

# Important Notice

This copy may be used only for the purposes of research and private study, and any use of the copy for a purpose other than research or private study may require the authorization of the copyright owner of the work in question. Responsibility regarding questions of copyright that may arise in the use of this copy is assumed by the recipient.

UNIVERSITY OF CALGARY

Influence of Low Frequencies on Seismic Impedance Inversion

by

Sina Esmaeili

A THESIS

SUBMITTED TO THE FACULTY OF GRADUATE STUDIES  
IN PARTIAL FULFILMENT OF THE REQUIREMENTS FOR THE  
DEGREE OF MASTER OF SCIENCE

GRADUATE PROGRAM IN GEOLOGY AND GEOPHYSICS

CALGARY, ALBERTA

APRIL, 2016

© Sina Esmaeili 2016

## **Abstract**

Acoustic impedance is a rock property that can be derived from seismic data and contains important information about subsurface properties. Mathematically, the acoustic impedance can be calculated from earth's reflectivity function and this function can be estimated from seismic data. However, estimation of reflectivity from seismic data even after excellent data processing, is always very bandlimited, lacking both low and high frequencies. In this situation, recovering any of this bandwidth, especially low frequencies, can be helpful.

The thesis will be focused on recovering low frequencies to improve impedance estimation and this includes trying to improve a frequency domain deconvolution algorithm using different smoother types and correcting the whitening error of deconvolution operator using color operator. At the end, the maximum correlation results between acoustic impedance inversion and well impedance demonstrate using color operator can increase the maximum correlation by around 20 percent comparing with the result without using color operator.

## **Acknowledgements**

I would like to express my gratitude to my supervisor, Dr. Gary F. Margrave, whose expertise, understanding, and patience, added considerably to my graduate experience. I have been amazingly fortunate to have an advisor who gave me the freedom to explore on my own, and at the same time the guidance to recover when my steps faltered. Gary taught me how to question thoughts and express ideas. His patience and support helped me overcome many crisis situations and finish this thesis. Thank you for everything.

Special thanks to Dr. Kristopher Innanen, Dr. Don Lawton, Dr. Larry Lines, Dr. Andreas Cordsen, Dr. Brian Russell and Dr. Faranak Mahmoudian for encouragements and constructive suggestions that have shaped up many parts in this thesis.

Thank you for the CREWES (the Consortium for Research in Elastic Wave Exploration Seismology) industrial sponsors and NSERC for supporting this work.

I am also grateful to the faculty, staff, and students of CREWES and the Department of Geoscience. Thank you to Laura Baird for all of the hard work that she does at CREWES, administrative support, ensuring that all deadlines were met and the annual CREWES conferences were well organized; to Kevin Hall for his great technical support; to Helen Isaac for helping me on modeling with GeoSyn software; to Kevin Bertram for taking days to print off my research posters for presentation at the Geoconvention and CREWES annual conferences and also Catherine Hubbell for all her assistance.

I would also like to thank all my friends and colleagues who gave me help and encouragement which enable me to start, move forward and complete this hard but very rewarding journey. It is difficult to name all of them, but what they did is unforgettable.

I would also like to thank my family for the support they provided me through my entire life and in particular, I must acknowledge my wife and best friend, Fatemeh, without whose love, encouragement and assistance, I would not have finished this thesis.

## **Dedication**

To my wife Fatemeh and my parents; this thesis only exists because of all of you.

## Table of Contents

Abstract .....	ii
Acknowledgements .....	iii
Dedication .....	v
Table of Contents .....	vi
List of Tables .....	viii
List of Figures and Illustrations .....	ix
List of Symbols, Abbreviations and Nomenclature .....	xviii
CHAPTER ONE: INTRODUCTION .....	1
1.1 Background .....	1
1.2 Acoustic reflection coefficient .....	3
1.3 Acoustic impedance .....	6
1.4 Seismic data and convolutional model .....	8
1.5 Bandlimited seismic data .....	11
1.6 Simple seismic model .....	14
1.7 Overview of chapters .....	21
1.8 MATLAB software .....	22
CHAPTER TWO: FREQUENCY DOMAIN DECONVOLUTION AND REFLECTIVITY ESTIMATION PROCESS .....	23
2.1 Introduction .....	23
2.2 Frequency domain deconvolution algorithm .....	23
2.3 Different smoothing methods .....	30
2.3.1 Boxcar smoother (BS) .....	30
2.3.2 Constant Gaussian smoother (CGS) .....	31
2.3.3 Frequency-Dependent Gaussian Smoother (FDGS) .....	32
2.4 The effect of different smoothers on frequency domain deconvolution .....	33
2.4.1 The results with Boxcar smoother .....	33
2.4.2 The results with constant Gaussian smoother .....	35
2.4.3 The results with frequency dependent Gaussian smoother .....	38
2.5 Summary .....	42
CHAPTER THREE: MINIMUM-PHASE COLOR OPERATOR .....	44
3.1 Introduction .....	44
3.2 Designing the color operator .....	56
3.3 Deconvolving the synthetic seismic data .....	63
3.4 Effect of color operator on deconvolved data .....	73
3.5 Summary .....	84
CHAPTER FOUR: EFFECT OF MINIMUM-PHASE COLOR OPERATOR ON HUSSAR REAL DATA 87	
4.1 Introduction .....	87
4.2 Data preparation .....	88
4.3 Color operator effects on seismic data and impedance inversion .....	91
4.4 Acoustic impedance inversion .....	95

4.5 Summary .....	104
CHAPTER FIVE: CONCLUSION .....	106
REFERENCES .....	110

## List of Tables

Table 2.1 The maximum correlation values between pseudo random reflectivity and estimated reflectivity calculated from different deconvolution algorithms. The values show the choice of frequency dependent Gaussian smoother can be best option.....	41
Table 3.1 The optimum boxcar and Gaussian smoother length for each dataset. The results show the Gaussian smoother length is approximately half of the boxcar smoother length..	67
Table 3.2. Calculated maximum correlation between deconvolved trace and well reflectivity of Hussar well. The results show higher correlation value when we use boxcar smoother in deconvolution algorithm in compare with the other smoother types.....	68
Table 3.3. The maximum correlation calculated between estimated reflectivity after using one of the color operators and real reflectivity.....	80
Table 4.1. The maximum correlation calculated for acoustic impedance estimation between the well impedance and the traces near those wells before and after applying color operator...	98

## List of Figures and Illustrations

Figure 1.1. When the wave crosses a layer boundary some of the energy is returned to the surface in the reflected wave and the rest of the energy continues downward through the next layer in the transmitted wave. ....	4
Figure 1.2 The normal incident ray paths associated with primaries. $Z_0 = 0$ represents the surface and it has been assumed that the source and receiver are located at the same point. ....	6
Figure 1.3 Schematic of matrix representation of convolution. The symmetry of W matrix shows that this process is stationary and is not changing in time (Margrave, 2002).....	10
Figure 1.4 (left) the amplitude spectrum of noisy data with different seismic to noise ratio in decibels. Their spectrum show -25db and -35db noise level for the data with $SNR = 2$ and $SNR = 5$ and (right) the same data in time domain. ....	13
Figure 1.5 Zooming at low frequency area to illustrate the effect of noise with different SNR on seismic data.....	13
Figure 1.6 Frequency filtering noisy seismic data due to reduce noise effects. Lower SNR needs large low frequency and small high frequency to be filtered in comparing with higher SNR.....	14
Figure 1.7. The single spike function in time domain and its amplitude spectrum in frequency domain. The Fourier transform of a single spike is broadband. ....	15
Figure 1.8 A simple 10 layers P-wave velocity model. The density was calculated from Gardner rule and the normal incident reflectivity is computed from equation 1.21.....	16
Figure 1.9 The synthetic seismic trace created with convolving of reflectivity and minimum-phase wavelet. ....	16
Figure 1.10 Reflectivity estimation using frequency domain deconvolution algorithm. ....	17
Figure 1.11 The acoustic impedance estimation computed from recursion formula compared with real estimation. The lack of low frequencies cause the misestimation of acoustic impedance. ....	18
Figure 1.12 The amplitude spectrum of estimated reflectivity which is not broadband and its low frequency components have been removed. ....	19
Figure 1.13 A broad band data may be considered to be the sum of a detailed data (10-250 Hz) and a gross data (0-9 Hz) .....	19
Figure 1.14 Estimated wavelet and its amplitude spectrum compared with source wavelet. The results in frequency domain shows in low frequency the real and estimated wavelets are	

not matching each other which is causing the lack of low frequencies in reflectivity estimations. ....	20
Figure 1.15 Recovering low frequency components using BLIMP algorithm with extracting the low frequency components from the real impedance. ....	21
Figure 2.1 The normal incident synthetic seismic trace created from pseudo random reflectivity and minimum-phase wavelet. ....	24
Figure 2.2 The amplitude spectrum of noisy seismic data compared with noise-free data. There is an specific frequency area which the noisy and noise free data are the same and can use the same method to extract deconvolution operator. ....	28
Figure 2.3 Boxcar smoothing procedure for the random dataset. ....	30
Figure 2.4 Gaussian distribution for using Gaussian smoother. ....	31
Figure 2.5 Constant Gaussian smoothing procedure for the random dataset. ....	32
Figure 2.6 Schematic of changing Gaussian smoother length with frequency. ....	32
Figure 2.7 Searching the optimum value for the boxcar smoother length in the frequency domain. The plot shows the best choice for the smoother length is 6Hz. ....	34
Figure 2.8. Smoothing the power of seismic spectrum using boxcar smoother with 6Hz of length. ....	34
Figure 2.9. The result of reflectivity estimation using the boxcar smoother with 6Hz of length. ....	35
Figure 2.10. Comparing the amplitude spectrum of pseudo random reflectivity and it estimation in frequency domain. Zooming the results in low frequencies (0-20Hz) demonstrate the misestimation of the reflectivity after deconvolution with boxcar smoother. ....	35
Figure 2.11. Searching the optimum value for the Gaussian smoother length in the frequency domain. The plot shows the best choice for the smoother length is 11Hz. ....	36
Figure 2.12. Smoothing the power of seismic spectrum using Gaussian smoother with 11Hz of length. ....	37
Figure 2.13. The result of reflectivity estimation using the constant Gaussian smoother with 11Hz of length. ....	37
Figure 2.14. Comparing the amplitude spectrum of pseudo random reflectivity and it estimation in frequency domain. Zooming the results in low frequencies (0-20Hz) demonstrate the misestimation of the reflectivity after deconvolution with constant Gaussian smoother. ....	38

Figure 2.15. Searching the optimum value for $n$ in frequency dependent Gaussian smoother length. $n$ is a deconvolution input parameter and indicates the rate of variation of smoother length.....	39
Figure 2.16. Gaussian distribution length variation with frequency. Smoother length becomes short in low frequencies and long in high frequencies.....	39
Figure 2.17. Smoothing the power of seismic spectrum using frequency dependent Gaussian smoother with $n = 9$ .....	40
Figure 2.18. The result of reflectivity estimation using the frequency dependent Gaussian smoother with $n = 9$ .....	40
Figure 2.19. Comparing the amplitude spectrum of pseudo random reflectivity and its estimation in frequency domain. Zooming the results in low frequencies (0-20Hz) demonstrate the misestimation of the reflectivity after deconvolution with frequency dependent Gaussian smoother.....	41
Figure 2.20. Acoustic impedance estimation which used different smoothers in their deconvolution algorithms.....	42
Figure 3.1. (top) Hussar is located at east of Calgary, Alberta (Google map) and (bottom) the location of the line and wells (Heather Lloyd, 2013). .....	44
Figure 3.2. The P-wave velocity log and density log of well 12-27 from Hussar experiment located at east of Calgary as well as its reflectivity calculated from equation 1.13. ....	45
Figure 3.3. The P-wave velocity log and density log of well 14-27 from Hussar experiment located at east of Calgary as well as its reflectivity calculated from equation 1.13. ....	45
Figure 3.4. The P-wave velocity log and density log of well 14-35 from Hussar experiment located at east of Calgary as well as its reflectivity calculated from equation 1.13. ....	46
Figure 3.5. The computed time-depth curve for well 12-27. The association of $t=0$ with $z=200$ (the first logged depth) means that no overburden model is included.....	48
Figure 3.6. The computed time-depth curve for well 14-27. The association of $t=0$ with $z=200$ (the first logged depth) means that no overburden model is included.....	48
Figure 3.7. The computed time-depth curve for well 14-35. The association of $t=0$ with $z=178$ (the first logged depth) means that no overburden model is included.....	48
Figure 3.8. The converted reflectivity of well 12-27 from depth domain into the time domain using time-depth curve are illustrated in both time domain (left) and frequency domain (right). The decrease in amplitude in the frequency domain above 130 Hz is due to antialias filtering. ....	49

Figure 3.9. The converted reflectivity of well 14-27 from depth domain into the time domain using time-depth curve are illustrated in both time domain (left) and frequency domain (right). The decrease in amplitude in the frequency domain above 130 Hz is due to antialias filtering. ....	49
Figure 3.10. The converted reflectivity of well 14-35 from depth domain into the time domain using time-depth curve are illustrated in both time domain (left) and frequency domain (right). The decrease in amplitude in the frequency domain above 130 Hz is due to antialias filtering. ....	50
Figure 3.11. The autocorrelation of pseudo random reflectivity and the reflectivity from well 12-27. The large negative value at lag=2 indicates the non-whiteness property of real reflectivity. ....	50
Figure 3.12 The normal incident synthetic seismic trace created from well 12-27 reflectivity and minimum-phase wavelet with 15Hz dominant frequency. ....	52
Figure 3.13. When the frequency domain deconvolution with the assumption of white spectrum reflectivity applying to the seismic data which resulted from colored spectrum reflectivity (well reflectivity), the deconvolved trace cannot does not include the color effects. (top) the well impedance and deconvolved trace in time domain and (bottom) their amplitude spectrum in frequency domain. ....	53
Figure 3.14. Comparing the acoustic impedance results using recursion formula and colored inversion method with well impedance. The 10Hz high pass filter has been applied to the well impedance and recursion formula impedance in this example. ....	55
Figure 3.15. The amplitude spectrum of the seismic data one after applying colored inversion operator and the other after applying -90 degree phase rotation. ....	56
Figure 3.16. Comparing the colored inversion method and -90 degree phase rotation on seismic data in time domain. ....	56
Figure 3.17. The calculated amplitude spectrum of AC color operator from multiplying Gaussian function with the autocorrelation of reflectivity of well 14-35 in frequency domain. ....	58
Figure 3.18. The calculated amplitude spectrum of AC color operator from multiplying Gaussian function with the autocorrelation of reflectivity of well 14-27 in frequency domain. ....	58
Figure 3.19. The calculated amplitude spectrum of AC color operator from multiplying Gaussian function with the autocorrelation of reflectivity of well 12-27 in frequency domain. ....	59
Figure 3.20 A comparison of well log reflectivity for Husky Hussar well in the time and frequency domains. The frequency domain views show clearly the effect of the anti-alias filter which begins its roll off at ½ of the Nyquist frequency. The low frequency roll off	

is essentially independent of sample rate and is similar in all sample rates. This low frequency roll off is what is modelled by our color operators. .... 60

Figure 3.21 The minimum-phase arctan color operator of Husky Hussar well 12-27 in time domain (left) and its amplitude spectrum in frequency domain (right) ..... 61

Figure 3.22. The sigmoidal color operator of Husky Hussar well 12-27 in time domain (left) and its amplitude spectrum in frequency domain (right) ..... 62

Figure 3.23. The arctan color operator has been designed for three Hussar well. Their comparison shows the differences are minor along the studied area. .... 63

Figure 3.24. The sigmoidal color operator has been designed for three Hussar well. Their comparison shows the differences are minor along the studied area. .... 63

Figure 3.25 The minimum-phase wavelet with 15Hz dominant frequency and 2 milliseconds sample rate. In the left this wavelet is shown in time domain and the right is the amplitude spectrum of the same wavelet in decibels. .... 64

Figure 3.26 The reflectivity functions related to each Husky Hussar well and their computed normal incident synthetic seismic trace. .... 65

Figure 3.27 Reflectivity estimation of Husky Hussar well 14-35 using different deconvolution algorithm. BS, CGS and FDGS represent boxcar smoother, constant Gaussian smoother and frequency dependent Gaussian smoother. .... 66

Figure 3.28 Reflectivity estimation of Husky Hussar well 14-27 using different deconvolution algorithm. BS, CGS and FDGS represent boxcar smoother, constant Gaussian smoother and frequency dependent Gaussian smoother. .... 66

Figure 3.29 Reflectivity estimation of Husky Hussar well 12-27 using different deconvolution algorithm. BS, CGS and FDGS represent boxcar smoother, constant Gaussian smoother and frequency dependent Gaussian smoother. .... 67

Figure 3.30 The error function between well reflectivity and deconvolved trace calculated for each well with three different smoother type in both time and frequency domain. .... 68

Figure 3.31. Comparing the smooth of seismic's power with the case if the actual wavelet has been as a smooth of seismic's power using BC smoother type for pseudo random reflectivity. .... 69

Figure 3.32. Comparing the smooth of seismic's power with the case if the actual wavelet has been as a smooth of seismic's power using CG smoother type for pseudo random reflectivity. .... 70

Figure 3.33. Comparing the smooth of seismic's power with the case if the actual wavelet has been as a smooth of seismic's power using FDG smoother type for pseudo random reflectivity. .... 70

Figure 3.34. Comparing the smooth of seismic's power with the case if the actual wavelet has been as a smooth of seismic's power using BC smoother type for well reflectivity. ....	71
Figure 3.35. Comparing the smooth of seismic's power with the case if the actual wavelet has been as a smooth of seismic's power using CG smoother type for well reflectivity. ....	71
Figure 3.36. Comparing the smooth of seismic's power with the case if the actual wavelet has been as a smooth of seismic's power using FDG smoother type for well reflectivity. ....	72
Figure 3.37. The deconvolved trace of synthetic trace created from well 14-35 data using boxcar smoother algorithm. ....	74
Figure 3.38. The deconvolved trace of synthetic trace created from well 14-27 data using boxcar smoother algorithm. ....	74
Figure 3.39. The deconvolved trace of synthetic trace created from well 12-27 data using boxcar smoother algorithm. ....	75
Figure 3.40. The result of applying arctan color operator on the deconvolved trace from well 14-35 in the time and frequency domain and comparing it with the deconvolved trace without applying color operator. ....	76
Figure 3.41. The result of applying sigmoidal color operator on the deconvolved trace from well 14-35 in the time and frequency domain and comparing it with the deconvolved trace without applying color operator. ....	76
Figure 3.42. The result of applying arctan color operator on the deconvolved trace from well 14-27 in the time and frequency domain and comparing it with the deconvolved trace without applying color operator. ....	77
Figure 3.43. The result of applying sigmoidal color operator on the deconvolved trace from well 14-27 in the time and frequency domain and comparing it with the deconvolved trace without applying color operator. ....	77
Figure 3.44. The result of applying arctan color operator on the deconvolved trace from well 12-27 in the time and frequency domain and comparing it with the deconvolved trace without applying color operator. ....	78
Figure 3.45. The result of applying sigmoidal color operator on the deconvolved trace from well 12-27 in the time and frequency domain and comparing it with the deconvolved trace without applying color operator. ....	78
Figure 3.46. The result of applying AC color operator on the deconvolved trace from well 14-35 in the time and frequency domain and comparing it with the deconvolved trace without applying color operator. ....	79

Figure 3.47. The result of applying AC color operator on the deconvolved trace from well 14-27 in the time and frequency domain and comparing it with the deconvolved trace without applying color operator. ....	79
Figure 3.48. The result of applying AC color operator on the deconvolved trace from well 12-27 in the time and frequency domain and comparing it with the deconvolved trace without applying color operator. ....	80
Figure 3.49. The acoustic impedance was calculated for well 14-35 data after and before applying color operator to see the effect of different color operators on impedance results. The results show improvements when the color operators have been used after deconvolution.....	81
Figure 3.50. The acoustic impedance was calculated for well 14-27 data after and before applying color operator to see the effect of different color operators on impedance results. The results show improvements when the color operators have been used after deconvolution.....	81
Figure 3.51. The acoustic impedance was calculated for well 12-27 data after and before applying color operator to see the effect of different color operators on impedance results. The results show improvements when the color operators have been used after deconvolution.....	82
Figure 3.52. The maximum correlation results between estimated acoustic impedances with BLIMP algorithm and well 14-35 impedance. Different low cut-off frequencies have been used in BLIMP algorithm. ....	83
Figure 3.53. The maximum correlation results between estimated acoustic impedances with BLIMP algorithm and well 14-27 impedance. Different low cut-off frequencies have been used in BLIMP algorithm. ....	83
Figure 3.54. The maximum correlation results between estimated acoustic impedances with BLIMP algorithm and well 12-27 impedance. Different low cut-off frequencies have been used in BLIMP algorithm. ....	84
Figure 4.1. Hussar seismic data processed by CGG Veritas and the location of three wells. ....	88
Figure 4.2. The time variant balancing operator applied to the Hussar seismic data. ....	88
Figure 4.3. P-wave velocity and density logs of well 14-35 from Hussar data. ....	89
Figure 4.4. P-wave velocity and density logs of well 14-27 from Hussar data. ....	89
Figure 4.5. P-wave velocity and density logs of well 12-27 from Hussar data. ....	90
Figure 4.6 Applying appropriate time shifting (and if applicable phase shifting), because of attenuation, different time slices might need different time shifts. This can be done by time stretching algorithm. ....	91

Figure 4.7. The effect of applying arctan color operator on Hussar seismic data. (left) before applying color operator and (right) after applying color operator. The results show that the seismic data after applying color operator become dim which means their power of amplitude at the low frequency part are decreasing.....	92
Figure 4.8. The effect of applying sigmoidal color operator on Hussar seismic data. (left) before applying color operator and (right) after applying color operator. The results show that the seismic data after applying color operator become dim which means their power of amplitude at the low frequency part are decreasing.....	92
Figure 4.9. The effect of applying AC color operator on Hussar seismic data. (left) before applying color operator and (right) after applying color operator. The results show that the seismic data after applying color operator become dim which means their power of amplitude at the low frequency part are decreasing.....	93
Figure 4.10. The amplitude spectrum of trace from Hussar seismic data near well 14-27 before and after applying arctan color operator. ....	93
Figure 4.11. The amplitude spectrum of trace from Hussar seismic data near well 14-27 before and after applying arctan color operator. ....	94
Figure 4.12. The amplitude spectrum of trace from Hussar seismic data near well 14-27 before and after applying AC color operator. ....	94
Figure 4.13 Impedance inversion using recursion formula for the seismic data before and after applying color operator. ....	95
Figure 4.14. The BLIMP impedance inversion without using any color operator. The low frequency in BLIMP algorithm was chosen 3.5Hz and the high frequency is linearly varying from 60Hz to 70Hz from left to the right side of seismic section. ....	96
Figure 4.15. The BLIMP impedance inversion for arctan color operator. The low frequency in BLIMP algorithm was chosen 3.5Hz and the high frequency is linearly varying from 60Hz to 70Hz from left to the right side of seismic section. ....	97
Figure 4.16. The BLIMP impedance inversion for sigmoidal color operator. The low frequency in BLIMP algorithm was chosen 3.5Hz and the high frequency is linearly varying from 60Hz to 70Hz from left to the right side of seismic section. ....	97
Figure 4.17. The BLIMP impedance inversion for AC color operator. The low frequency in BLIMP algorithm was chosen 3.5Hz and the high frequency is linearly varying from 60Hz to 70Hz from left to the right side of seismic section. ....	98
Figure 4.18. The colored inversion operator derivation process which needs to derive the spectral shape of well impedance. ....	99
Figure 4.19. The designed colored inversion operator from averaged well impedance and averaged seismic trace of Hussar data. ....	99

Figure 4.20. The result of applying colored inversion operator on Hussar seismic data. The computed impedance in this case is only showing the variation of impedance from its trend not its real value. .... 100

Figure 4.21. The amplitude spectrum of colored inversion result near each well and its comparison with the real acoustic impedance amplitude spectrum. The approximate range of frequency that colored inversion method contains is 14 to 62Hz at the location of well 14-35, 14 to 68Hz at the location of well 14-27 and 20 to 70Hz at the location of well 12-27. .... 101

Figure 4.22. Comparing the result of colored inversion method and -90 degree phase rotation on seismic data. .... 103

## List of Symbols, Abbreviations and Nomenclature

Symbol	Definition
AC	AutoCorrelation color operator
AGC	Automatic Gain Correction
AI	Acoustic Impedance (abbreviation)
BLIMP	BandLimited IMPedance inversion
BS	Boxcar Smoother
CGS	Constant Gaussian Smoother
CREWES	Consortium of Research in Elastic Wave Exploration Seismology
FDGS	Frequency Dependent Gaussian Smoother
G	Gaussian distribution
Hz	Hertz, a unit of frequency
$I$	Acoustic Impedance (mathematical symbol)
$I_r$	Impulse response
Kg	Kilograms
Ln	Logarithm
m	Meters
P-wave	Compressional wave
R	Reflection coefficient
$r(t)$	Reflectivity function
Sec	Seconds

Seismo	CREWES Matlab code to create normal incident synthetic seismic trace
SNR	Signal to Noise Ratio
S-wave	Shear wave
$s(t)$	Seismic trace
T	Transmission coefficient
$u_{inc}$	Incident wave
$u_{ref}$	Reflected wave
$u_{tr}$	Transmitted wave
v	Velocity
$v_p$	P-wave velocity
$v_s$	S-wave velocity
$w(t)$	Wavelet
$\delta$	Dirac delta function
$\sigma$	Half width of Gaussian distribution when reaches to $e^{-1/2}$ of its maximum
$\omega$	Angular frequency
$\bullet$	Convolution operator
$*$	Multiplication operator

## CHAPTER ONE: INTRODUCTION

### 1.1 Background

A primary goal of seismic exploration is to determine the earth's reflectivity as a function of position beneath a seismic survey. The subsurface of the earth consists of different types of layers and each interface can be determined by its reflection coefficient. The layer's thickness, identification, and reflectivity estimate are significant for hydrocarbon exploration and for seismic interpretation. This can be done by seismic exploration which looks for hydrocarbons in rocks that usually have high porosity. Porosity or void fraction is a measure of the void spaces in a material, and is a fraction of the volume of voids over the total volume, between 0 and 1, or as a percentage between 0 and 100%.

Seismic exploration starts first with generation of the seismic pulse which is called the wavelet. Generally the seismic sources can be divided as either natural sources (uncontrolled) like tectonic earthquakes, volcanic tremors, rock falls or man-made sources (controlled) like dynamite explosives, hammer on a metal plate, air gun or Vibroseis trucks (Thumper trucks). In seismic exploration for the purpose of this study the second type of source has been used. Each of these source types have different energy content for instance dynamite creates an intense pressure pulse of very short duration, measured in a few milliseconds. In seismic exploration acquiring good quality data is more likely assured by choosing optimum parameters with respect to the target zone (Scheffers et al., 1997). One of the key parameters is the selection of the appropriate seismic source and its characteristics. This selection should be done using several criteria which are related to the type of problem under consideration. One of the important criteria to consider is the source energy content, which should be large enough so that adequate information is recorded from the desired

target depth of the survey. Another criterion is the total cost of the project, and the most appropriate source for the project budget would be selected (Karastathis et al., 1995).

Once the seismic pulse is generated it propagates spherically in homogeneous media. In case of dynamite explosion, the wall rock or material surrounding the explosive charge is subjected to intense stress exceeding their limit for some distance out from the charge. This displacement of media can propagate from point to point in the earth. When the wave crosses a layer boundary some of the energy is returned to the surface in the reflected wave and the rest of the energy continues downward through the next layer in the transmitted wave. A complete and detailed study of the seismic wave propagation and its properties can be found in Aki and Richards (2002). The reflected waves from subsurface layers can be recorded via electromagnetic devices called geophones. A geophone is a device that converts ground movement (velocity or the time-derivative of displacement) into voltage, which may be recorded at a recording station. Geophones usually do not require electrical power to operate, and are lightweight, robust, and able to detect extremely small ground displacements (Cambois, 2002). The recorded data are usually contaminated with noise, which refers to any unwanted features in the data. These noises can be random noise such as wind or vehicle traffic in a land environment or coherent noise. The coherent noise can be generated by the seismic experiment as undesirable signals, such as ground roll, reverberating refractions and multiples or can be generated by other sources like pump jack noise and power line noise.

The other criteria of seismic source selection is its broadband coverage which means it must cover as many frequency content as possible to obtain the required resolution for the exploration of the particular problem. However in seismic exploration it is impossible to produce a fully broadband source wavelet (a discrete delta function), thus a recorded seismic trace will

always be band-limited by the source wavelet (Oldenburg et. al., 1983). This is one of the problems in seismic exploration that the recorded data only have a limited range of frequencies. In the past, low frequency seismic recordings have been shunned in the exploration industry, largely because of their overwhelming contamination with coherent noise. Surface waves or ground roll have been especially problematic. Ground roll can overwhelm other reflected events, especially at near offset from the source (Sheriff and Geldart, 1982; Yilmaz, 1987). This low frequency content can be attenuated in the field using arrays (Ongkiehong L. et al, 1987, 1988) or in the processing center using low-cut filters (Yang et al., 2009).

## 1.2 Acoustic reflection coefficient

As mentioned before, determining the earth's reflectivity as a function of position is one of the exploration seismology goals. Consider a medium with two different horizontal layers. Again as it has been mentioned, each subsurface rock layer has unique properties including P-wave velocity, S-wave velocity and density. The downgoing acoustic wave (e.g. incident wave),  $u_{inc}$ , approaches to the interface of the two layers with the angle of  $\theta_1$ . Acoustic wave theory can relate the reflected ( $u_{ref}$ ) and transmitted ( $u_{tr}$ ) waves to the incident wave as

$$u_{ref} = R(\theta)u_{inc}, \quad 1.1$$

$$u_{tr} = T(\theta)u_{inc}, \quad 1.2$$

where  $R(\theta)$  and  $T(\theta)$  are reflection and transmission coefficients given by (Yilmaz, 1987)

$$R(\theta) = \frac{\rho_2 v_2 \cos(\theta_1) - \rho_1 v_1 \cos(\theta_2)}{\rho_2 v_2 \cos(\theta_1) + \rho_1 v_1 \cos(\theta_2)}, \quad 1.3$$

$$T(\theta) = \frac{2\rho_2 v_2 \cos(\theta_1)}{\rho_2 v_2 \cos(\theta_1) + \rho_1 v_1 \cos(\theta_2)}, \quad 1.4$$

where  $v$  and  $\rho$  are P-wave velocity and density respectively and  $\theta_1$  and  $\theta_2$  are incident and transmitted angles respectively (Figure 1.1) and they are related by Snell's law

$$\frac{\sin(\theta_1)}{v_1} = \frac{\sin(\theta_2)}{v_2}. \quad 1.5$$

In case of normal incident waveform, all the incident, reflected and transmitted angles are zero which means all three ray paths are perpendicular to the interface. In this case the equations 1.3 and 1.4 become

$$R = \frac{\rho_2 v_2 - \rho_1 v_1}{\rho_2 v_2 + \rho_1 v_1}, \quad 1.6$$

$$T = \frac{2\rho_2 v_2}{\rho_2 v_2 + \rho_1 v_1}, \quad 1.7$$

which shows that normal incidence reflection and transmission coefficients depend only on rock density and velocity.

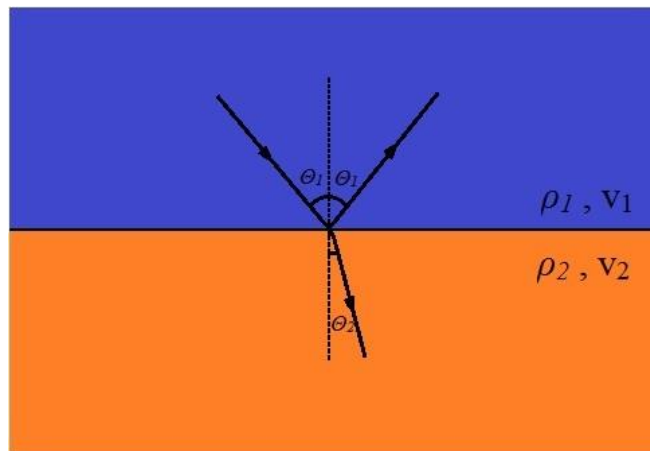


Figure 1.1. When the wave crosses a layer boundary some of the energy is returned to the surface in the reflected wave and the rest of the energy continues downward through the next layer in the transmitted wave.

Assuming a medium with number of different layers with different thicknesses, the downgoing wave approaches each layer at different time and it is possible to write the earth's impulse response as a function of time. The earth's impulse response refers to the reaction of earth in response to an impulsive source (Dirac delta) and the impulse response contains all physical and geological effects such as attenuation, multiples, transmission losses, spherical divergence, etc. (Margrave, 2002). The times of the layer boundaries are not necessarily regularly spaced. Typically,  $t_0$  and  $R_0$  represent the time and reflectivity at the surface and it is assumed that their value are zero. Thus, if the impulse response only contains the primaries (a primary is described as a single-bounce reflections event whereas a multiple has more than one bounce), it can be represented as

$$I_r(t) = R_1\delta(t - \tau_1) + R'_2\delta(t - \tau_2) + \dots \quad 1.8$$

where  $\delta$  is a Dirac delta function,  $R_1$  is the primary reflection coefficient of the first layer and  $R'_2$  is represented as (Waters, 1981)

$$R'_2 = T_{1,2}R_2T_{2,1}, \quad 1.9$$

where  $T_{1,2} = (1 - R_1)$  and  $T_{2,1} = (1 + R_1)$  are denoting the transmitted coefficient from layer 1 to layer 2 and from layer 2 to layer 1 respectively (Figure 1.2). The values of  $R'_i$  for larger  $i$  becomes complicated because of transmission through shallower interfaces, in the first case, and because of delays through media of different velocities, in the second case (Claerbout, 1985). In seismic data processing removing the amplitude effects of spherical spreading and transmission loss is called gain correction. However, if the velocity only varies weakly, such that reflection coefficients are all small, transmission pairs  $T_{n-1,n}T_{n,n-1} = 1 - R_{n-1}^2 \approx 1$  tend toward unity, such that

$$R'_i \approx R_i, \quad 1.10$$

and the equation 1.8 can represent the reflectivity function as

$$R(t) = R_1\delta(t - \tau_1) + R_2\delta(t - \tau_2) + \dots \quad 1.11$$

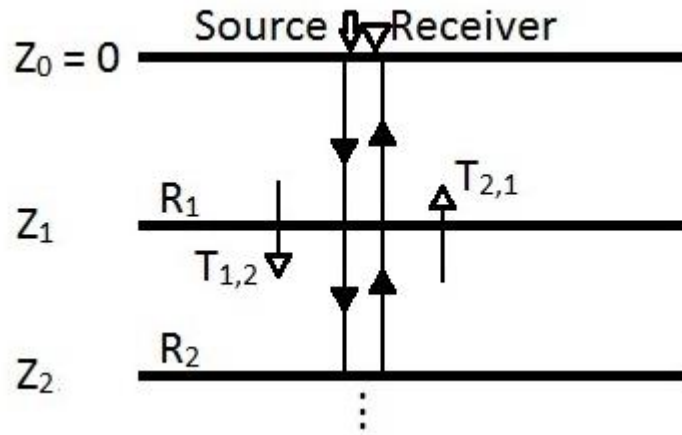


Figure 1.2 The normal incident ray paths associated with primaries.  $Z_0 = 0$  represents the surface and it has been assumed that the source and receiver are located at the same point.

### 1.3 Acoustic impedance

In equation 1.3 and 1.4, the product of P-wave velocity and density is called acoustic impedance which is dependent on the porosity (and other elastic properties) of the rock and it shown by  $I$ . For instant the hydrocarbon filled rocks usually have high porosity which tend to produce lower impedances than similar rocks (Dolberg, et al., 2000). Thus, finding the impedance variation in depth or time for the subsurface rocks can be a good clue for hydrocarbon exploration. Measuring the rock properties directly can be done at the well locations using well log data which means geophysicists are able to calculate the acoustic impedance at the well location. However, having wells at every single locations of the field not only is impossible, but also is massively expensive and impractical. Seismic reflection surveys are a commonly used exploration method that produces an image of the subsurface. This type of survey measures reflection coefficients that

are an interface property instead of layer property like impedance. The estimation of acoustic impedance from a reflectivity function is called seismic impedance inversion.

Back to the equation 1.6, the reflection coefficient in terms of acoustic impedance becomes

$$R = \frac{I_2 - I_1}{I_2 + I_1}, \quad 1.12$$

and generally, for layer n it becomes

$$R_n = \frac{I_n - I_{n-1}}{I_n + I_{n-1}}, \quad 1.13$$

where

$$I_n = \rho_n v_n. \quad 1.14$$

The equation 1.13 can be expressed in terms of reflectivity by

$$I_n = I_{n-1} \left( \frac{1 + R_n}{1 - R_n} \right), \quad 1.15$$

where the next layer in the sequence is dependent on the impedance of layer above it. As assumed, the variation of velocity and density are such that the reflection coefficients are much less than one. Using the mathematical approximation that  $|R_n| \ll 1$ , this equation becomes

$$I_n = I_{n-1} (1 + R_n) (1 - R_n)^{-1} \approx I_{n-1} (1 + R_n) (1 + R_n) = I_{n-1} (1 + R_n)^2 \approx I_{n-1} (1 + 2R_n), \quad 1.16$$

and applying the same procedures into the  $I_{n-1}$  it becomes

$$I_{n-1} \approx I_{n-2} (1 + 2R_{n-1}). \quad 1.17$$

This can be done for every next layers and putting all in equation 1.16 such that

$$I_n = I_1 \prod_j^n (1 + 2R_j) \quad 1.18$$

and applying  $(1 + 2R_j) \approx e^{2R_j}$  approximation to 1.18

$$I_n = I_1 \prod_j^n (e^{2R_j}) = I_1 e^{2 \sum_{j=1}^n R_j}, \quad 1.19$$

where  $I_1$  is the impedance at the first layer. Equation 1.19 also known as the impedance recursion formula and all that is needed to calculate the acoustic impedance for subsurface is having reflectivity function either in time or depth and value of impedance at the first layer. To estimate acoustic impedance as precisely as possible, the reflectivity should have broadband frequency which means it contains all significant power at all frequencies. However, as it will be seen, in the real world the reflectivities only contain a limited range of frequencies.

#### 1.4 Seismic data and convolutional model

The simplest model to introduce the seismic data is the convolutional model which represents the seismic data as a convolution of the wavelet and the reflectivity. In mathematics, the convolution is an operation that expresses the amount of overlap of one function  $g$  as it is shifted over another function  $f$  (Margrave, 2002).

$$c = f \bullet g$$

$$c_j = \sum_k f_k g_{j-k}, \quad 1.20$$

and this is a good approximation for gain corrected field data. When the wavelet,  $w$ , propagates in the earth and goes down through the earth's layers, regardless of the effect of geometrical spreading, transmission losses, a simple geophysical model can be introduced by a convolutional model. Note that because of stationary property of convolutional model which means it does not change with time, the an-elastic absorption and multiple reflections which are nonstationary cannot be modeled with convolutional model. The stationary property is basically means that the wavelet does not evolve in time as it propagates. Seismic data recorded by a receiver are towel modelled by a convolution of earth's reflectivity function with a known wavelet (Sheriff and Geldart, 1995).

$$s(t) = r(t) \bullet w(t), \quad 1.21$$

and for continuous functions this equation becomes

$$s(t) = \int_{-\infty}^{+\infty} r(\tau)w(t-\tau)d\tau. \quad 1.22$$

With a simple mathematical calculation it is possible to show that the convolution operator has commutative property which means

$$s = r \bullet w = w \bullet r. \quad 1.23$$

For discrete functions it is also possible to show the equation 1.23 in matrix representation.

For instance  $s_0$  and  $s_1$  can be written such that

$$\begin{aligned} s_0 &= \dots + w_0 r_0 + w_{-1} r_1 + w_{-2} r_2 + \dots \\ s_1 &= \dots + w_1 r_0 + w_0 r_1 + w_{-1} r_2 + \dots \end{aligned}, \quad 1.24$$

which means for  $n$  elements of  $s$  it becomes

$$\begin{bmatrix} \vdots \\ w_0 & w_{-1} & w_{-2} & w_{-3} \\ w_1 & w_0 & w_{-1} & w_{-2} \\ w_2 & w_1 & w_0 & w_{-1} \\ w_3 & w_2 & w_1 & \ddots \\ \vdots & \vdots & \vdots & \vdots \end{bmatrix}_{n \times m} \begin{bmatrix} r_0 \\ r_1 \\ r_2 \\ \vdots \\ r_m \end{bmatrix}_{m \times 1} = \begin{bmatrix} s_0 \\ s_1 \\ s_2 \\ \vdots \\ s_n \end{bmatrix}_{n \times 1}. \quad 1.25$$

The equation 1.25 is the matrix representation of convolution of reflectivity and wavelet and W matrix is convolution operator. The symmetry of the W matrix is clear in this equation and also each column contains the wavelet with the zero time sample aligned on the main diagonal which means that the wavelet is shifting in time along the each column (e.g. stationary) (Figure 1.3). This fact is one of the basic and important assumptions in the developing of convolutional model for seismic data which is not strictly true in the real world where the wavelet includes attenuation and more other effects.

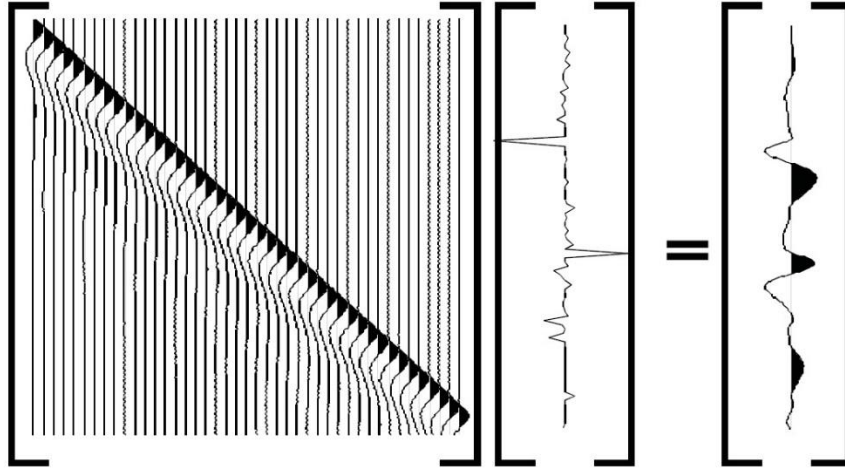


Figure 1.3 Schematic of matrix representation of convolution. The symmetry of  $W$  matrix shows that this process is stationary and is not changing in time (Margrave, 2002).

The seismic traces are always recorded in time. However, for better understanding of their properties and also for processing them, it is useful to look at them in other frameworks. In mathematics, any function  $f(t)$  be built out of sin's and cos's or identically complex exponentials such that

$$f(t) = \frac{1}{2\pi} \int_{-\infty}^{\infty} F(\omega) e^{i\omega t} d\omega, \quad 1.26$$

where

$$F(\omega) = \int_{-\infty}^{\infty} f(t) e^{-i\omega t} d\omega. \quad 1.27$$

The equation 1.26 and 1.27 are called inverse and forward Fourier transform. The forward Fourier transform equation computes the complex coefficients,  $F(\omega)$ , of the complex sinusoids which, when summed (integrated), will yield  $f(t)$ . Usually  $F(\omega)$  is decomposed into two separate real functions

$$\text{amplitude spectrum: } A(\omega) = |F(\omega)| = \sqrt{\text{Re}(F(\omega))^2 + \text{Im}(F(\omega))^2} \quad 1.28$$

$$\text{phase spectrum: } \varphi(\omega) = \tan^{-1} \left( \frac{\text{Im}(F(\omega))}{\text{Re}(F(\omega))} \right). \quad 1.29$$

One of the most important and fundamental applications of Fourier transform in all of signal processing is the Fourier transform of convolution. Consider  $h(t)$  is the convolution of two functions  $f(t)$  and  $g(t)$  such that

$$h(t) = \int_{-\infty}^{\infty} f(\tau)g(t-\tau)d\tau . \quad 1.30$$

It is possible to show (Yilmaz, 1987) that the Fourier transform of  $h(t)$  is a normal multiplication of spectrum of  $f(t)$  and  $g(t)$  which means

$$H(\omega) = F(\omega)G(\omega), \quad 1.31$$

where

$$\begin{aligned} H(\omega) &= \int_{-\infty}^{\infty} h(t)e^{-i\omega t} dt \\ F(\omega) &= \int_{-\infty}^{\infty} f(t)e^{-i\omega t} dt, \\ G(\omega) &= \int_{-\infty}^{\infty} g(t)e^{-i\omega t} dt \end{aligned} \quad 1.32$$

This is a very remarkable result which leads to an extremely fast algorithm for performing the digital Fourier transform which called Fast Fourier Transform (FFT). Using the FFT a convolution of two functions can be done by multiplying their spectra and inverse Fourier transforming the results.

### 1.5 Bandlimited seismic data

Rock properties measured from the log data at the borehole contain a very broad bandwidth of frequency information. However, seismic data that have been recorded at the earth's surface

have a much more limited frequency band. The bandlimited nature of the source, the internal structure of the geophone which records the data, and also the complexity of the subsurface because of the attenuation and other properties are some of the reasons of losing most of the data bandwidth during the seismic survey. For example, the seismic field system, including sources, receivers and recording instruments, is responsible for removing low frequencies from the signal, whereas earth effects, sources, and the recording system are responsible for removing (or not generating) the high-frequencies (Aki and Richards, 2002).

The other issue is the data are contaminated with noises and represented by signal to noise ratio (SNR). There are different methods to suppress the noise effect for either random noise (Canales, 1984) or coherent noise (Larner, et al., 1983) or improve the SNR such as band-pass filtering, F-K filtering, and stacking (Yilmaz, 1987). Furthermore, the choice of seismic data acquisition methods can affect the SNR (Bagaini, et al., 2010). Figure 1.4 shows synthetic seismic data affected by random noise. The left hand side of this figure shows the amplitude spectrum of two noisy traces with different SNR and the right hand side plot shows the same data in time domain. As shown, as this ratio increases, the high frequencies are less contaminated and the time-domain data is higher quality. Consider the application of frequency filters at specific frequencies to reduce noise (Yu, et al., 1984). For example, looking at the amplitude spectrum of noisy data at Figure 1.4 shows that the data higher than 150Hz for  $SNR = 5$  data and higher than 100Hz for  $SNR = 2$  data need to be filtered. Also, in low frequencies, Figure 1.5, frequencies lower than 2Hz and 5Hz should be filtered for  $SNR = 5$  and  $SNR = 2$  data respectively.

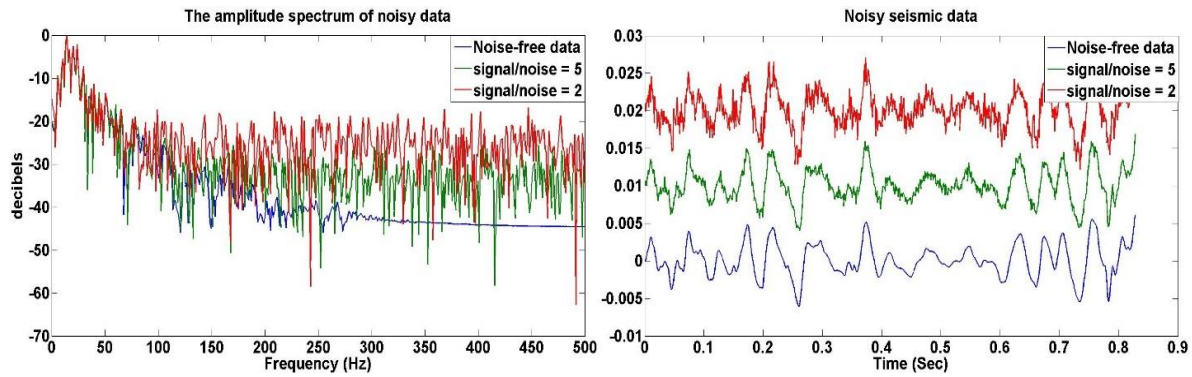


Figure 1.4 (left) the amplitude spectrum of noisy data with different seismic to noise ratio in decibels. Their spectrum show -25db and -35db noise level for the data with  $SNR = 2$  and  $SNR = 5$  and (right) the same data in time domain.

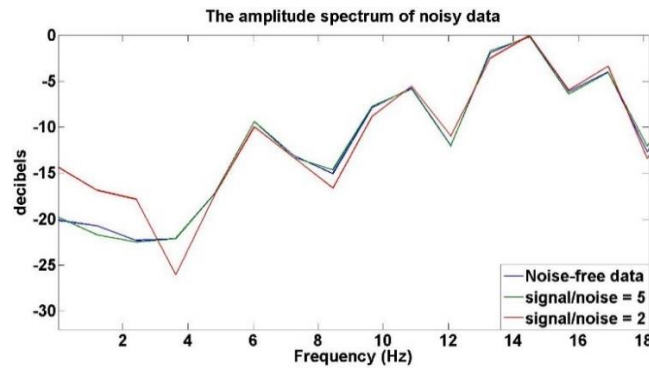


Figure 1.5 Zooming at low frequency area to illustrate the effect of noise with different SNR on seismic data

Figure 1.6 illustrates the result of filtering the noisy data in both frequency and time domain with the mentioned cut-off frequencies. Denoising of the filtered data can cause the elimination of some other useful information from original data. For instance, after removing different noises from the real seismic data the result are very bandlimited sometimes between 20 to 70Hz and consequently a lot of information of data in low and high frequencies is lost.

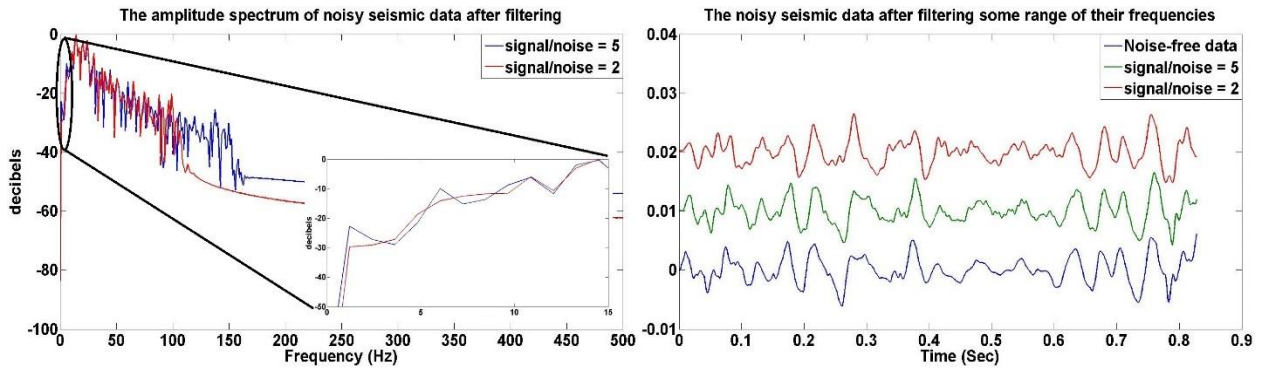


Figure 1.6 Frequency filtering noisy seismic data due to reduce noise effects. Lower SNR needs large low frequency and small high frequency to be filtered in comparing with higher SNR.

### 1.6 Simple seismic model

To understand the importance of frequency bandwidth reduction, especially low frequencies, examining a simple model can be helpful. As previously mentioned, in a very simple case, based on convolutional model a seismic trace is a convolution of earth reflectivity function and wavelet

$$s(t) = r(t) \cdot w(t) \quad 1.33$$

The model was created with 10 layers with varying velocity and density values (Figure 1.8). Using the equation 1.13, the reflectivity function can be calculated for each layer and as shown in the figure, it can be represented as a trace of spikes (equation 1.11) which means the modeled reflectivity is broadband. The reason is because a single spike has an amplitude spectrum equal to 1 at all frequencies and because the Fourier transform is a linear operator, the Fourier transform of a spike sequences is the sum of the transforms of a set of shifted spikes which become broadband (Figure 1.7).

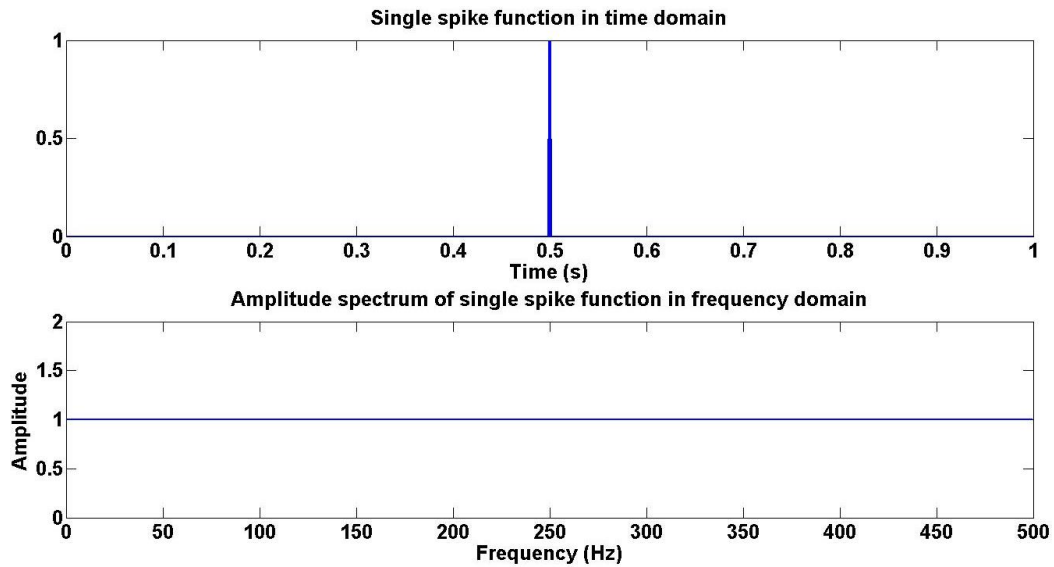


Figure 1.7. The single spike function in time domain and its amplitude spectrum in frequency domain. The Fourier transform of a single spike is broadband.

Based on equation 1.21 to create the normal incident synthetic seismic trace the calculated reflectivity from velocity and density log can be convolved with minimum-phase wavelet with 15 Hz dominant frequency and 2 milliseconds sample rate (Figure 1.9). The reason for choosing a minimum-phase wavelet and what exactly the minimum-phase wavelet is will be discussed later (chapter 2). The computed synthetic trace is a simple example that the geophone records in the field and the geophysicist's goal is estimating the reflectivity and then the impedance from the known seismic trace.

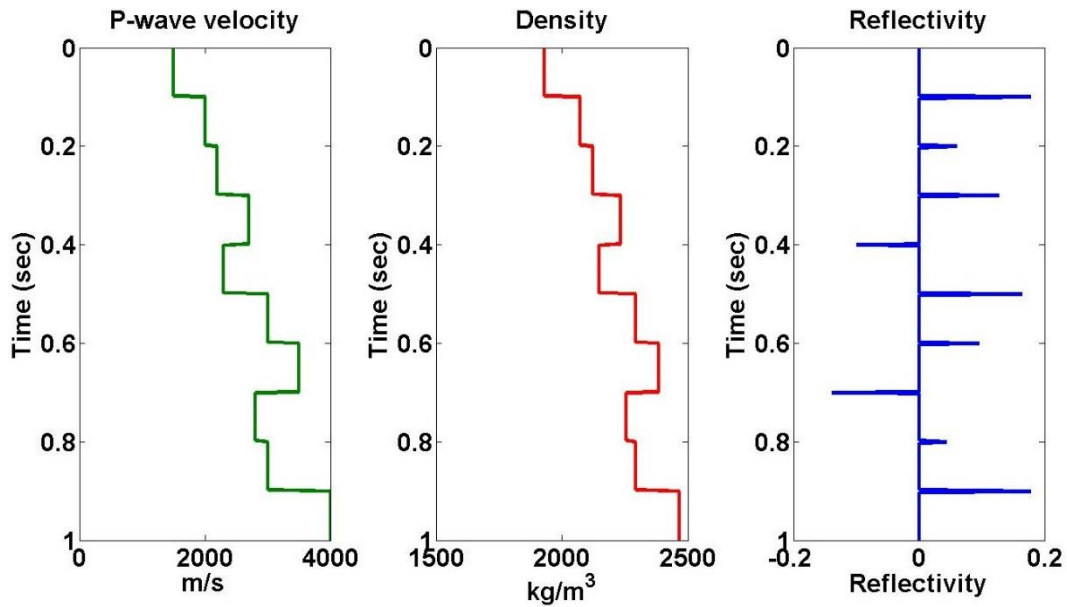


Figure 1.8 A simple 10 layers P-wave velocity model. The density was calculated from Gardner rule and the normal incident reflectivity is computed from equation 1.21.

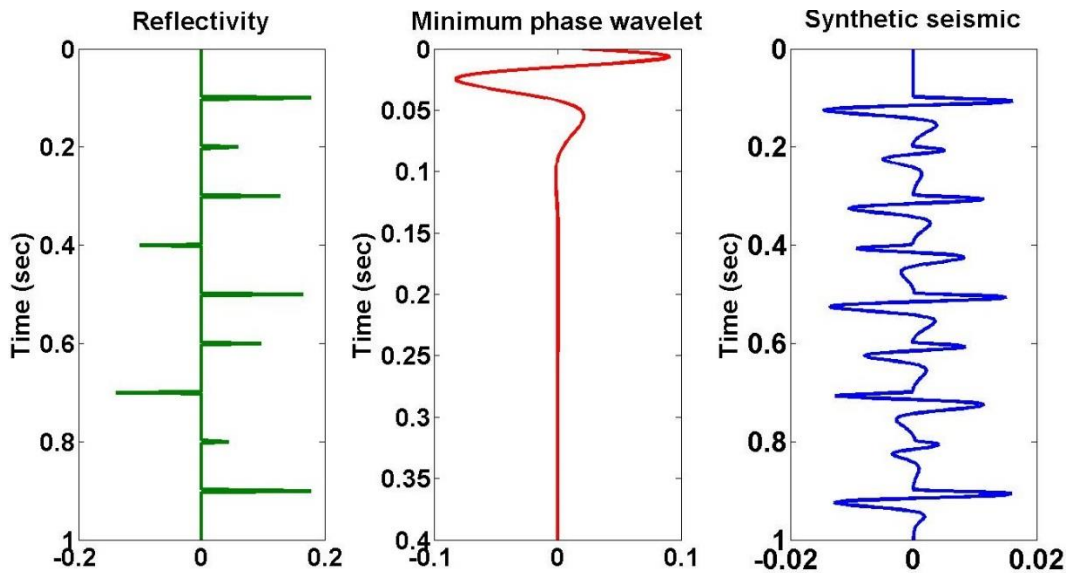


Figure 1.9 The synthetic seismic trace created with convolving of reflectivity and minimum-phase wavelet.

Based on equation 1.31 the Fourier transform of equation 1.21 becomes

$$S(f) = R(f)W(f) \quad 1.34$$

where  $S(f)$ ,  $R(f)$  and  $W(f)$  are the amplitude spectrum of seismic data, reflectivity and wavelet respectively. Also, here only the seismic trace is known and both earth reflectivity and wavelet are

unknown and the estimation of both functions are related to each other. It means that in equation 1.34 there are infinitely many possibilities for reflectivity and wavelet to give the same result in the left hand side. However, as will be discussed in the next chapter, by making certain assumptions about the nature of both the wavelet and the reflectivity, a very acceptable solution can be found. This is called deconvolution. In mathematics, deconvolution is an algorithm-based process used to reverse the effects of convolution on recorded data and the frequency domain deconvolution method is one of the simplest deconvolution methods. This deconvolution method will be discussed detailed on the next chapter. By applying the frequency domain deconvolution method to the seismic trace the reflectivity can be estimated. Figure 1.10 illustrates the estimated and the real reflectivity. As shown in this figure, all the reflectivity spikes have been estimated in the right positions and approximately right amplitude. However, there are also extra weak spikes in the estimated reflectivity which the actual one does not have.

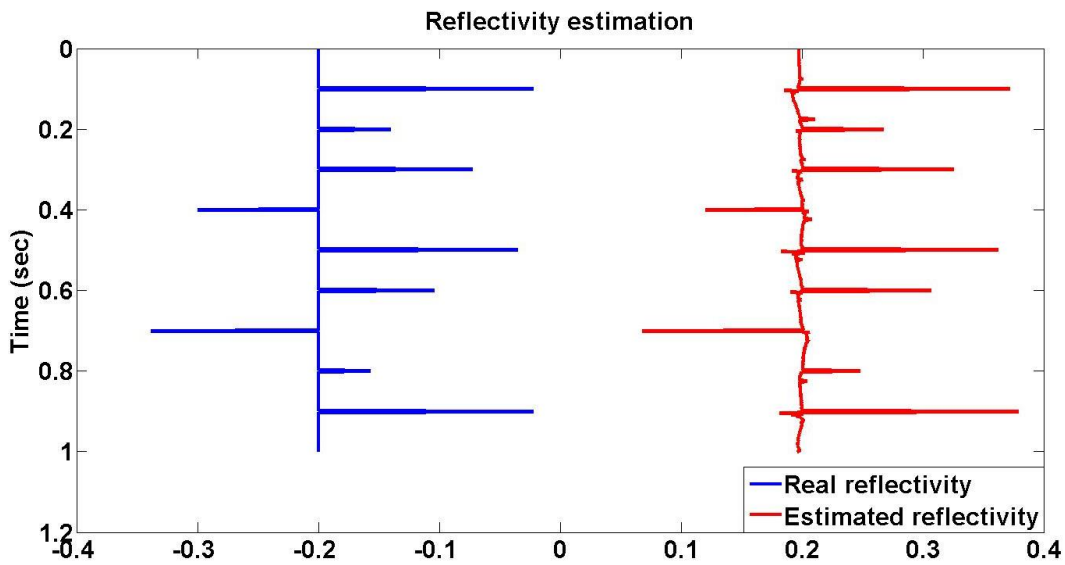


Figure 1.10 Reflectivity estimation using frequency domain deconvolution algorithm.

Using the equation 1.19 and computed reflectivity and also the first layer's impedance from multiplying its P-wave velocity and density, the acoustic impedance of the model can be

calculated. The result has been shown in Figure 1.11 and compared with the real acoustic impedance.

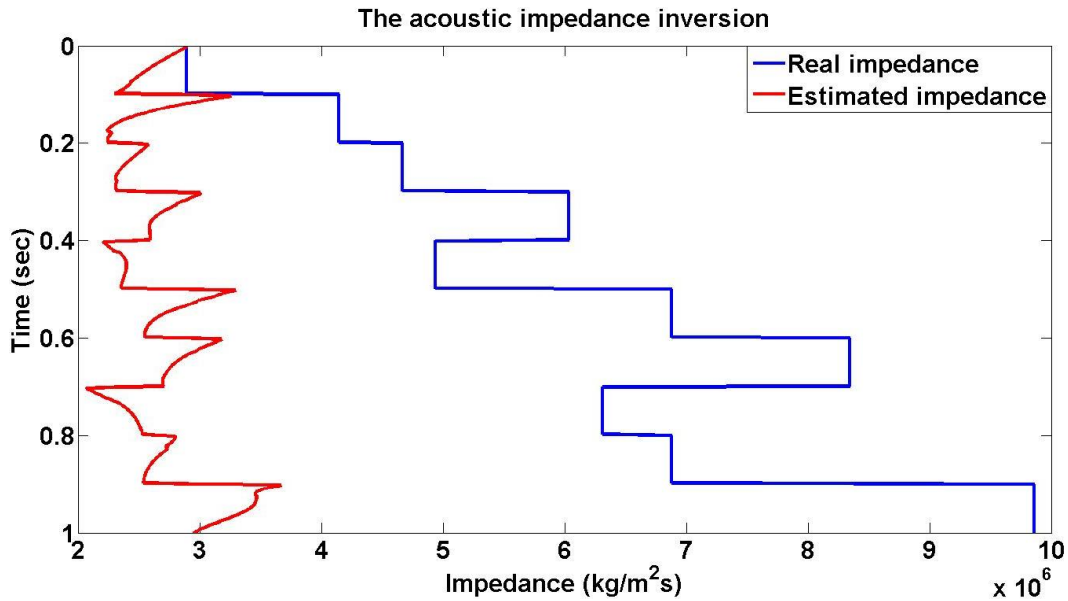


Figure 1.11 The acoustic impedance estimation computed from recursion formula compared with real estimation. The lack of low frequencies cause the misestimation of acoustic impedance.

The small errors in reflectivity estimation seems to be affecting significantly the impedance estimation. To understand why the acoustic estimation failed with using equation 1.19, it is good to look at the amplitude spectrum of both real and estimated reflectivity which the impedance computed from it. Figure 1.12 shows their amplitude spectrum in frequency domain. Except for frequencies below than 10 Hz, in the other frequencies both real and estimated reflectivity have nearly the same spectrum which means the low frequencies in the estimated data have not been properly recovered. Comparing two previous figures (Figure 1.11 and Figure 1.12) shows that the low frequency components determine the trend of data (Lindseth, 1979).

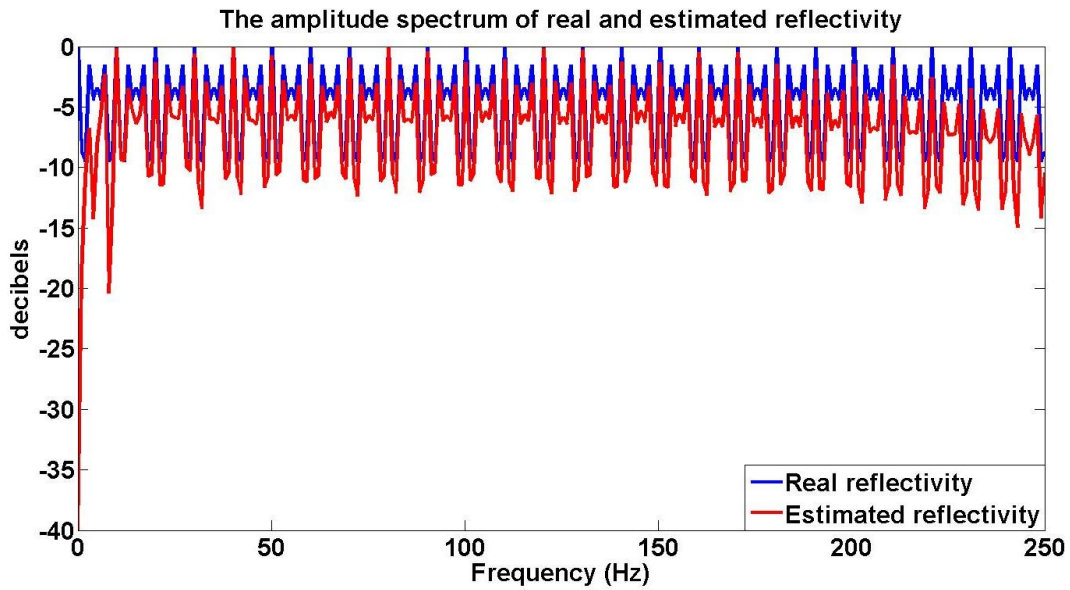


Figure 1.12 The amplitude spectrum of estimated reflectivity which is not broadband and its low frequency components have been removed.

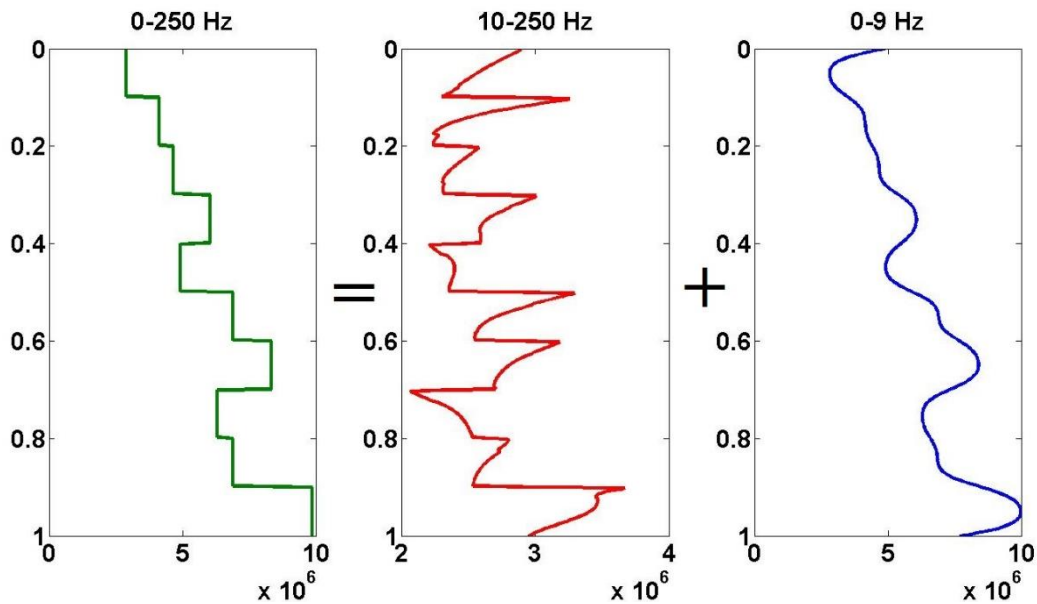


Figure 1.13 A broad band data may be considered to be the sum of a detailed data (10-250 Hz) and a gross data (0-9 Hz)

The deconvolution algorithm computes the reflectivity by estimating the embedded wavelet. Thus, the reason of the lack of low frequencies in estimated reflectivity can be found in estimated wavelet. Figure 1.13 shows the estimated wavelet in time domain and its amplitude

spectrum in frequency domain compared with the real wavelet. In the frequencies below than 10 Hz the differences can be seen. Note that based on equation 1.34 misestimation in amplitude spectrum of wavelet can causes the same frequency bandwidth reduction in the amplitude spectrum of estimated reflectivity.

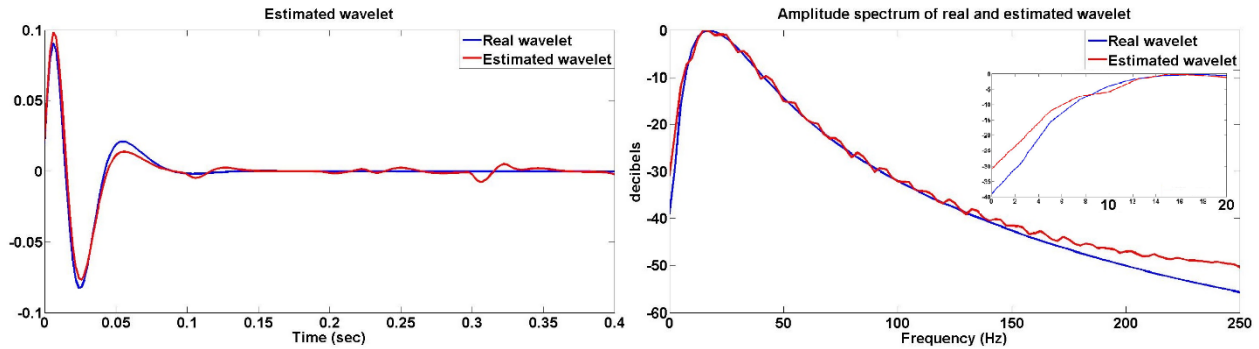


Figure 1.14 Estimated wavelet and its amplitude spectrum compared with source wavelet. The results in frequency domain shows in low frequency the real and estimated wavelets are not matching each other which is causing the lack of low frequencies in reflectivity estimations.

As shown, the loss of the low frequencies most greatly hampers interpretation of the derived acoustic impedance, and for this reason a number of methods for inserting those frequencies have been developed. Galbraith and Millington (1979) used the acoustic impedance measured at a nearby well. Lavergne and Willm (1977) and Lindseth (1979) both added low frequencies derived from velocity analysis. In 1996, Ferguson and Margrave created the BLIMP (BandLimited IMPedance) inversion algorithm which extracts the low frequency data from well log data. This algorithm has been used to extract the low frequency components from the real impedance and apply to the estimated impedance. BLIMP was created as an example of what has become standard practice to use well information to provide the low frequencies. The results illustrated in Figure 1.15.

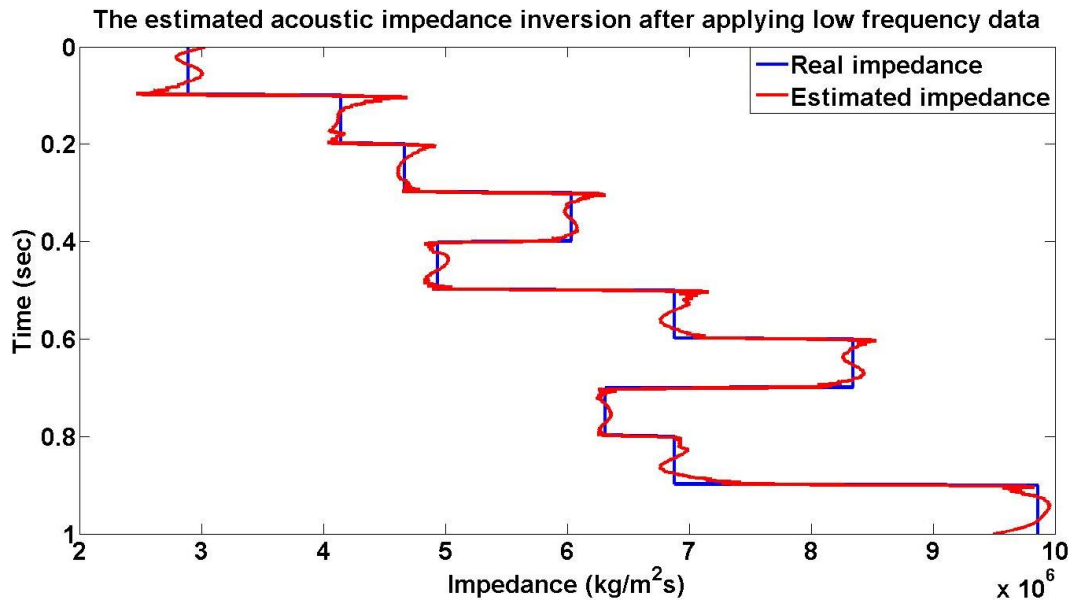


Figure 1.15 Recovering low frequency components using BLIMP algorithm with extracting the low frequency components from the real impedance.

The example here shows that even in a very simple case, the computed reflectivity is bandlimited because of the bandlimited property of wavelet and an apparent failure of the deconvolution algorithm to correctly estimate the low frequencies. In the real seismic data other effects such as noise contamination, multiples, transmission losses, complex subsurface structures as well as nonstationary effect can cause the wavelet estimation to become even more difficult. In the frequency domain deconvolution, the deconvolution method has been used here, there are number of assumptions need to be consider. One of the assumptions is that the spectrum of the reflectivity should be white. A white spectrum is one that has constant power at all frequencies, the same case represented here. However, Walden and Hosken (1985) showed that the most reflectivities from wells sourced all over the world do not have white spectra.

## 1.7 Overview of chapters

This thesis is presented in 5 chapters.

Chapter 2 will be focused on how the wavelet estimation process can be done. In this chapter the frequency domain deconvolution which is one of the deconvolution methods will be discussed and we will investigate if the smoother type is changed in the deconvolution operator how it can affect the reflectivity estimation.

In chapter 3 the Hussar well log data will be used and it will be essentially tried to design an operator to correct the errors of whitening deconvolution operator. This includes designing three different models and applying them to the normal incident synthetic seismic trace.

In chapter 4 the real seismic data will be introduced and then the effect of applying the color operators which designed in chapter 3 on seismic data will be discussed.

Chapter 5 will be summarized the conclusions from chapter 2-4.

## **1.8 MATLAB software**

The main software used in this thesis is MATLAB® which is a high-level programming language developed by MathWorks. This software is optimized for matrix algebra, which is ideal for seismic data. CREWES (Consortium of Research in Elastic Wave Exploration Seismology) developed a toolbox with a variety of processing, modeling and utility functions that can be used for seismic data processing. This toolbox was used extensively in this thesis.

## **CHAPTER TWO: FREQUENCY DOMAIN DECONVOLUTION AND REFLECTIVITY ESTIMATION PROCESS**

### **2.1 Introduction**

Seismic reflectivity estimation is aimed at obtaining the true underground reflection information and improving the seismic vertical resolution, which is mainly restricted by the bandlimited source wavelet. As mentioned previously, for stationary wavelet assumption, based on the convolutional model it is possible to estimate the reflectivity via deconvolution algorithm (Oldenburg et. al., 1983). This technique can be done by various algorithms. Frequency domain deconvolution (Margrave 2002), Wiener spiking deconvolution (Leinbach, 1995), Vibroseis deconvolution, Burg (maximum entropy) deconvolution (Burg, 1975) and Gabor deconvolution (Margrave and Lamoureux, 2002) are different types of deconvolution algorithms. The application of frequency domain deconvolution has been shown in the previous chapter for a very simple case. In this chapter, it will be demonstrated how frequency domain deconvolution method estimates the reflectivity via wavelet estimation.

### **2.2 Frequency domain deconvolution algorithm**

To start to create the deconvolution operator, a number of mathematical assumptions need to be set:

- The wavelet should be causal and minimum-phase.
- The wavelet spectrum should be smooth.
- The wavelet should be stationary.
- The reflectivity is assumed to be random, thus its amplitude spectrum is white.
- Any noise is additive, white and stationary.

The model based on these assumptions is illustrated in Figure 2.1. The reflectivity is random and the wavelet is minimum-phase with 15 Hz dominant frequency and 2 milliseconds sample rate. The normal incident synthetic seismic trace has been created using equation 1.21.

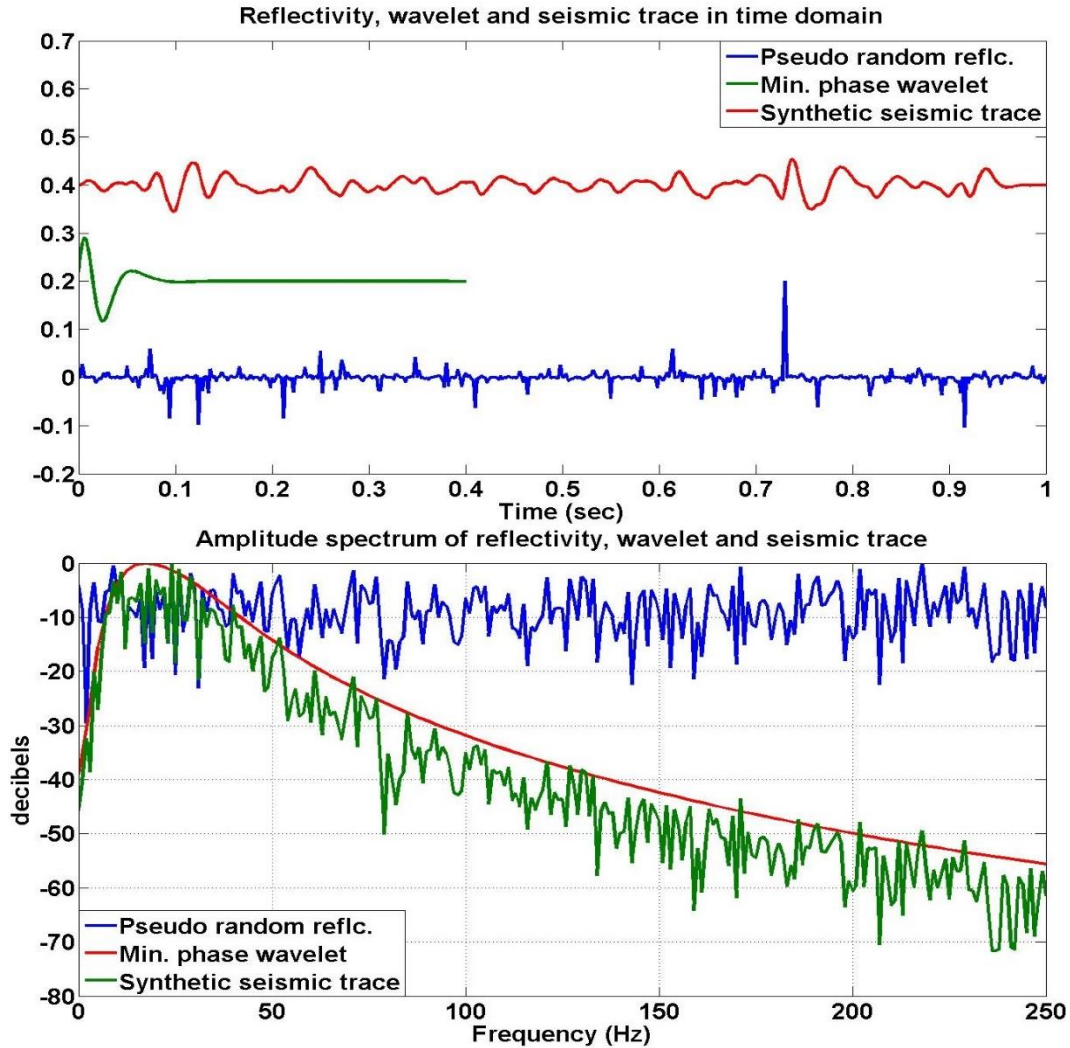


Figure 2.1 The normal incident synthetic seismic trace created from pseudo random reflectivity and minimum-phase wavelet.

Comparing the amplitude spectrum of seismic trace and the wavelet shows that the amplitude spectral shape of the seismic trace is essentially similar to the spectral shape of the unknown wavelet which means the amplitude spectrum of the unknown wavelet can be estimated

by smoothing the amplitude spectrum of the seismic trace. Mathematically, the perfect deconvolution operator can be defined as (Oldenburg et. al., 1983)

$$w(t) \bullet d(t) = \delta(t), \quad 2.1$$

where  $d(t)$  is the convolutional inverse of  $w(t)$  and  $\delta(t)$  is delta Dirac function. By substituting the inverse of  $w(t)$  into equation 1.21,  $r(t)$  becomes

$$r(t) = s(t) \bullet d(t), \quad 2.2$$

where  $r(t)$  is the exact reflectivity function. But in practice, because of the bandlimited nature of wavelets and the unavoidable presence of noise, even if we could find  $d(t)$  as a function to make equation 2.1 equal to  $\delta(t)$ , such an operator would simply produce noise at frequencies where noise dominates signal. This important fact leads us to the concept that the estimated wavelet is never exactly the same as the true wavelet. Mathematically, the deconvolved seismic trace can be written as

$$s_d(t) = r(t) \bullet w_d(t), \quad 2.3$$

where  $s_d(t)$  is the deconvolved trace which is also the estimated reflectivity, and  $w_d(t)$  can be represented as

$$w_d(t) = w(t) \bullet d(t), \quad 2.4$$

where  $w_d(t)$  is the embedded wavelet after deconvolution and is an approximation of a Delta function. The wavelet estimated by deconvolution is the convolutional inverse of  $d(t)$  and will always differ from the true wavelet. As shown previously, Figure 1.14 is illustrating an example of an actual wavelet and its estimation in the time and frequency domain. According to the Figure 2.1 the equation 1.34 leads to

$$|S(f)| \approx |R(f)||W(f)|, \quad 2.5$$

where the vertical bars (e.g.  $|S(f)|$ ) denote absolute values or amplitude spectra. Note that by using amplitude spectra, we are discarding the possibility of estimating the wavelet phase directly from the data. The white reflectivity assumption means

$$|\overline{R(f)}| \approx 1, \quad 2.6$$

where the overbar indicates smoothing. Therefore, the amplitude spectrum of an estimated wavelet can be expressed as

$$|W(f)|_{est} = \overline{|S(f)|} \approx |W(f)|. \quad 2.7$$

The equation 2.7 demonstrates that the amplitude spectrum of estimated wavelet is similar to smoothing of amplitude spectrum of seismic trace. There are many possible smoothing techniques and we postpone this discussion until later. Because, the deconvolution algorithm tries to remove the effect of wavelet from seismic trace, the amplitude spectrum of the deconvolution operator is just the algebraic inverse of equation 2.7

$$|D(f)| = |W(f)|_{est}^{-1} = \frac{1}{|W(f)|_{est}} \quad 2.8$$

In equation 2.8 if the wavelet is very weak at some frequency, then it is likely that noise is significant at that frequency. Therefore, inverting the wavelet at such frequencies will cause unacceptable noise enhancement. It is customary to add a small constant to the estimated wavelet's amplitude spectrum prior to inversion to avoid division by zero (i.e. singularities). Then the equation 2.8 becomes

$$|D(f)| = \frac{1}{|W(f)|_{est} + \mu A_{max}} \quad 2.9$$

where  $\mu$  is called stability factor or white-noise constant and is a small positive number usually between 0.01 and 0.000001 and  $A_{max} = \max(|W(f)|_{est})$ . Once the amplitude spectrum of deconvolution operator is calculated, its phase spectrum needs to be computed. One of the aforesaid assumptions was that the wavelet should be minimum-phase. Notice that the minimum-phase wavelet does not refer to a particular phase spectrum which, if preserved, maintains a dataset's minimum-phase. Instead, the minimum-phase refers to a particular mathematical relationship existing between the amplitude and phase spectra so that knowledge of either one is sufficient to compute the other one. Because of causality property of minimum-phase signal, its real and imaginary parts form a Hilbert transform pair such that (Margrave, 2002)

$$\begin{aligned} F_r(f) &= \frac{1}{\pi} \int_{-\infty}^{\infty} \frac{F_i(\bar{f})}{f - \bar{f}} d\bar{f} \\ F_i(f) &= \frac{-1}{\pi} \int_{-\infty}^{\infty} \frac{F_r(\bar{f})}{f - \bar{f}} d\bar{f}, \end{aligned} \quad 2.10$$

where  $F_r(f)$  and  $F_i(f)$  are real and imaginary part of  $F(t)$  respectively. He also showed, under certain circumstance instead of using the real and imaginary part of minimum-phase signal the amplitude and phase spectrum of it can be relate each other as:

$$\phi(f) = H(\ln(A(f))), \quad 2.11$$

where  $\phi(f)$  and  $A(f)$  are phase and amplitude spectrum of minimum-phase signal respectively and  $H$  is the Hilbert transform. Equation 2.11 is the relationship between phase spectrum and amplitude spectrum and using this equation the phase spectrum of deconvolution operator becomes

$$\phi_D(f) = H(\ln(|D(f)|)). \quad 2.12$$

Finally, the calculated amplitude spectrum and phase spectrum can easily transform from frequency domain into the time domain via inverse Fourier transform.

So far, the deconvolution operator has been calculated for noise-free seismic data. However, the seismic data is always contaminated with different type of noises depending on the field properties and the acquisition instruments quality. The reasonable model for random noise is that should be additive, white, and stationary. Here the term ‘stationary’ means that the statistical properties of the noise (its mean and standard deviation) are not time variant. If the seismic trace contaminated with such random noise, the equation 1.21 becomes

$$s(t) = r(t) \cdot w(t) + n(t), \quad 2.13$$

and its amplitude spectrum in the frequency domain becomes

$$S(f) = R(f)W(f) + N(f). \quad 2.14$$

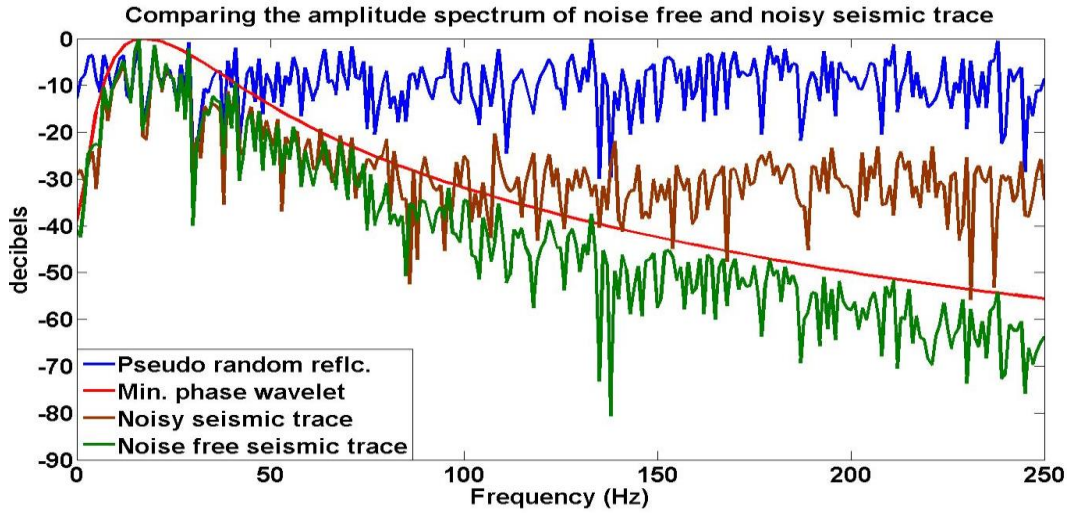


Figure 2.2 The amplitude spectrum of noisy seismic data compared with noise-free data. There is an specific frequency area which the noisy and noise free data are the same and can use the same method to extract deconvolution operator.

Figure 2.2 shows that for a specific range of frequency ( $f_{\min} \leq f \leq f_{\max}$ ) the  $R(f)W(f)$  term dominates over  $N(f)$  and the noisy and noise-free seismograms are closely similar which

means for this frequency region all previous procedures to compute the deconvolution operator are valid. All we need to do is to apply low-cut and high-cut frequency filters to remove the data lower than  $f_{\min}$  and higher than  $f_{\max}$ . This filtering process makes the data more bandlimited and so causing the reflectivity estimation less accurate.

As discussed, to calculate the deconvolution operator, the amplitude spectrum of seismic trace must be smoothed. On the other hand, transforming data from the time domain to the frequency domain by Fourier transform leads data to be expanded in negative and positive frequencies. However, the negative frequencies are often suppressed because they are redundant (they can be calculated from the positive frequencies) and if we try to smooth the spectrum in only positive frequencies, the smoother gets significant errors at very low frequencies. Thus the power spectrum of data should be unwrapped first, then smoothed and then wrapped again for the inverse FFT.

There are two common methods to smooth the data: convolutional smoothing and smoothing by data fitting. The convolutional smoothing can be done for instance with moving average (boxcar) and Gaussian function which both are the same but differing in the nature of the convolution function. Furthermore, since the convolutional smoothing becomes windowing in the time domain, it seems plausible that we might wish to have a convolutional frequency smoother whose width changes with frequency. In this study two different convolutional smoothers, boxcar and Gaussian, with constant and frequency dependent length will be examined and in the next chapter the data fitting smoother will be used to design color operator.

## 2.3 Different smoothing methods

### 2.3.1 Boxcar smoother (BS)

The simplest form of smoothing is the "moving average" which simply replaces each data value with the average of neighboring values. To avoid shifting the data, it is best to average the same number of values before and after where the average is being calculated. In equation form, the moving average is calculated by

$$\bar{x}[i] = \frac{1}{2M+1} \sum_{j=-M}^M x[i+j]. \quad 2.15$$

Another term for this kind of smoothing is "boxcar smoothing". It can be implemented by convolving the input data with a box-shaped pulse with the length of  $n = 2M + 1$  which implies  $n$  should be an odd number. The smoother with the length of  $n$  when applied to the input data, those points of data are located inside of smoother, are used to compute the average (Figure 2.3).

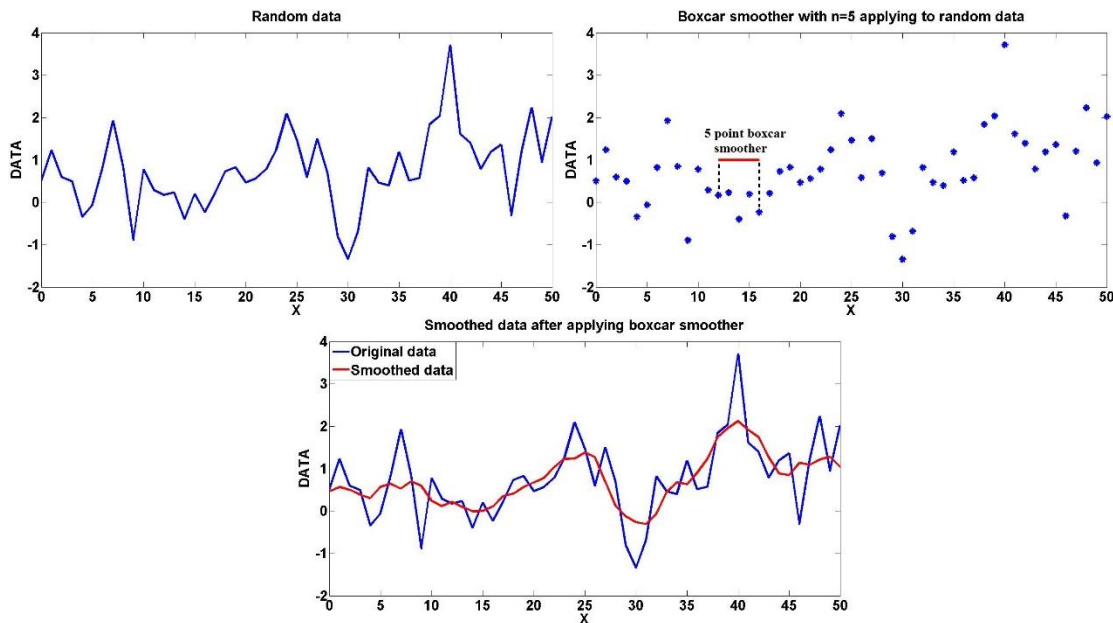


Figure 2.3 Boxcar smoothing procedure for the random dataset.

### 2.3.2 Constant Gaussian smoother (CGS)

The Gaussian smoother is another type of convolutional smoother which is based on Gaussian distribution. In one dimension, the Gaussian function of zero mean is

$$G(x) = \frac{1}{\sqrt{2\pi\sigma^2}} e^{-\frac{x^2}{2\sigma^2}}, \quad 2.16$$

where  $\sigma$  is the standard deviation of the distribution. Shown graphically, we see the familiar bell shaped Gaussian distribution (Figure 2.4).

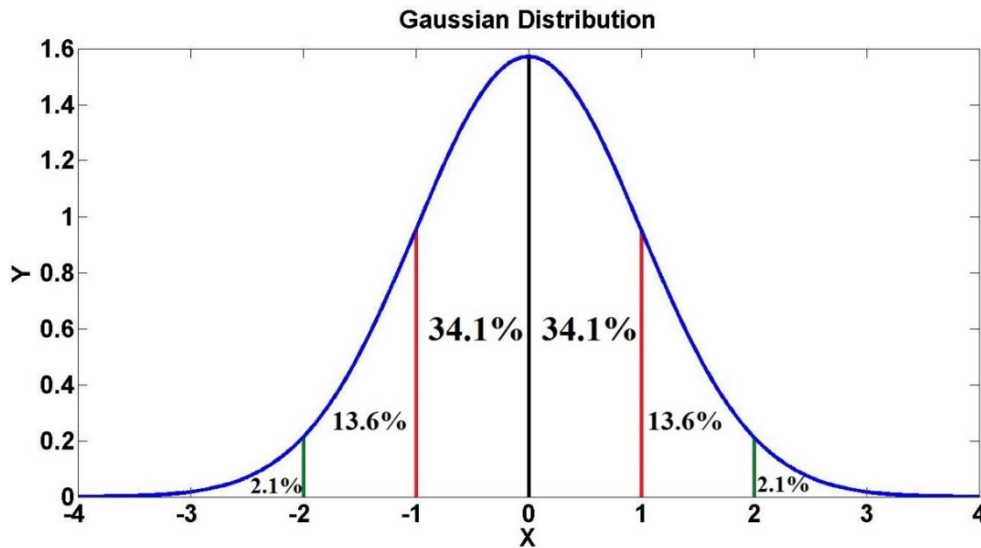


Figure 2.4 Gaussian distribution for using Gaussian smoother.

The standard deviation of the Gaussian function plays an important role in its behavior. The above figure shows that the values located between  $\pm\sigma$  account for 68% of the set, while  $\pm 2\sigma$  from the mean account for 95% ( $2 \times 13.6 + 2 \times 34.1$ ), and  $\pm 3\sigma$  account for 99.7% so the distribution has approached very close to zero at about three standard deviations from the mean. This means we can normally limit the kernel size to contain only values within  $\pm 3\sigma$  of the mean. If the value of  $\sigma$  (i.e. Gaussian smoother's length) remains constant during the applying Gaussian distribution on specific data, it is called Constant Gaussian Smoother (CGS).

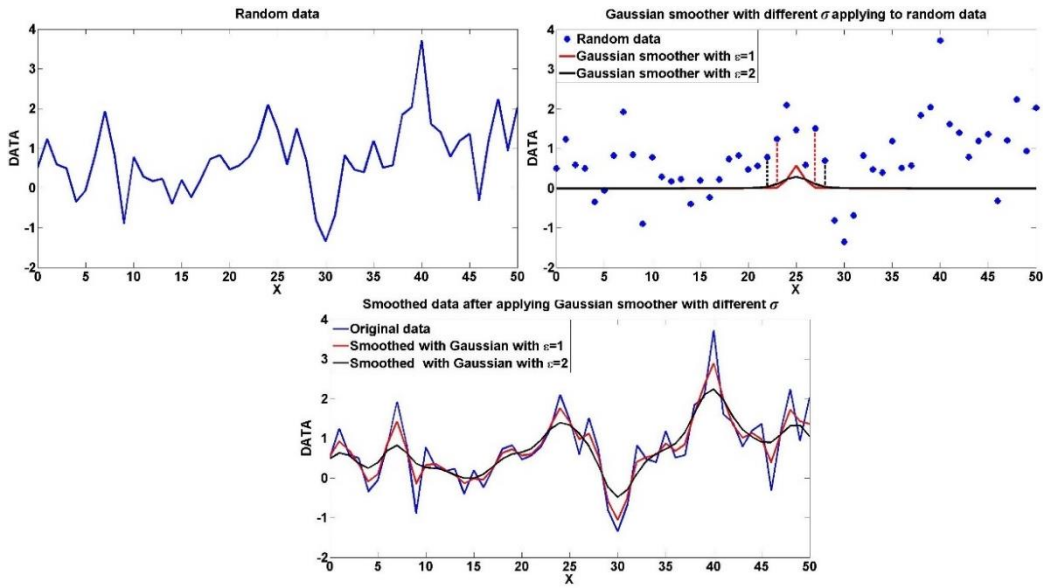


Figure 2.5 Constant Gaussian smoothing procedure for the random dataset.

In the above two Gaussian smoothers with different  $\sigma$ , one with  $\sigma = 1$  and the other one with  $\sigma = 2$ , are centered at the middle data point and have been applied to the indicated area. The same procedure is applied to every single point and the final smoothed data are shown in the last figure.

### 2.3.3 Frequency-Dependent Gaussian Smoother (FDGS)

If the smoother length (the value of  $\sigma$ ) varies with frequency, we call it frequency-dependent Gaussian smoothing (FDGS).

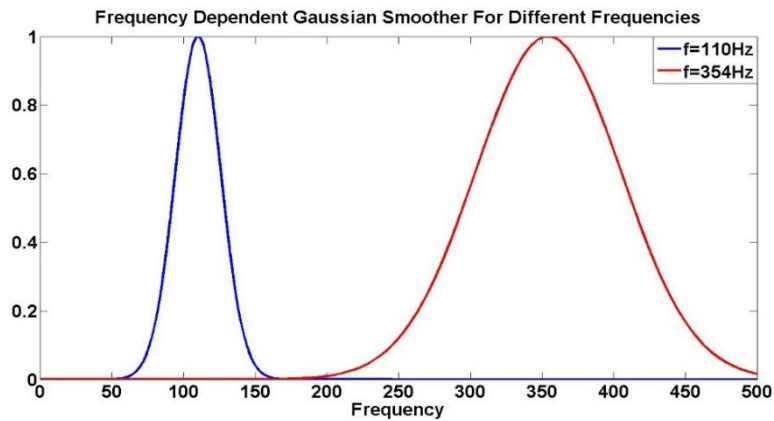


Figure 2.6 Schematic of changing Gaussian smoother length with frequency.

## 2.4 The effect of different smoothers on frequency domain deconvolution

To investigate how these different smoothers can affect the deconvolution results, the pseudo random reflectivity which was mentioned in this chapter has been used. A normal incident synthetic seismic trace has been created by convolving these random data with 15 Hz minimum-phase wavelet with 2 milliseconds sample rate (Figure 2.1).

### 2.4.1 The results with Boxcar smoother

The first choice of deconvolution operator uses the boxcar smoother. As mentioned before, the number of points of boxcar function is the smoother length. First we need to choose the best smoother length. To do this, a series of tests were conducted in which the smoother length was varied over a reasonable range and the resulting reflectivity estimates were crosscorrelated with the known reflectivity. The results, plotted in Figure 2.7 shows the best length of smoother in frequency for the normal incident synthetic seismic trace to be about 6 Hz. Since the length of the synthetic is  $T = 1\text{sec}$ , the smoother width in Hz is related to the number of points in the smoother by

$$f_{smooth} = n_{smooth} \Delta f = \frac{n_{smooth}}{T} \quad 2.17$$

where  $f_{smooth}$  and  $n_{smooth}$  are length of smoother in frequency and smoother length in point number respectively. Also, Figure 2.8 illustrates the smoothed power of amplitude spectrum of seismic trace with the appropriate boxcar smoother (with length of 6 Hz) in frequency domain.

The deconvolved trace which is the estimated reflectivity is shown in Figure 2.9 in time domain and also its amplitude spectrum in Figure 2.10.

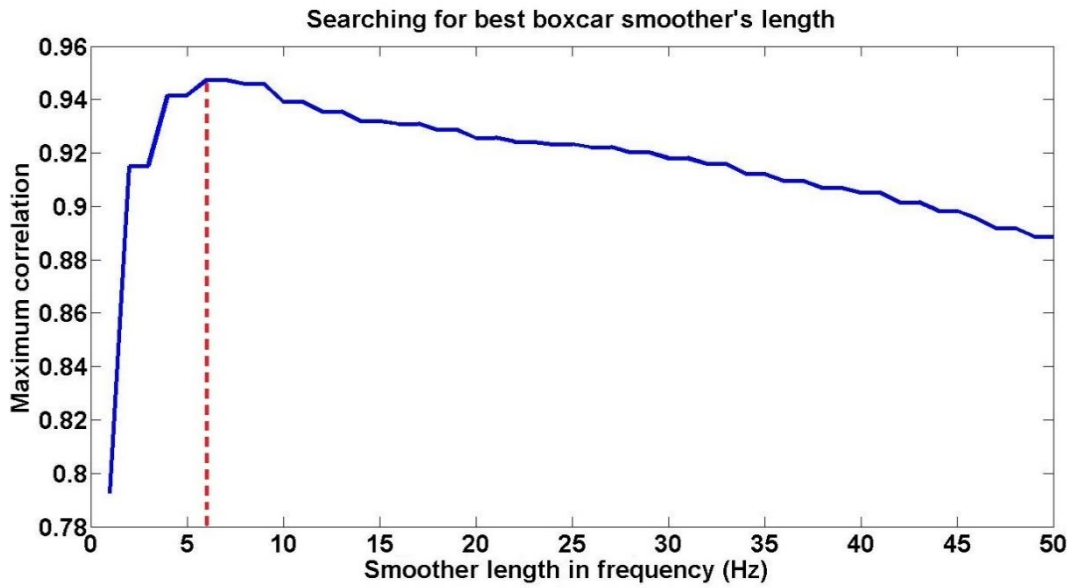


Figure 2.7 Searching the optimum value for the boxcar smoother length in the frequency domain. The plot shows the best choice for the smoother length is 6Hz.

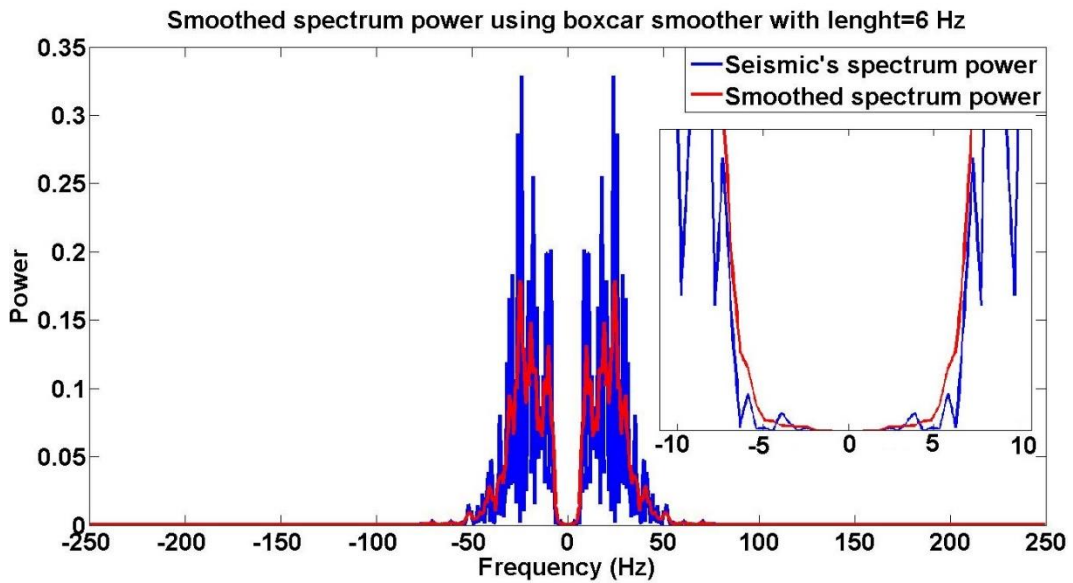


Figure 2.8. Smoothing the power of seismic spectrum using boxcar smoother with 6Hz of length.

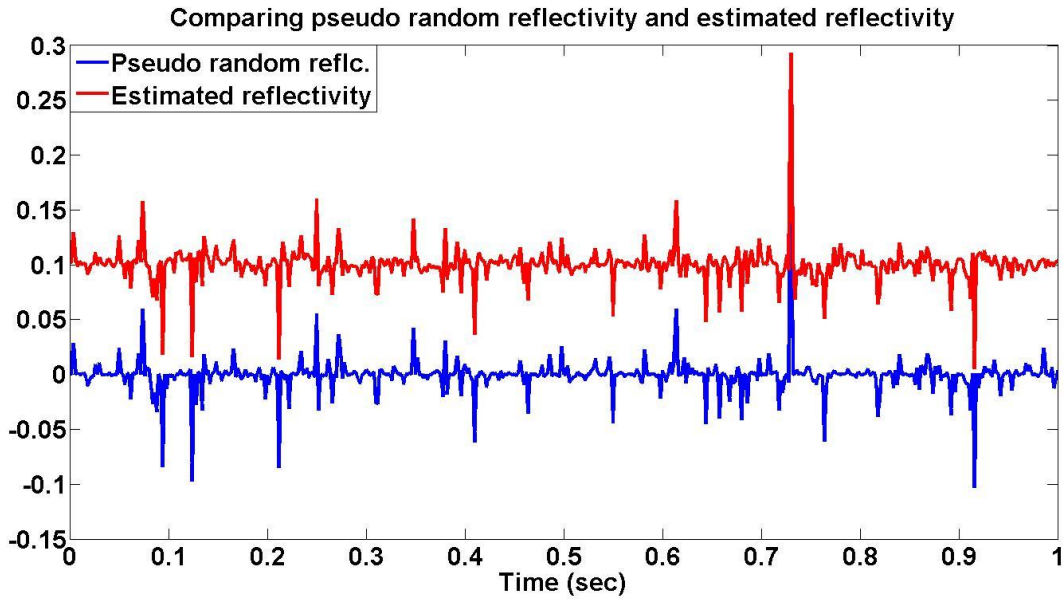


Figure 2.9. The result of reflectivity estimation using the boxcar smoother with 6Hz of length.

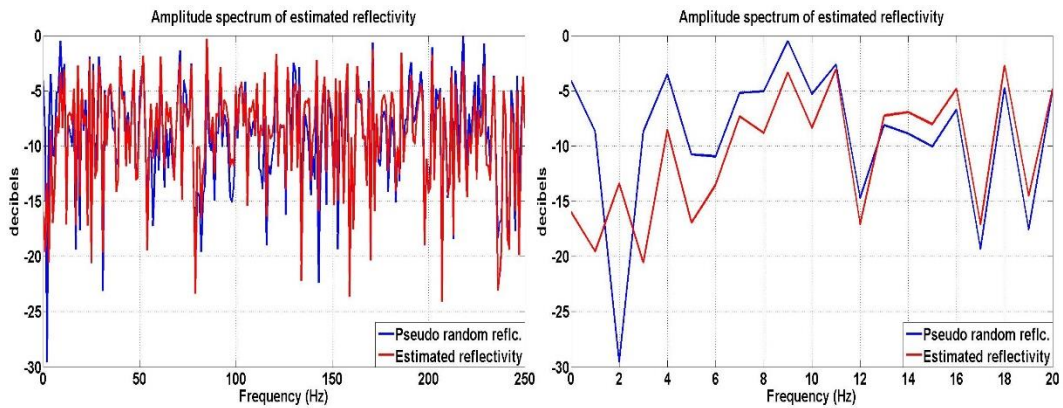


Figure 2.10. Comparing the amplitude spectrum of pseudo random reflectivity and its estimation in frequency domain. Zooming the results in low frequencies (0-20Hz) demonstrate the misestimation of the reflectivity after deconvolution with boxcar smoother.

#### 2.4.2 The results with constant Gaussian smoother

The next option of smoother in deconvolution operator is a constant Gaussian smoother. As mentioned before, the Gaussian smoother is defined by equation 4 and its length indicated by  $\sigma$ .  $\sigma$  is half width of Gaussian distribution which the value of Gaussian reaches to  $e^{-1/2}$  of its maximum. The mathematical equation of Gaussian smoother we are using in this study is

$$\bar{A}_j = \frac{\sum_k A_k g_{j-k}}{\sum_k g_k} \quad 2.18$$

where  $A_k$  is the unsmoothed amplitude spectrum,  $\bar{A}_j$  is the smoothed spectrum, and

$$g_k = e^{-k\Delta f^2/\sigma_f^2} \quad 2.19$$

in which  $\sigma_f$  is the standard deviation in Hz.

Here  $\sigma_f$  is the length of smoother in frequency. Again it is possible to search the best length of smoother for deconvolution algorithm. The curve of maximum correlation between deconvolved trace and reflectivity and length of smoother is illustrated in Figure 2.11. According to this figure the maximum correlation will be achieved if the length of smoother is 11 Hz.

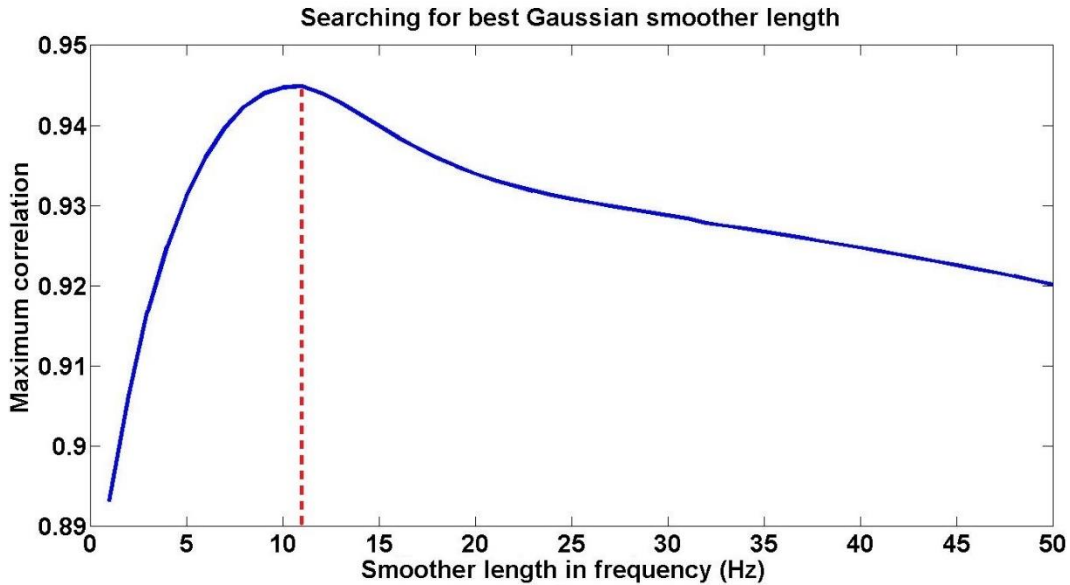


Figure 2.11. Searching the optimum value for the Gaussian smoother length in the frequency domain. The plot shows the best choice for the smoother length is 11Hz.

If the Gaussian distribution with 11 Hz length is chosen as the smoother, the smoothed amplitude spectrum of seismic trace became as Figure 2.12.

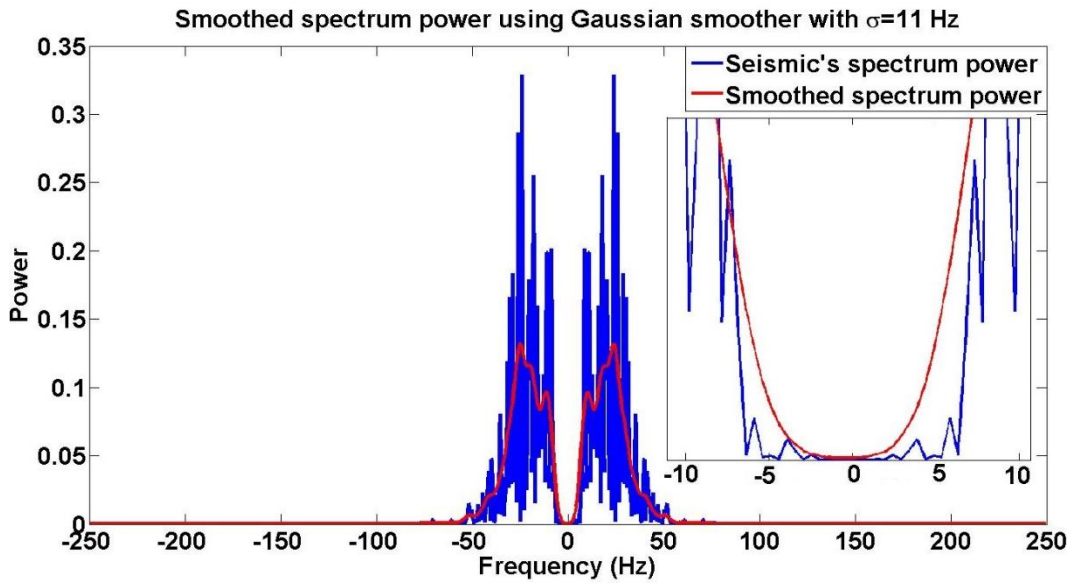


Figure 2.12. Smoothing the power of seismic spectrum using Gaussian smoother with 11Hz of length.

Applying this deconvolution operator to the seismic data gives us the deconvolved trace or the estimated reflectivity. The result has been shown in Figure 2.13 in time domain and its amplitude spectrum in Figure 2.14.

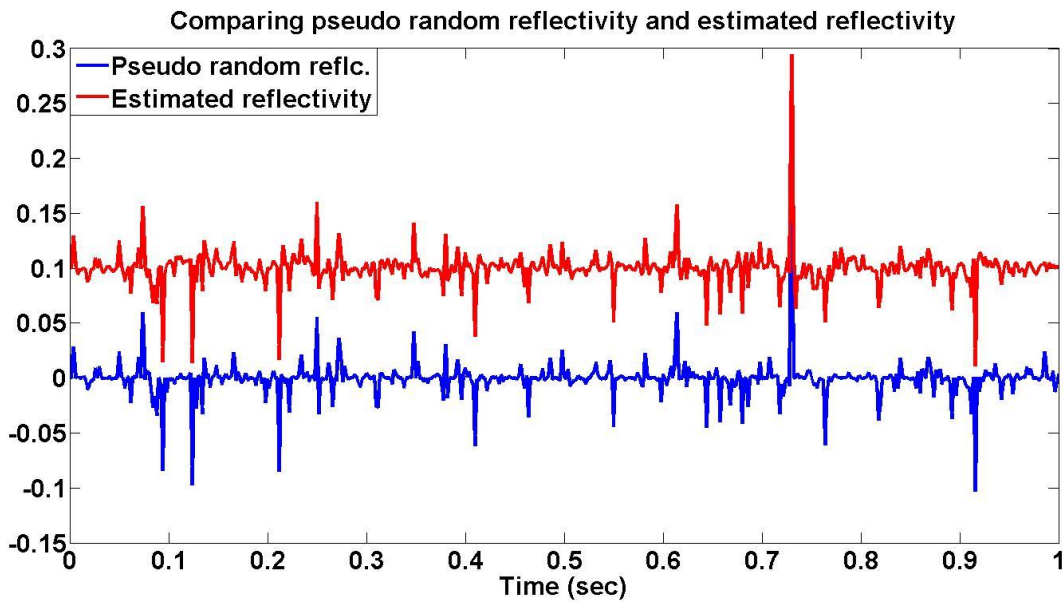


Figure 2.13. The result of reflectivity estimation using the constant Gaussian smoother with 11Hz of length.

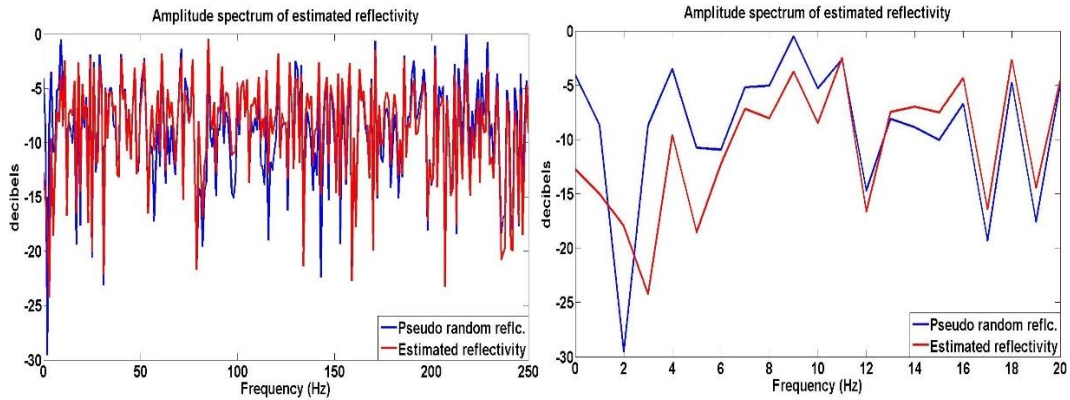


Figure 2.14. Comparing the amplitude spectrum of pseudo random reflectivity and its estimation in frequency domain. Zooming the results in low frequencies (0-20Hz) demonstrate the misestimation of the reflectivity after deconvolution with constant Gaussian smoother.

### 2.4.3 The results with frequency dependent Gaussian smoother

As previously mentioned, the idea of changing smoother length with frequency comes from the consideration that spectral smoothing must be time-domain windowing and lower frequencies should require longer temporal windows. This implies that the frequency domain smoother should decrease as frequency tends towards zero. So we will define a smoother length which becomes short in low frequencies and long in high frequencies. We do this in a similar fashion to equation 2.19 except that we set  $\sigma_f$  to depend on frequency according to

$$\sigma_f = \frac{f}{n} = \frac{k\Delta f}{n} \quad 2.20$$

where  $n$  is a deconvolution input parameter and indicates the rate of variation of smoother length and its best value can be found similarly to the two previous methods. Figure 2.15 shows the maximum correlation between reflectivity and deconvolved trace versus  $n$ .

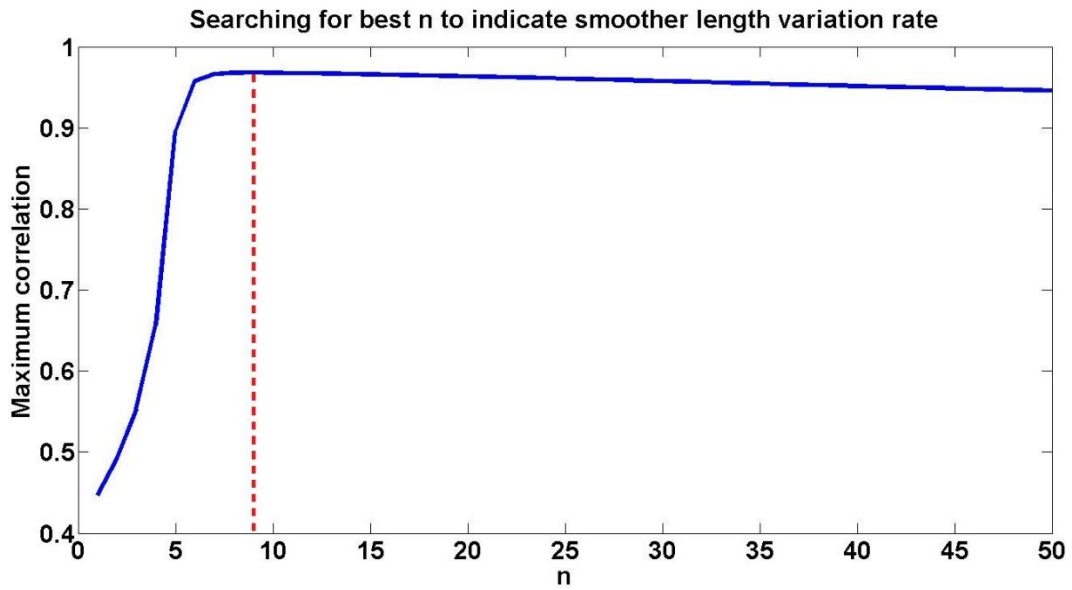


Figure 2.15. Searching the optimum value for  $n$  in frequency dependent Gaussian smoother length.  $n$  is a deconvolution input parameter and indicates the rate of variation of smoother length

This figure shows that the best value for  $n$  is 9. So the smoother length can be varied by  $\frac{f}{9}$

in different frequencies. For instance the Gaussian distribution is shown for 20Hz and 150 Hz in

Figure 2.16.

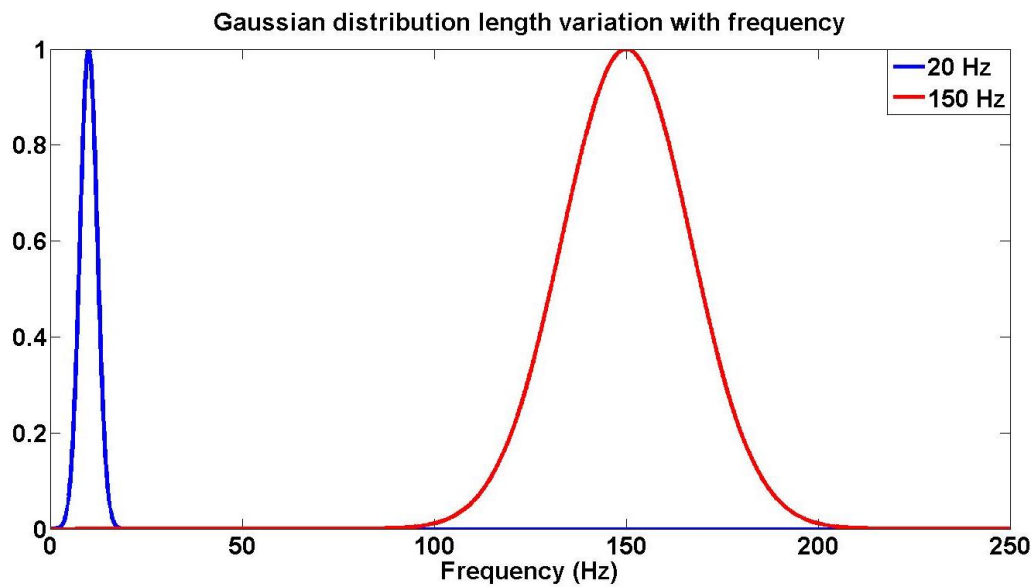


Figure 2.16. Gaussian distribution length variation with frequency. Smoother length becomes short in low frequencies and long in high frequencies.

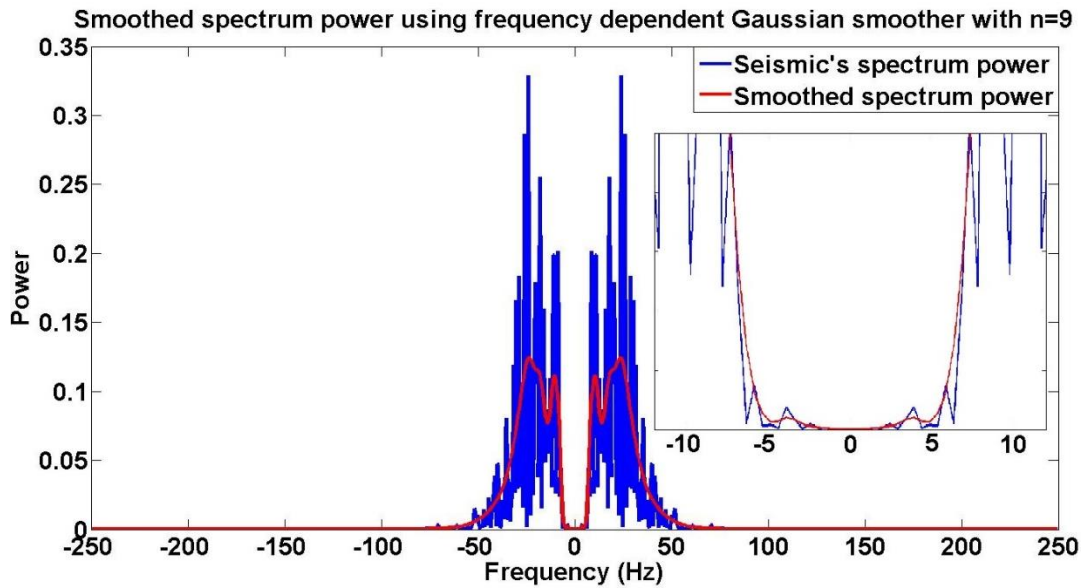


Figure 2.17. Smoothing the power of seismic spectrum using frequency dependent Gaussian smoother with  $n = 9$ .

The result of applying deconvolution operator with frequency dependent Gaussian smoother to the seismic data to calculate the reflectivity estimation shows on Figure 2.18 and also its amplitude spectrum on Figure 2.19.

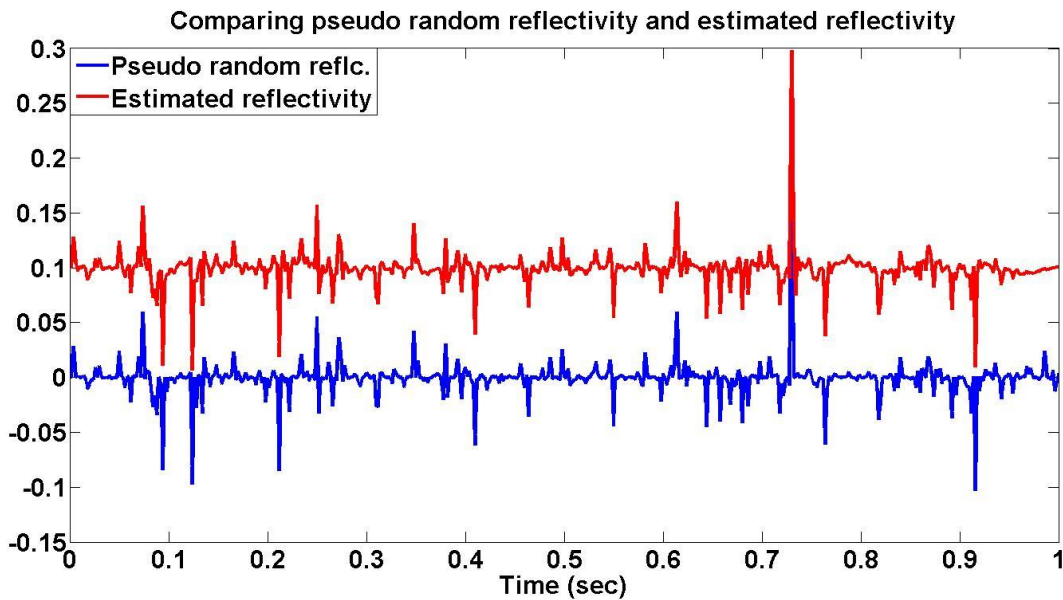


Figure 2.18. The result of reflectivity estimation using the frequency dependent Gaussian smoother with  $n = 9$ .

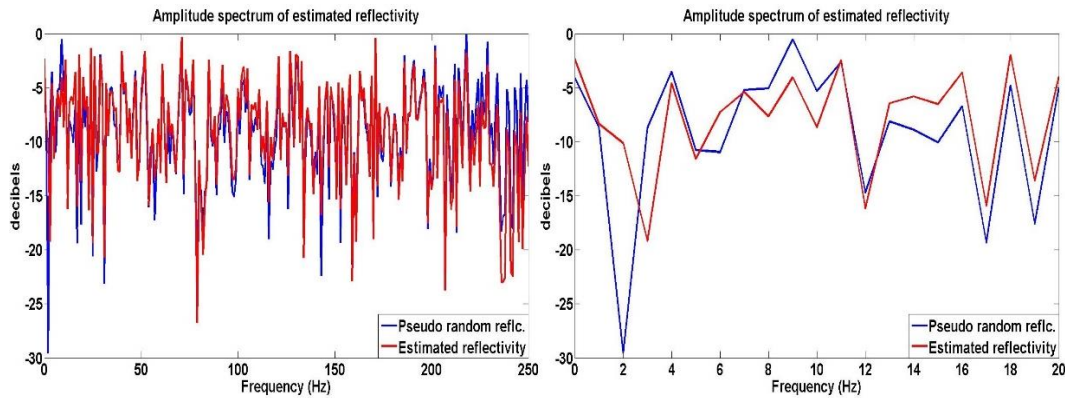


Figure 2.19. Comparing the amplitude spectrum of pseudo random reflectivity and its estimation in the frequency domain. Zooming the results in low frequencies (0-20Hz) demonstrates the misestimation of the reflectivity after deconvolution with a frequency-dependent Gaussian smoother.

Comparing the results of three different techniques, especially their amplitude spectrum results, shows that changing the smoother type can affect the recoverable frequency band in estimated reflectivity. The results show that using the frequency-dependent Gaussian smoother in the deconvolution algorithm contains more frequency information compared to two other smoother types. The result of maximum correlation between estimated reflectivity and real reflectivity is presented in Table 2.1, which can show the differences.

Smoother type	Boxcar smoother	Gaussian smoother	Frequency dependent Gaussian smoother
Maximum correlation	0.9473	0.9449	0.9681

Table 2.1 The maximum correlation values between pseudo random reflectivity and estimated reflectivity calculated from different deconvolution algorithms. The values show that the choice of frequency-dependent Gaussian smoother can be the best option.

Computing the acoustic impedance can be helpful to investigate the effect of using different smoothers in the deconvolution algorithm. Figure 2.20 shows the plot of impedance estimation calculated from the recursion formula (equation 1.19) from each deconvolution algorithm. As can be seen from this figure, in the frequency domain deconvolution algorithm when the seismic data are

smoothed with frequency dependent Gaussian smoother, the impedance results are significantly improved. The result shows in this case (pseudo random reflectivity) by using the frequency dependent Gaussian smoother not only the estimated impedance contains more details (high frequencies), also it contains the background trend (low frequencies). However, as it will be seen in the next two chapters in the real case where the spectrum of the reflectivity is non-white (colored) and hence, one of the deconvolution assumptions is not met, the reflectivity estimation becomes more challenging and that will show that the errors involved in smoothing are not as important as those created by ignoring spectral color.

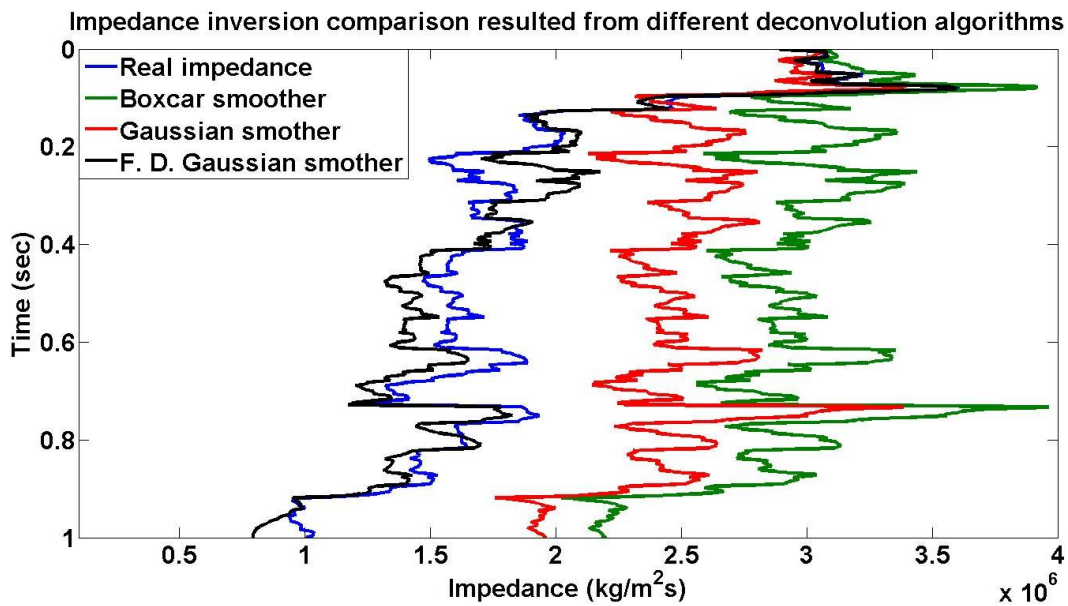


Figure 2.20. Acoustic impedance estimation which used different smoothers in their deconvolution algorithms.

## 2.5 Summary

- Seismic reflectivity estimation is aimed at obtaining the true underground reflection information and improving the seismic vertical resolution, which is mainly restricted by the bandlimited source wavelet.
- Frequency domain deconvolution method assumes some fundamental assumptions such as:

- The wavelet should be causal and minimum-phase.
  - The wavelet spectrum should be smooth.
  - The wavelet should be stationary.
  - The reflectivity is assumed to be random, thus its amplitude spectrum is white.
  - Any noise is additive, white and stationary.
- The minimum-phase wavelet does not refer to a particular phase spectrum which, if preserved, maintains a dataset's minimum-phase. Instead, the minimum-phase refers to a particular mathematical relationship existing between the amplitude and phase spectra so that knowledge of either one is sufficient to compute the other one. The mathematical relation between phase spectrum and amplitude spectrum can be found in equation 2.12.
  - To calculate the frequency domain deconvolution operator, the amplitude spectrum of seismic trace must be smoothed to get the wavelet estimation. This can be done with different smoother types. Boxcar smoother, constant Gaussian smoother and frequency dependent Gaussian smoother have been used.
  - Applying different frequency domain deconvolution operators to the pseudo random data demonstrate significant improvement in impedance results when the frequency dependent Gaussian smoother has been used (Figure 2.20).

## CHAPTER THREE: MINIMUM-PHASE COLOR OPERATOR

### 3.1 Introduction

In September 2011, CREWES with cooperation of Husky Energy initiated a seismic experiment with the goal of pushing the low-frequency content of seismic down as low as possible. This project was located near Hussar, Alberta, which is about 100km east of Calgary, Alberta. The line was 4.5km long and intersected three wells, 12-27, 14-27 and 14-35, shown in Figure 3.1. The Figure 3.2, Figure 3.3 and Figure 3.4 illustrate the P-wave velocity log, density log and calculated reflectivity for each mentioned wells. Note that for all three wells the logs start from around 200 meter depth and as we shall see later, for better tying between the synthetic data and the seismic data, an overburden model needs to be added at top of each well.

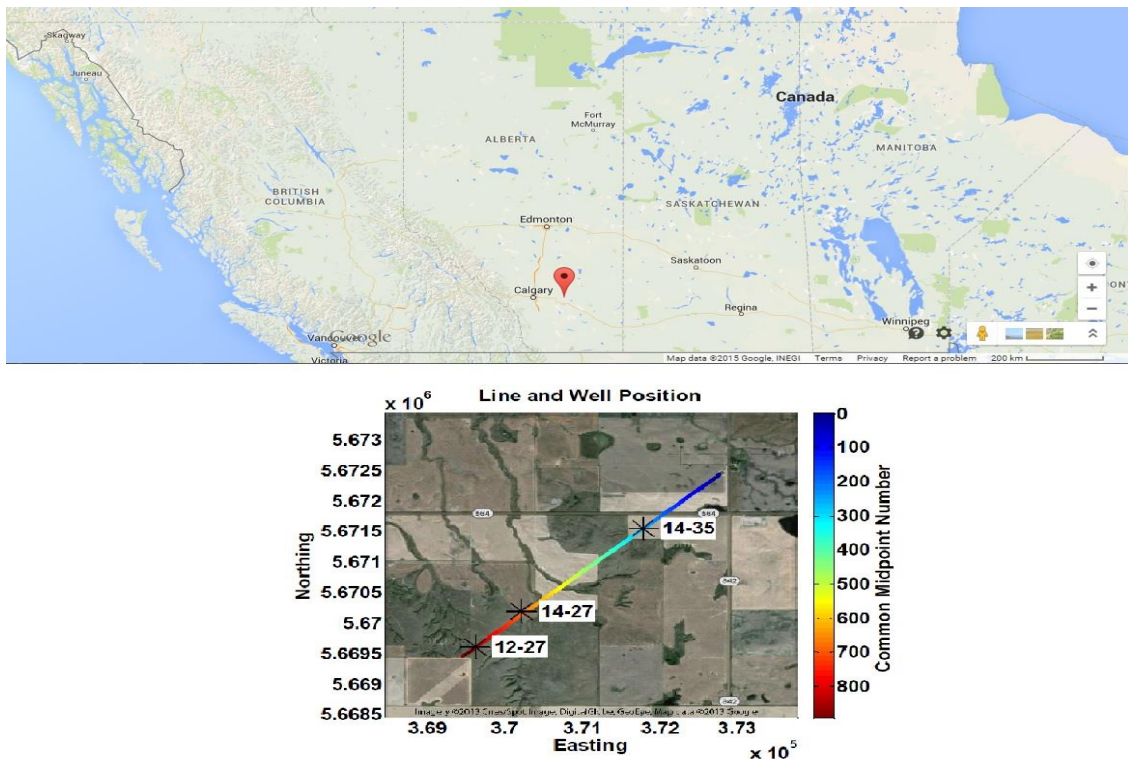


Figure 3.1. (top) Hussar is located at east of Calgary, Alberta (Google map) and (bottom) the location of the line and wells (Heather Lloyd, 2013).

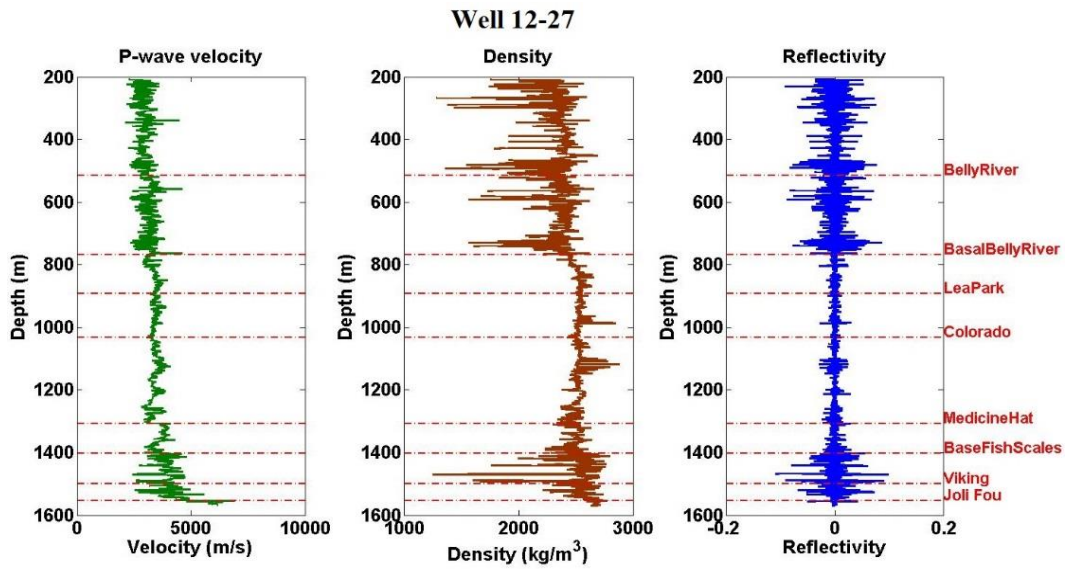


Figure 3.2. The P-wave velocity log and density log of well 12-27 from Hussar experiment located at east of Calgary as well as its reflectivity calculated form equation 1.13.

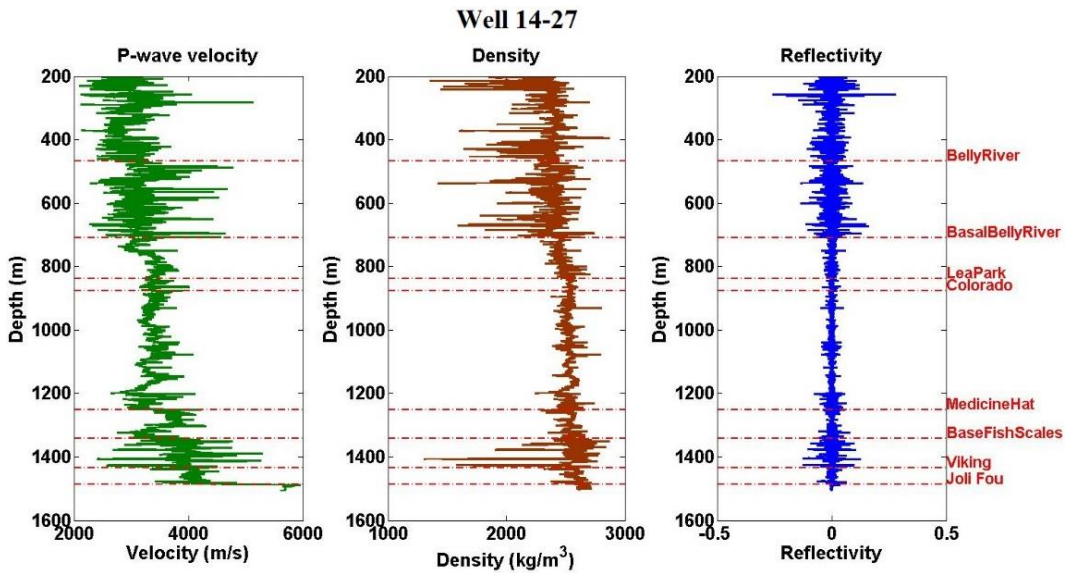


Figure 3.3. The P-wave velocity log and density log of well 14-27 from Hussar experiment located at east of Calgary as well as its reflectivity calculated form equation 1.13.

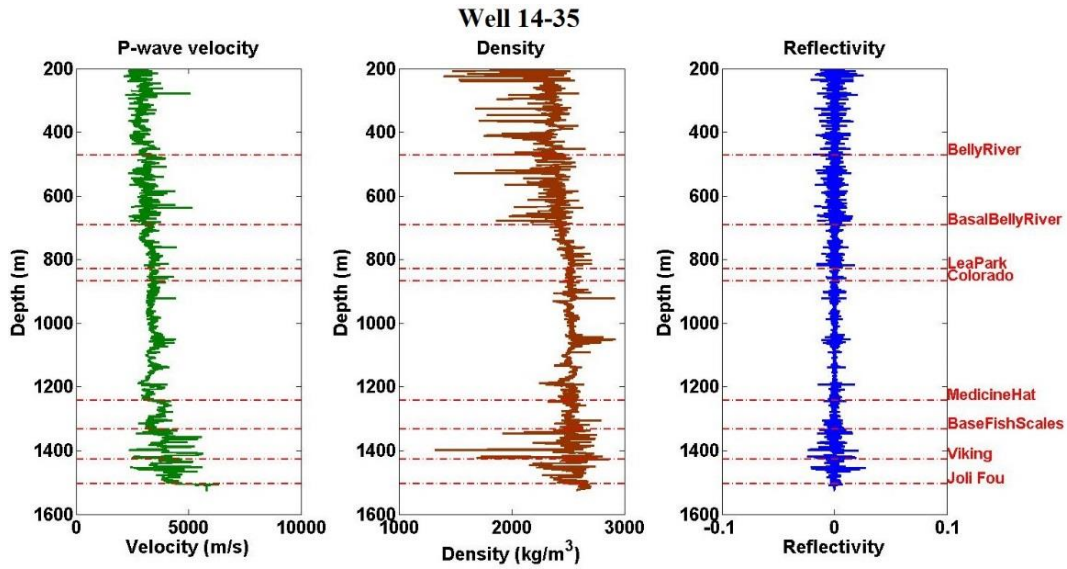


Figure 3.4. The P-wave velocity log and density log of well 14-35 from Hussar experiment located at east of Calgary as well as its reflectivity calculated from equation 1.13.

The reflectivity calculated from well log data is in depth and has very detailed information. This reflectivity needs to be correlated with real seismic data which is in time domain and has much less information (bandwidth). The correlation is the process of matching well depth to seismic times and requires the estimation of the seismic wavelet. Thus the synthetic data need to be created in time domain and to do this, the reflectivity needs to be converted into the time domain using 2-way time-depth table. By default, the time-depth table is automatically calculated from the sonic log velocities using the two way travel time equation for each layer

$$t_i = 2 * \sum_{j=1}^i \frac{d_j}{v_j}, \quad 3.1$$

where

$t_i$  = two way time to layer  $i$

$d_j$  = thickness of layer  $j$

$v_j$  = velocity of layer  $j$

and \* represents the conventional multiplication operator.

The time corresponding to a particular depth, depends on all the velocities above that depth including the first velocity to the surface. But as mentioned, because logs are not recorded near the surface, the shallow velocity is unknown and is often approximated by extrapolating the first measured velocity back to the surface (although this is a poor approximation because the velocity gets much slower in the very near surface). The time-depth table calculated from the sonic log in this method is never exactly correct because of various reasons such as

- The seismic data and log data may be different.
- The shallowest velocities are not logged.
- Errors in the sonic log velocities produce cumulative errors in the calculated travel-times.

There are many software packages which can apply a manual correction to the well time-depth curve to optimize the correlation between well depths and seismic times. Heather Lloyd introduced a Matlab based program designed to allow the user to choose knee points and then add or subtract slowness from the sonic log to produce the time-depth relationship (Lloyd, 2013). In this method a robust way to pick the match points and produce the time-depth curves is to match the Hilbert envelopes of the synthetic and real seismic traces.

Once the time-depth curve is created, the calculated reflectivity from P-wave velocity log and density log can be converted into the time domain. The time-depth curves for well 12-27, 14-27 and 14-35 have been illustrated in Figure 3.5, Figure 3.6 and Figure 3.7 respectively.

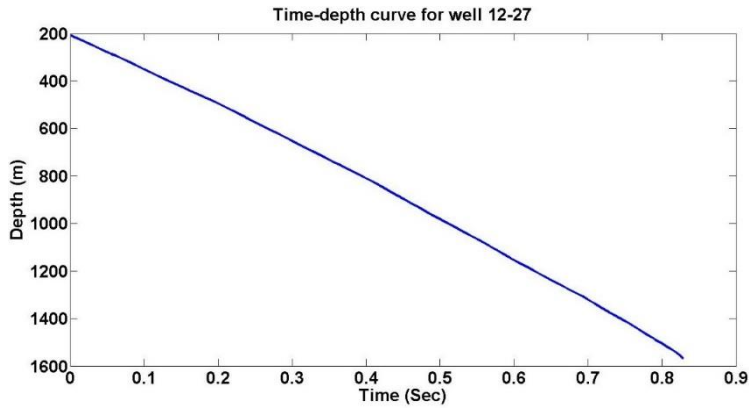


Figure 3.5. The computed time-depth curve for well 12-27. The association of  $t=0$  with  $z=200$  (the first logged depth) means that no overburden model is included.

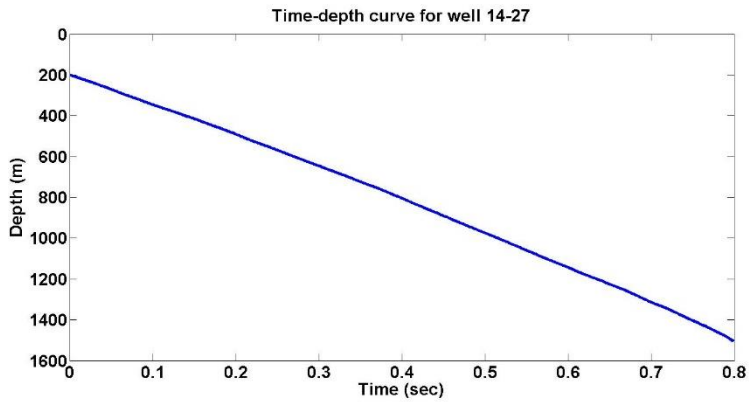


Figure 3.6. The computed time-depth curve for well 14-27. The association of  $t=0$  with  $z=200$  (the first logged depth) means that no overburden model is included.

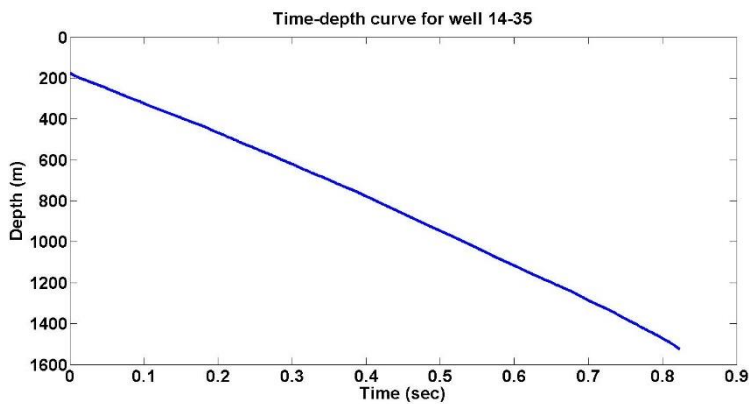


Figure 3.7. The computed time-depth curve for well 14-35. The association of  $t=0$  with  $z=178$  (the first logged depth) means that no overburden model is included.

The reflectivity function in time for each wells are illustrated in figures 3.8, 3.9 and 3.10 in both time domain and frequency domain which are converted from depth coordinate based on calculated time-depth curves. This reflectivity has been converted to time at a time-sample interval of 2 milliseconds. This is about twenty times larger than the average time between depth samples in the well log so an antialias filter is required to reject frequencies above 250 Hz. This filter causes the roll off in high frequencies in Figure 1.12 that begins around 130 Hz.

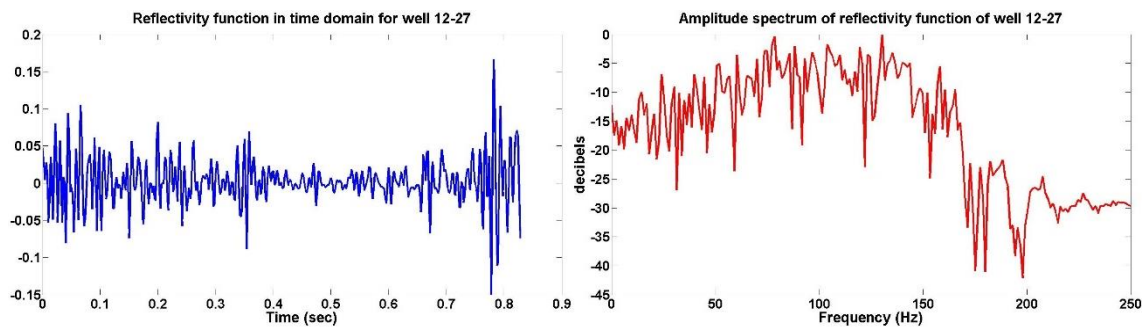


Figure 3.8. The converted reflectivity of well 12-27 from depth domain into the time domain using time-depth curve are illustrated in both time domain (left) and frequency domain (right). The decrease in amplitude in the frequency domain above 130 Hz is due to antialias filtering.

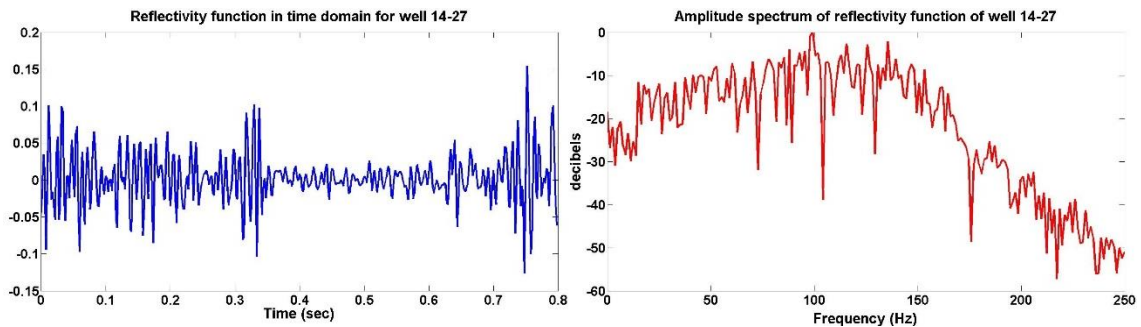


Figure 3.9. The converted reflectivity of well 14-27 from depth domain into the time domain using time-depth curve are illustrated in both time domain (left) and frequency domain (right). The decrease in amplitude in the frequency domain above 130 Hz is due to antialias filtering.

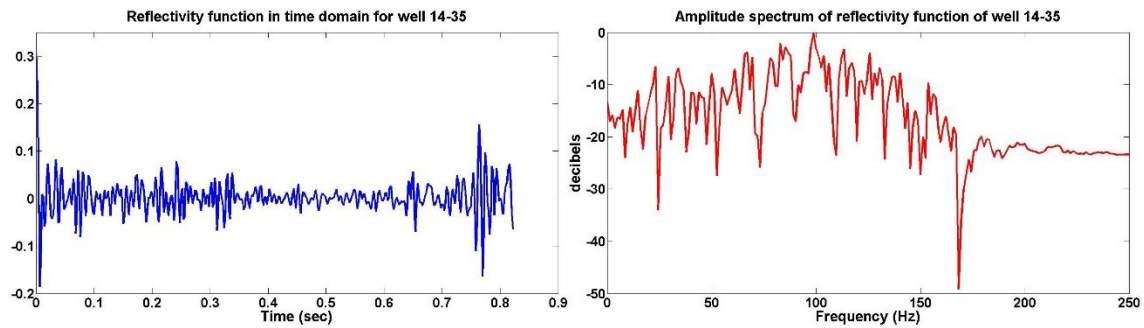


Figure 3.10. The converted reflectivity of well 14-35 from depth domain into the time domain using time-depth curve are illustrated in both time domain (left) and frequency domain (right). The decrease in amplitude in the frequency domain above 130 Hz is due to antialias filtering.

Comparing the amplitude spectrum of all these reflectivity functions with the amplitude spectrum of pseudo random reflectivity which was mentioned in the last chapter shows a significant difference on their amplitude spectrum. The other way to see the difference, calculating the autocorrelation of real and pseudo random reflectivities (figure 3.11).

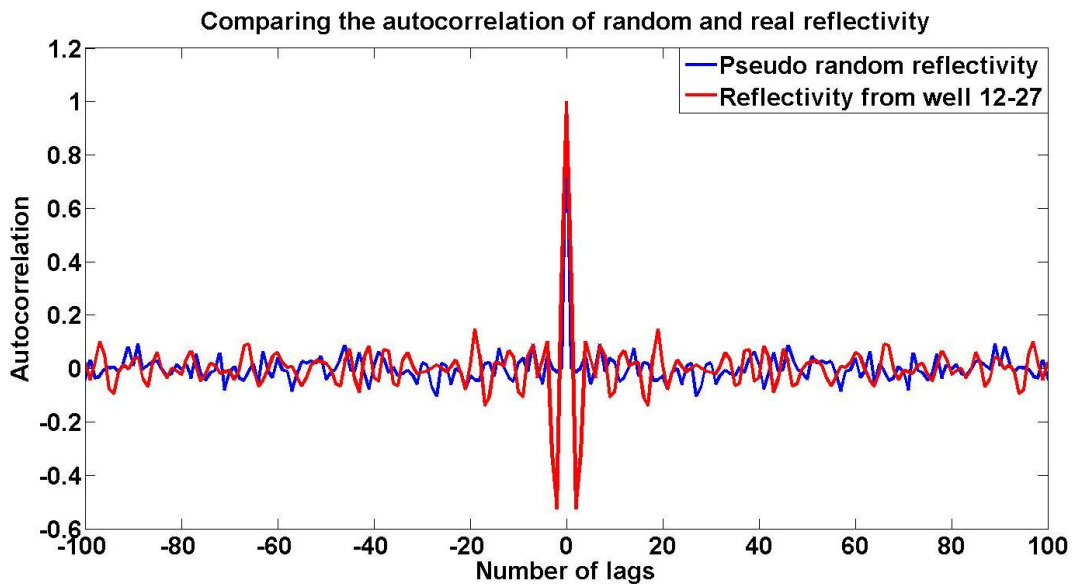


Figure 3.11. The autocorrelation of pseudo random reflectivity and the reflectivity from well 12-27. The large negative value at lag=2 indicates the non-whiteness property of real reflectivity.

The autocorrelation values at lag 2 indicate large negative values. The negative values at small lags are characteristic of the autocorrelation function of reflection sequences generated from well logs (O’Doherty and Ansety, 1971) which implies the non-whiteness spectrum (e.g. “color

spectrum”). Walden and Hosken (1985) demonstrated that the reflection coefficients from a wide variety of rock sequences around the world are colored. They showed that the reflection sequences are pseudo-white only above a corner frequency, below which their power spectrum falls away according to a power law  $f^\alpha$ , where  $\alpha$  is between 0.5 and 1.5 by analyzing 8 wells from a wide variety of geographical and geological sequences. The positive value of the exponent implies the low-cut behavior of reflection coefficient series.

Therefore, in the reality that the earth reflectivity does not have a white spectrum, the whiteness assumption of deconvolution algorithm is not met. To understand the effect of colored reflectivity on frequency dependent deconvolution results, the normal incident synthetic seismic trace created with “seismo” algorithm in Matlab CREWES toolbox. “Seismo” computes a 1-D seismic model from well log information. It uses the sonic log to build a time-depth curve, calculate the reflectivity function in the time domain using the computed time-depth curve and then convolving it with the given wavelet to create a synthetic seismic trace. The ideal seismic source would be a spike which has maximum amplitude at every frequency (broadband). Unfortunately, this cannot be realized in practice and the actual wavelet always contains a very limited range of frequencies. The other important concept is causality which means the concentration of energy of the wavelet should be near time zero (the initiation time). In this case it will be zero before time zero. The commonly chosen one would be minimum-phase wavelet. Here, the well 12-27’s log information have been used to compute the reflectivity function and the minimum-phase wavelet with 15 Hz dominant frequency and 2 milliseconds sample rate has been used. Figure 3.12 illustrates the resulted synthetic seismic trace modeled with seismo.

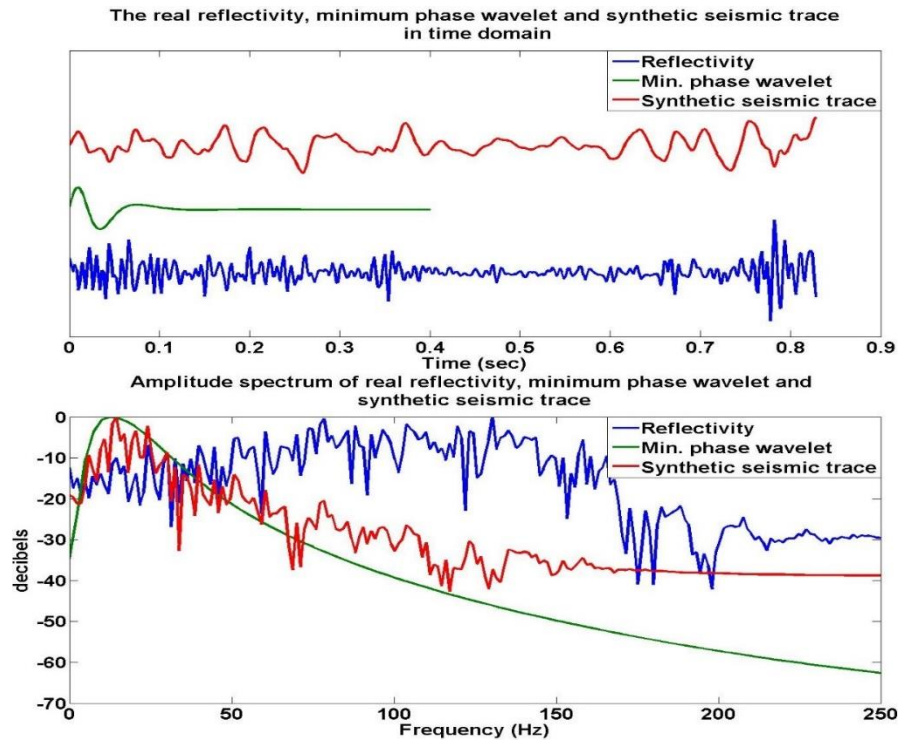


Figure 3.12 The normal incident synthetic seismic trace created from well 12-27 reflectivity and minimum-phase wavelet with 15Hz dominant frequency.

The seismic data illustrated in the Figure 3.12 is a simple example of recorded data in the field by geophones. Note that the synthetic data calculated here is based on a very simple model without considering any of the geometrical spreading effects, transmission losses, multiple reflections, noises and other non-stationary effects. By considering this simple model, to estimate the reflectivity from seismic trace, all we need to do is apply the deconvolution operator to the seismic data. To estimate the reflectivity, the deconvolution algorithm tries to remove the effect of wavelet from seismic trace. To do this, as discussed in chapter 2, the amplitude spectrum of wavelet can be estimated via smoothing of seismic spectrum and then the amplitude spectrum of deconvolution operator is proportional to inverse of amplitude spectrum of estimated wavelet (equation 2.9). Also, because the deconvolved trace should be minimum-phase its phase spectrum can be calculated via Hilbert transform of logarithm of its amplitude spectrum (Equation 2.12).

The result of applying frequency domain deconvolution with boxcar smoother on seismic data which gives us the estimated reflectivity illustrates on Figure 3.13. From this figure the amplitude spectrum of estimated reflectivity for frequencies between 5 Hz to 130 Hz is closely white. For frequencies higher than 130 Hz the rolling off of the spectrum is because of the anti-alias filter. Therefore any result from conventional deconvolution will not estimate the reflectivity properly and this is because, when the deconvolution operator with assumption of white spectrum reflectivity is applied to the seismic data which resulted from colored spectrum reflectivity, the color effects are removed.

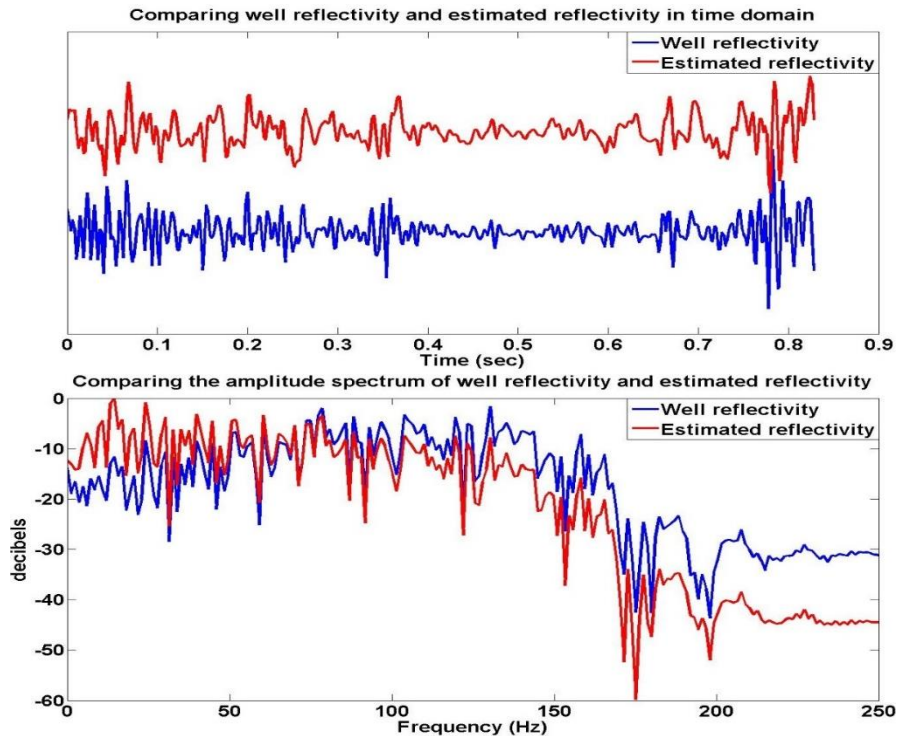


Figure 3.13. When the frequency domain deconvolution with the assumption of white spectrum reflectivity applying to the seismic data which resulted from colored spectrum reflectivity (well reflectivity), the deconvolved trace cannot does not include the color effects. (top) the well impedance and deconvolved trace in time domain and (bottom) their amplitude spectrum in frequency domain.

Equation 1.19 tells us to calculate the acoustic impedance the reflectivity function and the first layer's impedance are needed. For the real seismic data, as it has been seen, after

deconvolution the estimated reflectivity not only has white spectrum which mismatched with the spectrum of real reflectivity, also because of the bandlimited seismic data it is also so bandlimited. All these make the impedance inversion calculation becomes complex and challenge full. The recursion formula works perfectly for the broadband seismic data but when it has been used for bandlimited data it totally fails. The other method is using colored inversion method (Lancaster and Whitcombe, 2000). The colored inversion method is a simple and fast technique to invert the band-limited seismic data to relative impedance. This is done by generating a single operator to match the average seismic spectrum to the shape of the well log impedance spectrum. From their observation, the AI spectra can be written as power law such as

$$S_{AI} \propto f^{\alpha}, \quad 3.2$$

where  $f$  is frequency and the  $\alpha$  term is a negative constant number. The  $\alpha$  can be found for a field by curve-fitting to AI logs then the amplitude spectrum of the inversion operator is determined as being that which maps the seismic spectrum to a curve of form  $f^{\alpha}$ . Once the inversion operator has been derived it should be applied to the deconvolved trace to create the acoustic impedance. This can be done by convolving each seismic trace with the colored inversion operator (equation 3.3) as

$$I(t) = s(t) \bullet CI(t), \quad 3.3$$

where  $\bullet$  represents the convolution operator and  $I(t)$ ,  $s(t)$  and  $CI(t)$  are acoustic impedance, seismic trace and colored inversion operator in time domain respectively. Finally, the acoustic impedance from equation 3.3 needs to be scaled to match well impedance. Note that the colored inversion operator creates the bandlimited acoustic impedance. For example, Figure 3.14 shows the performance of this method in comparison with the recursion formula method for impedance

estimation of well 12-27 where 10Hz low cut-off frequency applied for the well impedance and recursion formula impedance.

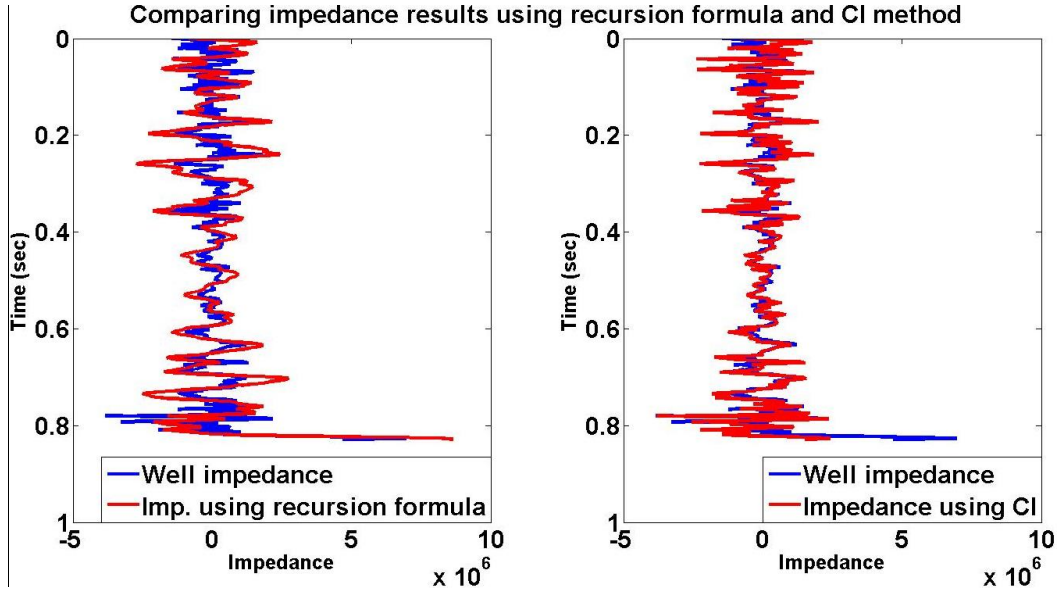


Figure 3.14. Comparing the acoustic impedance results using recursion formula and colored inversion method with well impedance. The 10Hz high pass filter has been applied to the well impedance and recursion formula impedance in this example.

Our observation of colored inversion operator shows this operator is proportional to -90 degree phase rotation of seismic data. This can be seen from the comparison of amplitude spectra of -90 degree phase rotated seismic data and colored inversion method's result (Figure 3.15). Notice that we would not expect a -90 degree phase rotation to show anything on the amplitude spectrum. Also in the next figure (Figure 3.16) both data balanced with the bandlimited well impedance (13Hz high pass filtered applied to the well impedance) to compare them with the bandlimited well impedance.

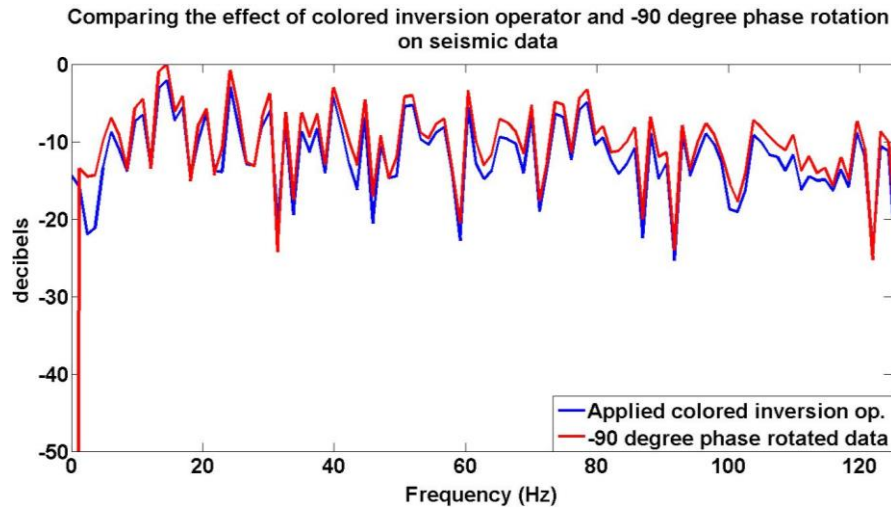


Figure 3.15. The amplitude spectrum of the seismic data one after applying colored inversion operator and the other after applying -90 degree phase rotation.

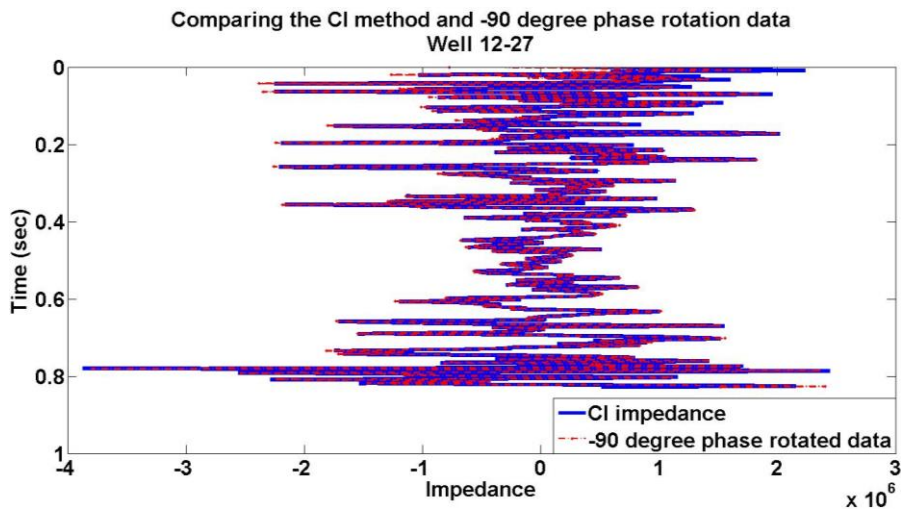


Figure 3.16. Comparing the colored inversion method and -90 degree phase rotation on seismic data in time domain.

### 3.2 Designing the color operator

The results in Figure 3.13 showed that the deconvolved real seismic data need color correction because of color properties of real reflectivity. This can be done by designing a suitable color operator to be applied after deconvolution. The objective of the color operator is to create a model that represents the color trend in the spectrum without reproducing the specific characteristics of reflectivity that must be preserved in the seismic; such as the reflections to be

interpreted. Thus, the operator should depend only on the observed spectral shape of the reflectivity. Also, this operator needs to correct the error of minimum-phase whitening deconvolution operator, therefore it must be minimum-phase. The desired color operator can be designed in many different ways. The main concept is to use real reflectivity which is available in well locations and its Fourier transformation in frequency domain. A method was introduced by Hunt et. al. (1993) based on autocorrelation function of well reflectivity and then the designed color operator can be applied into the deconvolved trace. The operator derivation can be done by multiplying the specific window to the reflectivity autocorrelation and that means in frequency domain it is equivalent to the smoothed power spectrum of reflectivity. Once the amplitude spectrum of the operator was found its phase spectrum can be calculated as a minimum-phase and the time transferred color operator can be applied to the deconvolved trace. For instance, here the Gaussian window has been used to derive the operator of each reflectivity in Hussar well locations. We call these operators the AutoCorrelation (AC) color operator. The AC color operators for all three well have been shown in figures 3.15, 3.16 and 3.17. Note, the phase spectrum can be calculated by Hilbert transform of the logarithm of the amplitude spectrum. The result of applying these color operators to the data will be shown later.

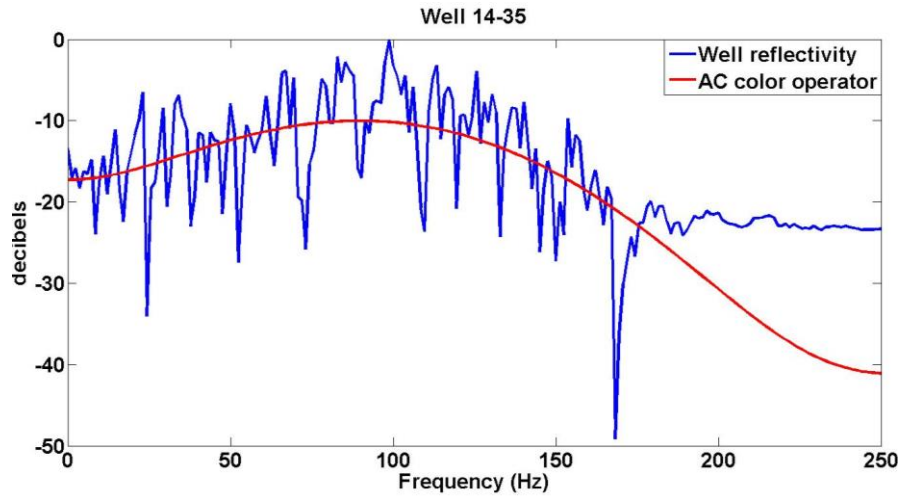


Figure 3.17. The calculated amplitude spectrum of AC color operator from multiplying Gaussian function with the autocorrelation of reflectivity of well 14-35 in frequency domain.

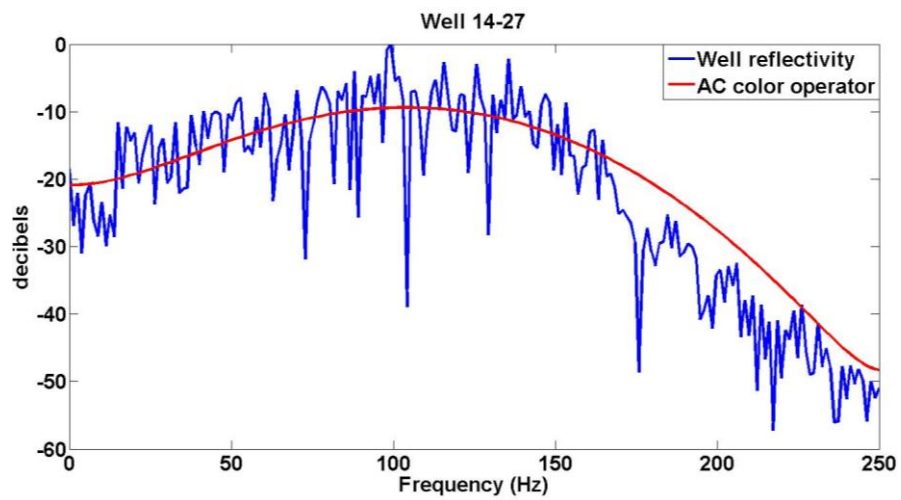


Figure 3.18. The calculated amplitude spectrum of AC color operator from multiplying Gaussian function with the autocorrelation of reflectivity of well 14-27 in frequency domain.

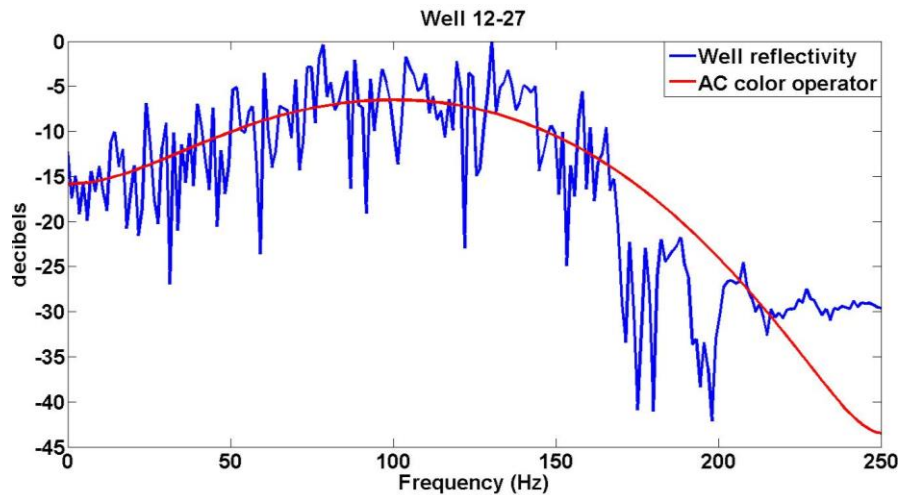


Figure 3.19. The calculated amplitude spectrum of AC color operator from multiplying Gaussian function with the autocorrelation of reflectivity of well 12-27 in frequency domain.

Using the same idea but different methods, other types of color operator can be designed. In this case, to design the color operator first its amplitude spectrum needs to be extracted by fitting appropriate curve on the amplitude spectrum of reflectivity and once its amplitude spectrum calculated, its phase spectrum can be computed using Equation 2.12 (minimum-phase spectrum). It needs to be noticed that from examination of Figure 3.13 we are not interested in the spectral shape of the reflectivity for frequencies higher than 130Hz since these frequencies are shaped by an anti-alias filter. The real reflectivity from the well has a very high sample rate which in time is roughly around every 0.1 milliseconds. However the sample rate of seismogram is usually around one or two milliseconds and therefore the well log data must be downsampled. Whenever a signal goes from more samples to fewer samples, an anti-alias filter is required. Thus the creation of a synthetic seismogram from well log requires an anti-alias filter. A typical anti-alias filter has an amplitude spectrum which begins to roll off at 50% to 60% of Nyquist frequency and reaches very large attenuation at Nyquist frequency. That is why the amplitude spectrum of reflectivity starts to decay after 130Hz in Figure 3.13. For example the Hussar well 12-27 reflectivity with three

different sample rates, 0.002; 0.001 and 0.0005, in time and frequency domain are shown in Figure 3.20. Using higher sample rates shifts the anti-alias filter effect to higher frequencies, revealing an essentially flat spectrum.

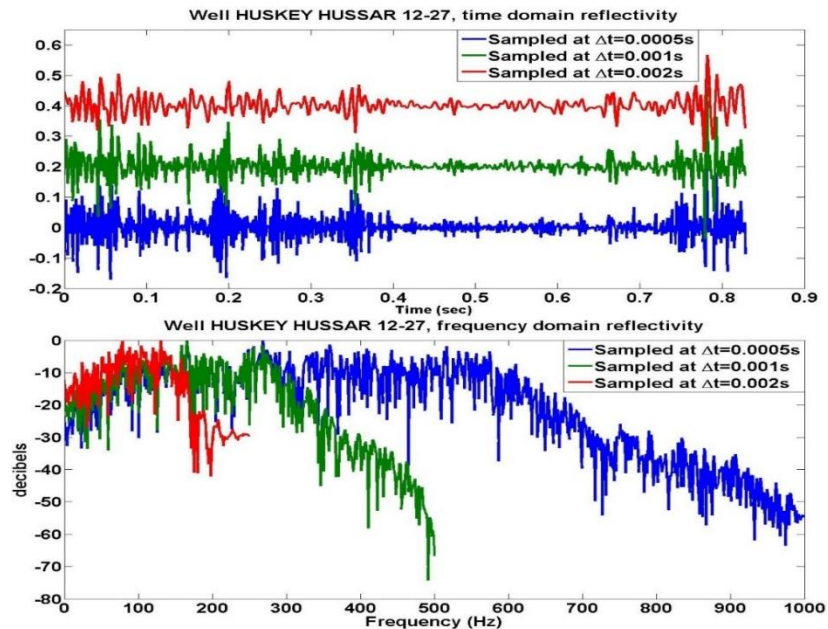


Figure 3.20 A comparison of well log reflectivity for Husky Hussar well in the time and frequency domains. The frequency domain views show clearly the effect of the anti-alias filter which begins its roll off at  $\frac{1}{2}$  of the Nyquist frequency. The low frequency roll off is essentially independent of sample rate and is similar in all sample rates. This low frequency roll off is what is modelled by our color operators.

We will investigate several curve-fitting models for spectral color like the arctan function or sigmoid function and these color operators should be applied to the seismic data right after deconvolution process to shape the whitened result from deconvolution into the reflectivity's colored spectrum. Once this is done the trace is said to be colored and further processing including inversion can proceed. Again, once the amplitude spectrum of a color operator is calculated its phase can be calculated by Hilbert transform of the logarithm of the amplitude spectrum. We will design a color operator that has a very smooth spectrum in the hope that it will have wide applicability.

Considering the reflectivity of Hussar well 12-27 (Figure 3.8), one possible function to fit on reflectivity's amplitude spectrum based on this figure is the arctan function. Mathematically, for fitting arctan function into the reflectivity function we can write

$$a + b \arctan(f) = R(f) \quad 3.4$$

where  $a$  and  $b$  are constants and should be determined and  $R(f)$  is the amplitude spectrum of reflectivity function in term of frequency. In matrix representation, equation 3.4 can be written as

$$[1 \quad \arctan(f)]_{n \times 2} \begin{bmatrix} a \\ b \end{bmatrix}_{2 \times 1} = A \begin{bmatrix} a \\ b \end{bmatrix} = R_{n \times 1} \quad 3.5$$

where 1 in the left hand side is  $n \times 1$  matrix and  $n$  is the length of frequency ( $f$ ). Note that  $A$  is just substituted with  $[1 \quad \arctan(f)]_{n \times 2}$  in this equation. To find  $a$  and  $b$  in equation 3.5, both sides should be multiply by inverse of from the left

$$\begin{bmatrix} a \\ b \end{bmatrix}_{2 \times 1} = (A^T A)^{-1} A^T R \quad 3.6$$

By finding  $a$  and  $b$  the appropriate arctan function related to the well reflectivity can be determined. We call this color operator the arctan color operator. For example for the Hussar well 12-27  $a$  and  $b$  become 0.1623 and 0.9854 respectively. In the Figure 3.21 the color operator and its amplitude spectrum in frequency domain are shown.

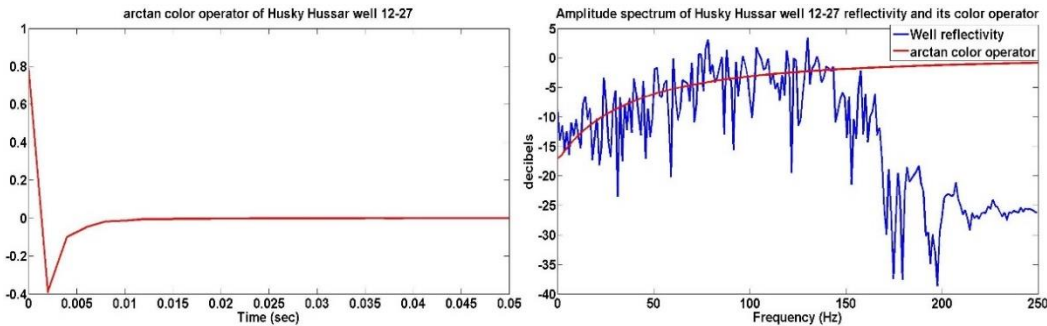


Figure 3.21 The minimum-phase arctan color operator of Husky Hussar well 12-27 in time domain (left) and its amplitude spectrum in frequency domain (right)

Examination of the frequencies below than 10Hz shows this part has a locally flattened shape which is not well modelled by the arctan function. Another possible model for color operator's amplitude spectrum including the horizontal part at low frequencies is fitting a sigmoidal function into the earth reflectivity amplitude spectrum. The mathematical form of the sigmoid function is

$$S(f) = \frac{a+bs}{\sqrt{1+s^2}}; s = \frac{f - f_0}{f_0}, \quad 3.7$$

where again  $a$  and  $b$  are the constants and the frequency  $f_0$  is the inflection point of the sigmoid function. Given  $f_0$ , finding  $a$  and  $b$  is accomplished by ordinary least squares. All three parameters are found by scanning over the range of likely frequencies for  $f_0$ , in increments of 0.5 Hz. The scan for  $f_0$  is done from 10 Hz to half Nyquist and the minimum norm found in this scan determines  $f_0$ . For instance, the sigmoidal color operator has been calculated for Huskar well 12-27 with  $a = -17.3914$ ,  $b = 7.6129$  and  $f_0 = 34$ Hz. This color operator and its amplitude spectrum are illustrated in Figure 3.22. As can be seen from this figure, the amplitude spectrum of sigmoidal color operator can fit much better on the amplitude spectrum of reflectivity in frequencies below than 10Hz.

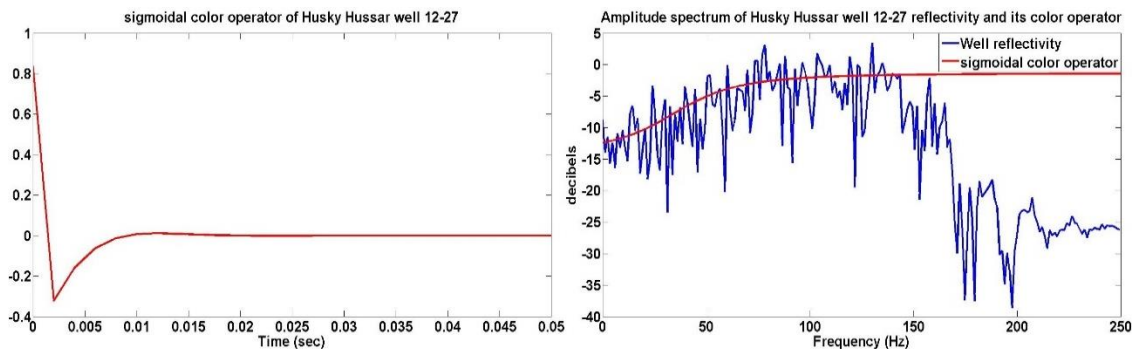


Figure 3.22. The sigmoidal color operator of Husky Hussar well 12-27 in time domain (left) and its amplitude spectrum in frequency domain (right)

The same procedure can be done to derive the sigmoidal color operator for Hussar wells 14-27 and 14-35. The calculated values for  $a$ ,  $b$  and  $f_0$  for well 14-27 are -15.7434, 7.8106 and 39Hz and for well 14-35 are -15.8890, 6.8429 and 24Hz respectively. Figure 3.23 and Figure 3.24 compare the arctan and sigmoidal color operators for all three wells of Husky Hussar project in both time and frequency domain.

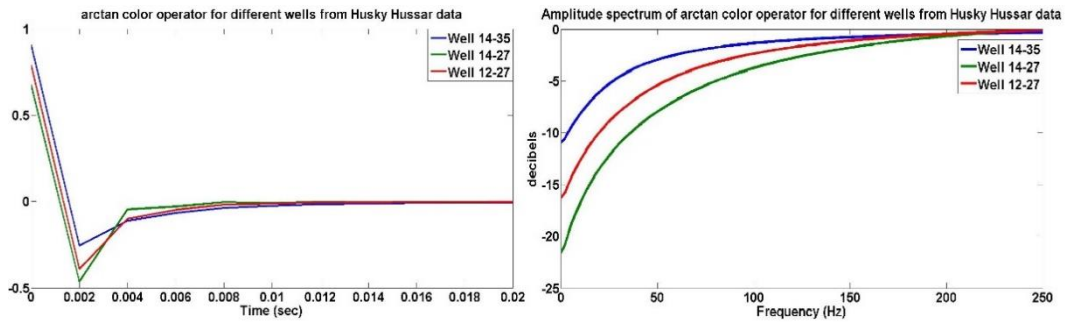


Figure 3.23. The arctan color operator has been designed for three Hussar well. Their comparison shows the differences are minor along the studied area.

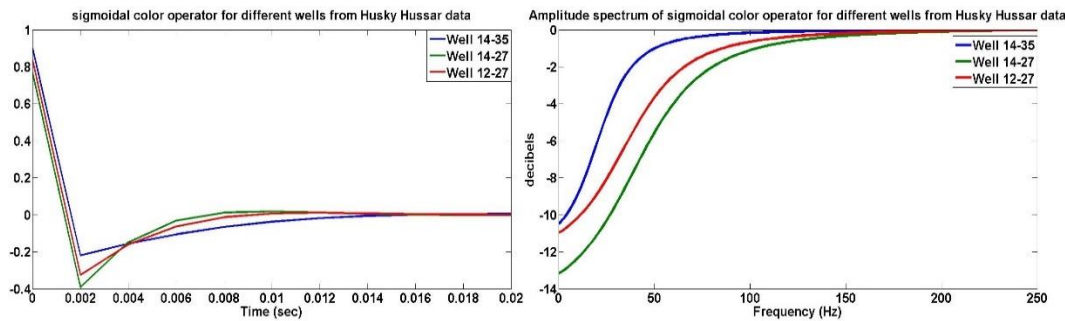


Figure 3.24. The sigmoidal color operator has been designed for three Hussar well. Their comparison shows the differences are minor along the studied area.

Any of these color operators can be applied to the data right after deconvolution process and as it will be shown later these color operator can improve the color effects of reflectivity significantly.

### 3.3 Deconvolving the synthetic seismic data

To investigate the performance of color operator and its ability to correct the color effects of deconvolved data, the normal incident synthetic seismic data created from the reflectivities of

each Husky Hussar wells data. Then the both color operators of each reflectivities applied to the deconvolved data right after deconvolution process.

The reflectivity functions of each well which have been computed in time and showed in the Figure 3.8, Figure 3.9 and Figure 3.10 are convolved with a minimum-phase wavelet with 15 Hz dominant frequency and 2 milliseconds sample rates (Figure 3.25) and the results are the synthetic seismic traces related to each well (Figure 3.26). This means, in case of the source and receiver are located at the well location, the recorded seismic trace via receiver will be the same that calculated from convolution. Note that the created seismic data has been calculated based on a very simple model without considering any of the geometrical spreading effects, transmission losses, an-elastic absorption, multiple reflections and noises.

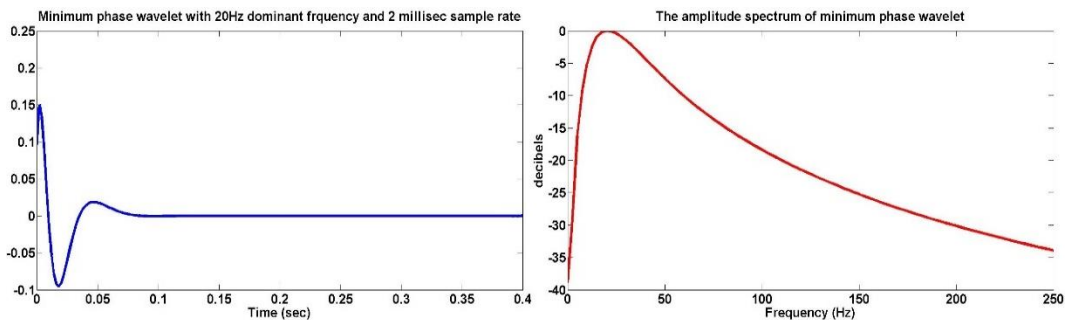


Figure 3.25 The minimum-phase wavelet with 15Hz dominant frequency and 2 milliseconds sample rate. In the left this wavelet is shown in time domain and the right is the amplitude spectrum of the same wavelet in decibels.

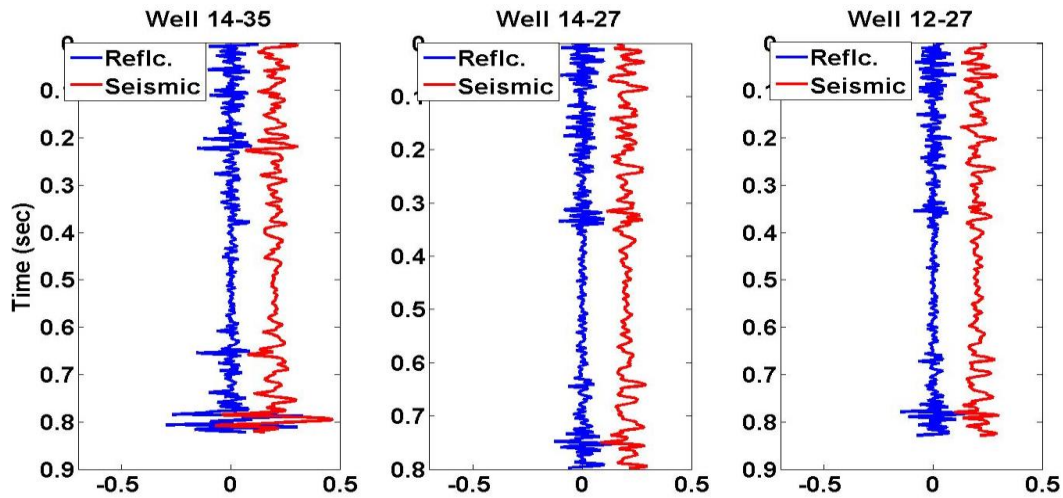


Figure 3.26 The reflectivity functions related to each Husky Hussar well and their computed normal incident synthetic seismic trace.

In the previous chapter, three different algorithms have been defined for frequency domain deconvolution. These three algorithms were based on different smoother types for deconvolution algorithm and they have been classified as Boxcar Smoother (BS), Constant Gaussian Smoother (CGS) and Frequency Dependent Gaussian Smoother (FDGS) and their results after applying to the pseudo random reflectivity data illustrated in chapter two. The results showed significant improvement especially in the impedance calculation when the FDGS has been used as a smoother in deconvolution algorithm. Here, first of all, it will be tried to find the best deconvolution method for synthetic data resulted from the real reflectivity and then the effect of each color operator methods will be investigated. To do this, frequency domain deconvolution with three different smoother types have been applied to each synthetic data from Hussar wells and the results are shown in Figure 3.27, Figure 3.28 and Figure 3.29 for well 14-35, 14-27 and 12-27 respectively.

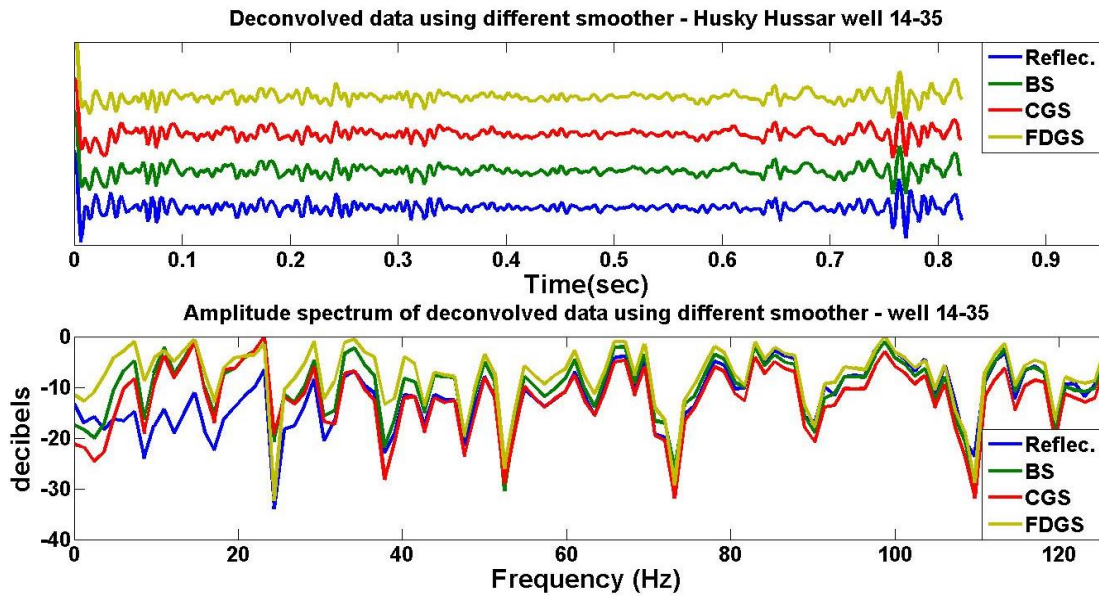


Figure 3.27 Reflectivity estimation of Husky Hussar well 14-35 using different deconvolution algorithm. BS, CGS and FDGS represent boxcar smoother, constant Gaussian smoother and frequency dependent Gaussian smoother.

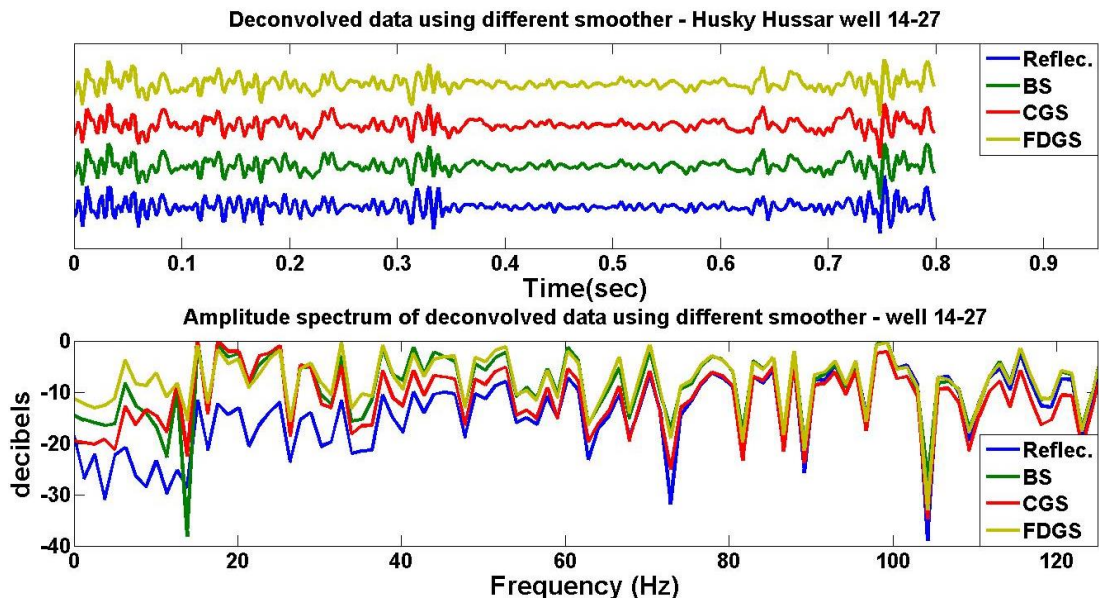


Figure 3.28 Reflectivity estimation of Husky Hussar well 14-27 using different deconvolution algorithm. BS, CGS and FDGS represent boxcar smoother, constant Gaussian smoother and frequency dependent Gaussian smoother.

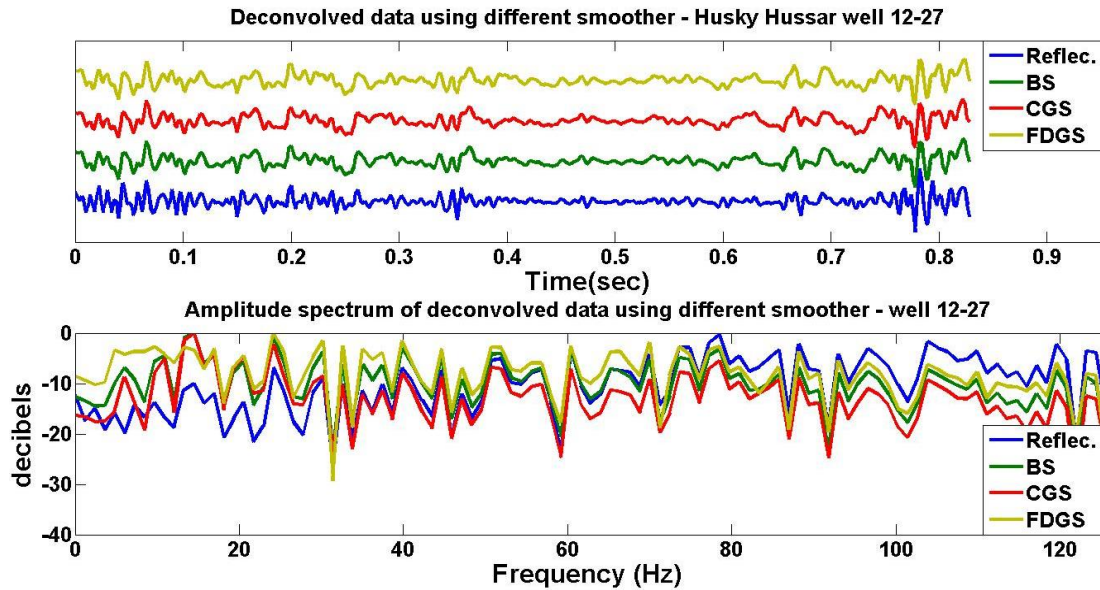


Figure 3.29 Reflectivity estimation of Husky Hussar well 12-27 using different deconvolution algorithm. BS, CGS and FDGS represent boxcar smoother, constant Gaussian smoother and frequency dependent Gaussian smoother.

In each case the appropriate smoother length have been chosen from the same method which we used in the chapter two. Table 3.1 is showing the optimum smoother length in frequency for both boxcar and Gaussian smoother at three Hussar wells location.

	Boxcar smoother length (Hz)	Gaussian smoother length (Hz)
Well 14-35	43	18
Well 14-27	63	34
Well 12-27	38	23

Table 3.1 The optimum boxcar and Gaussian smoother length for each dataset. The results show the Gaussian smoother length is approximately half of the boxcar smoother length.

To investigate which smoother type can be optimum choice, the error function between deconvolved trace calculated from each smoother type and its appropriate well reflectivity can be computed. Also the maximum correlation calculation between these two parameters can be helpful. Figure 3.30 displays the calculated errors for each well using different smoothers in

deconvolution algorithm both in time and frequency domain and Table 3.2 shows the calculated maximum correlation deconvolved trace calculated from each smoother type and well reflectivity.

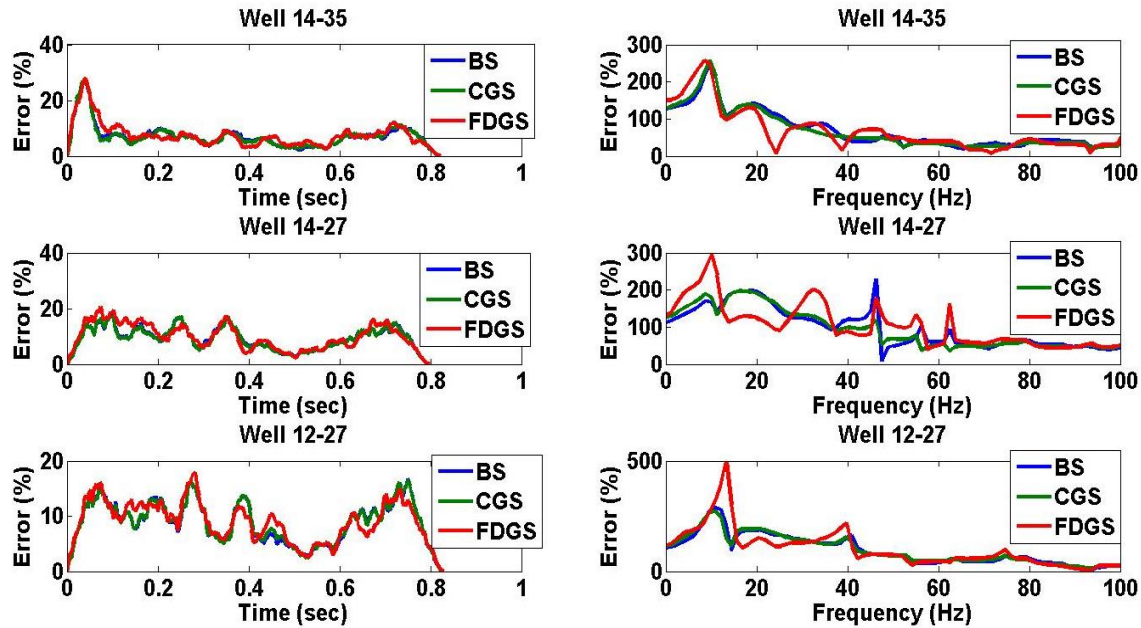


Figure 3.30 The error function between well reflectivity and deconvolved trace calculated for each well with three different smoother type in both time and frequency domain.

	Well 14-35	Well 14-27	Well 12-27
BS	0.9226	0.8754	0.8770
CGS	0.9227	0.8756	0.8769
FDGS	0.9000	0.8464	0.8667

Table 3.2. Calculated maximum correlation between deconvolved trace and well reflectivity of Hussar well. The results show higher correlation value when we use boxcar smoother in deconvolution algorithm in compare with the other smoother types.

From comparing the both maximum correlation results and calculated errors it is possible to decide which smoother method can be a good option for frequency domain deconvolution. In the Table 3.2 the maximum correlation values in three wells show that using frequency dependent Gaussian smoother in deconvolution algorithm leads to small correlation value compared to the other smoothers. This result also can be proven from computed errors in frequency domain

observation which shows a significant error differences between using FDGS and two other smoothers in frequencies lower than 15 Hz. Note that in time domain it is hard to decide about which deconvolution methods work better because the error variation in time domain is too much for all three wells.

However, as it was seen in the previous chapter, this result was completely different when the seismic data was created with white reflectivity. This can be clarified if the smoothed power of seismic can be compared with the one which came from exact wavelet (The main attempt of deconvolution operator is estimating the wavelet as precise as possible). Figure 3.31 to Figure 3.36 illustrate these comparisons for both pseudo random and well reflectivity data with three different smoother types respectively.

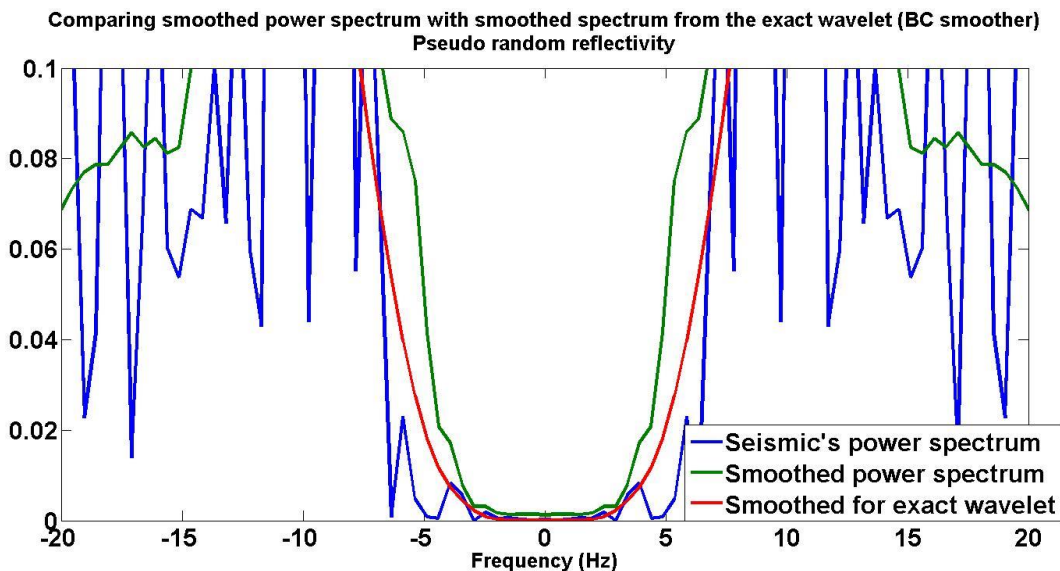


Figure 3.31. Comparing the smooth of seismic's power with the case if the actual wavelet has been as a smooth of seismic's power using BC smoother type for pseudo random reflectivity.

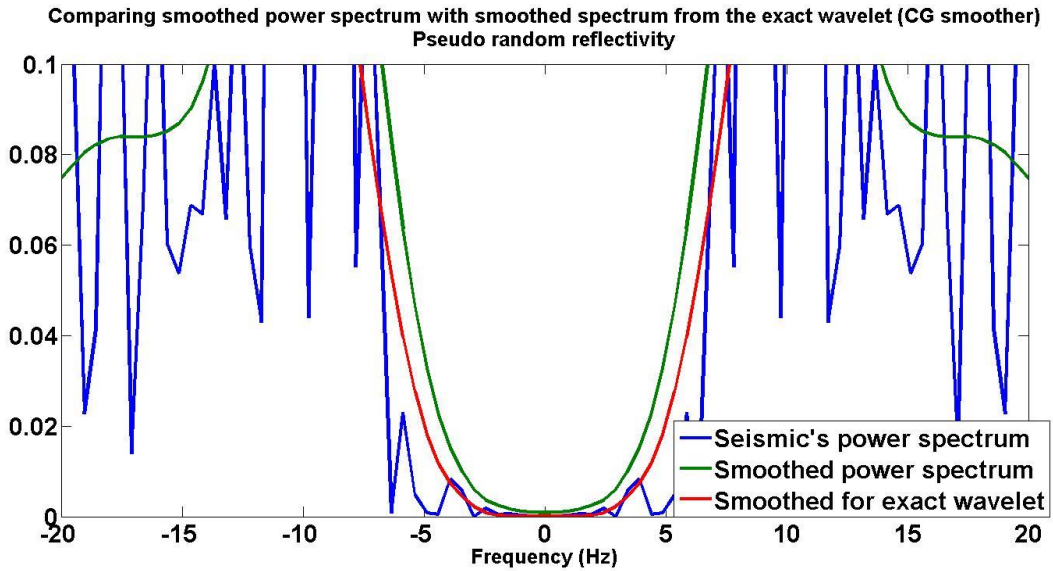


Figure 3.32. Comparing the smooth of seismic's power with the case if the actual wavelet has been as a smooth of seismic's power using CG smoother type for pseudo random reflectivity.

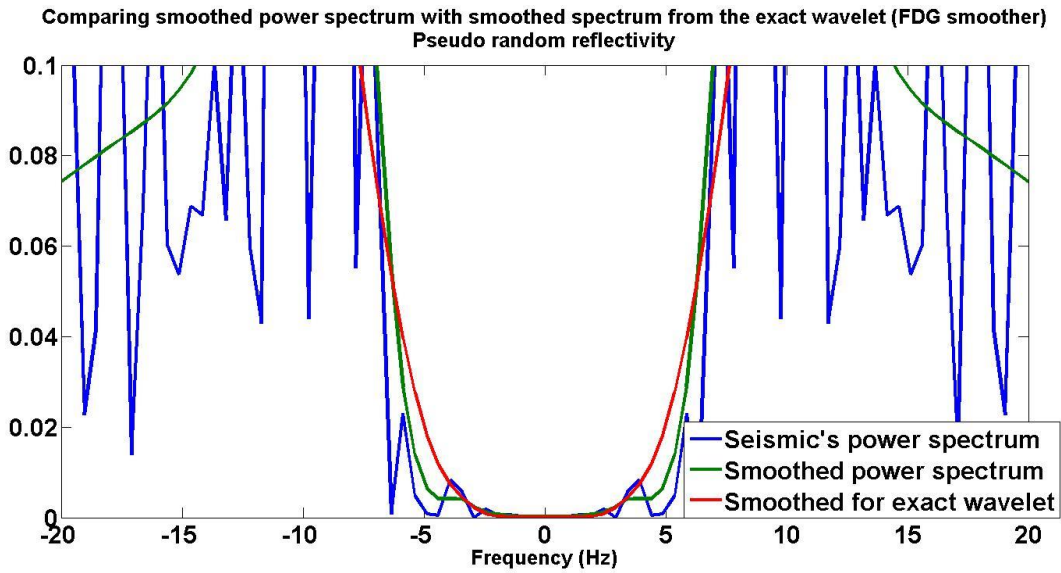


Figure 3.33. Comparing the smooth of seismic's power with the case if the actual wavelet has been as a smooth of seismic's power using FDG smoother type for pseudo random reflectivity.

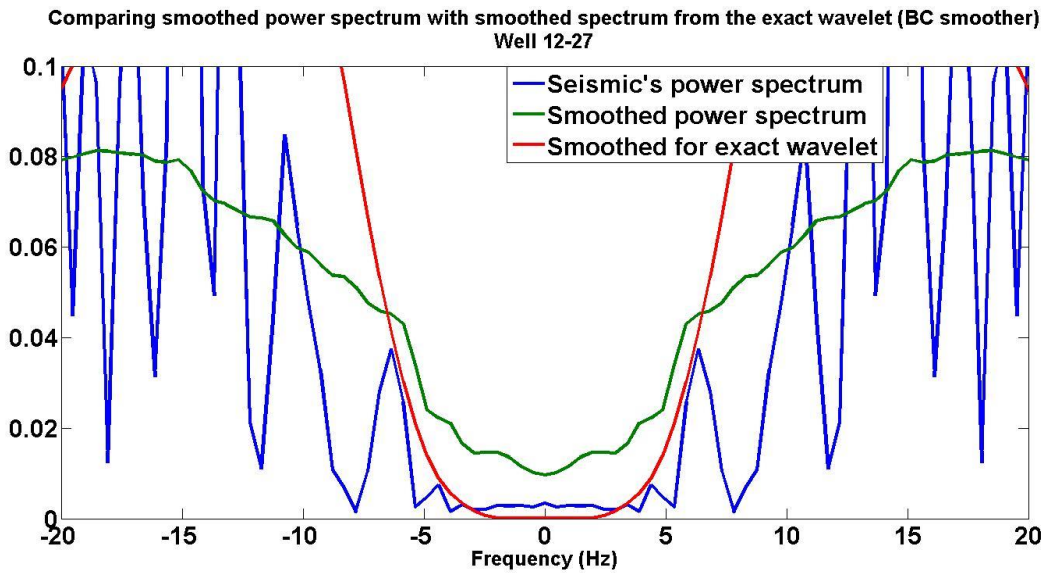


Figure 3.34. Comparing the smooth of seismic's power with the case if the actual wavelet has been as a smooth of seismic's power using BC smoother type for well reflectivity.

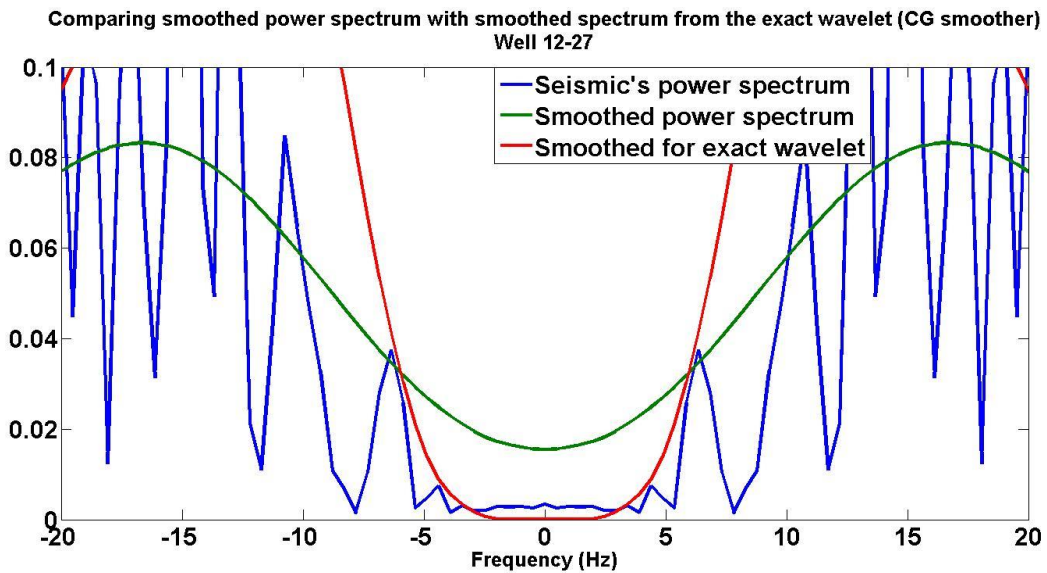


Figure 3.35. Comparing the smooth of seismic's power with the case if the actual wavelet has been as a smooth of seismic's power using CG smoother type for well reflectivity.

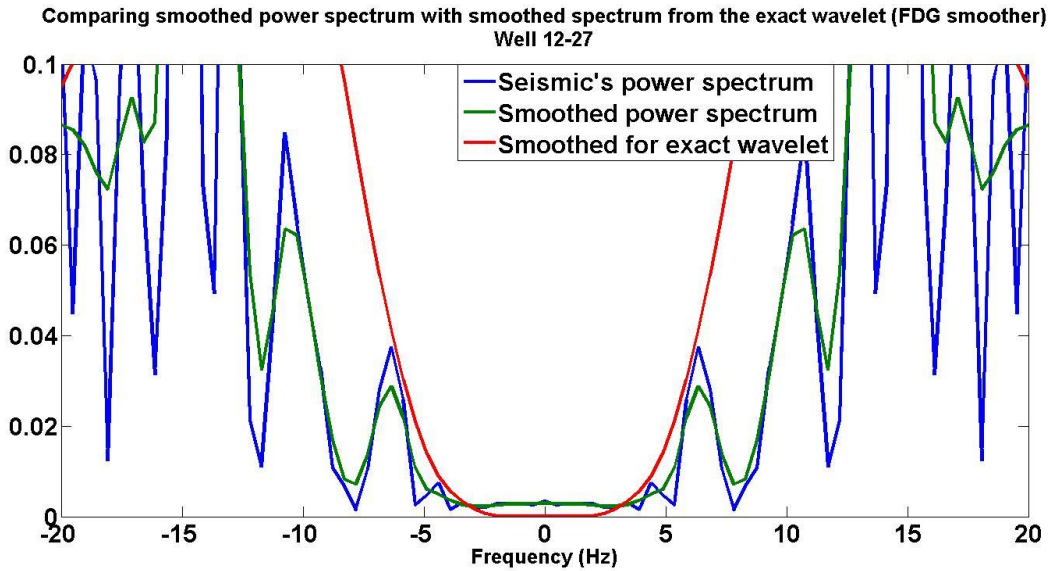


Figure 3.36. Comparing the smooth of seismic's power with the case if the actual wavelet has been as a smooth of seismic's power using FDG smoother type for well reflectivity.

Comparing these figures and also the result of maximum correlations (Table 2.1 and Table 3.2) and errors can clearly demonstrate that when the smoothed power spectrum shape is closer to the exact wavelet shape this causes better wavelet estimation and then better reflectivity estimation. On the other hand, the high value of maximum correlation in pseudo random reflectivity case when deconvolved with FDGS deconvolution algorithm resulted from the similarity of smoothed power spectrum and smoothed exact wavelet in this case. The other fact can be seen from Figure 3.31 to Figure 3.36 is about very low frequency part (Frequencies between 0 to 5Hz). At this area the power spectrum of seismic data belonged to the pseudo random reflectivity have nearly zero amplitude and that is the reason when it has been trying to smooth this part, the smoothed spectrum became so close to the exact wavelet curve. However, in the case of real reflectivity, at this region the power spectrum has the value higher than zero which causes its smoothed spectrum to differ significantly with the exact wavelet curve. This is a very important result that shows the reason that the frequency domain deconvolution is not able to estimate the

reflectivity precisely especially in the low frequencies and that is not only because of the smoothening process. The colored spectrum property of the real reflectivity in the low frequencies causes any method of smoothening to become unsuccessful in this matter.

The recent comparison for the deconvolution of well synthetic seismic trace demonstrates that using one of the boxcar or constant Gaussian smoother as an optimum smoother type for deconvolution algorithm might be good choice rather than using frequency dependent Gaussian smoother. Here, the boxcar smoother for all three well data has been selected. As it has been mentioned before, once the seismic data are deconvolved, the color operator can be apply to the deconvolved data to correct the color effect of reflectivity. For each dataset three different minimum-phase color operator which have been derive previously will be applied and the results on both time and frequency domain will be shown.

### **3.4 Effect of color operator on deconvolved data**

As mentioned previously, the reason to use the color operator is to recover the color effect of deconvolved data without reproducing the specific characteristics of reflectivity that must be preserved in seismic. At the beginning of this chapter two different color operators have been created via curve fitting technique to the spectrum of well reflectivity and these two color operators were shown on Figure 3.23 and Figure 3.24 for all Hussar wells. The results of using different smoother in the frequency domain deconvolution also showed that using either boxcar or constant Gaussian smoother gave better results in frequency domain in comparison with frequency dependent Gaussian smoother algorithm. In figures 3.25, 3.26 and 3.27 the result of deconvolved traces of well 14-35, 14-27 and 12-27 are shown respectively using the boxcar smoother algorithm.

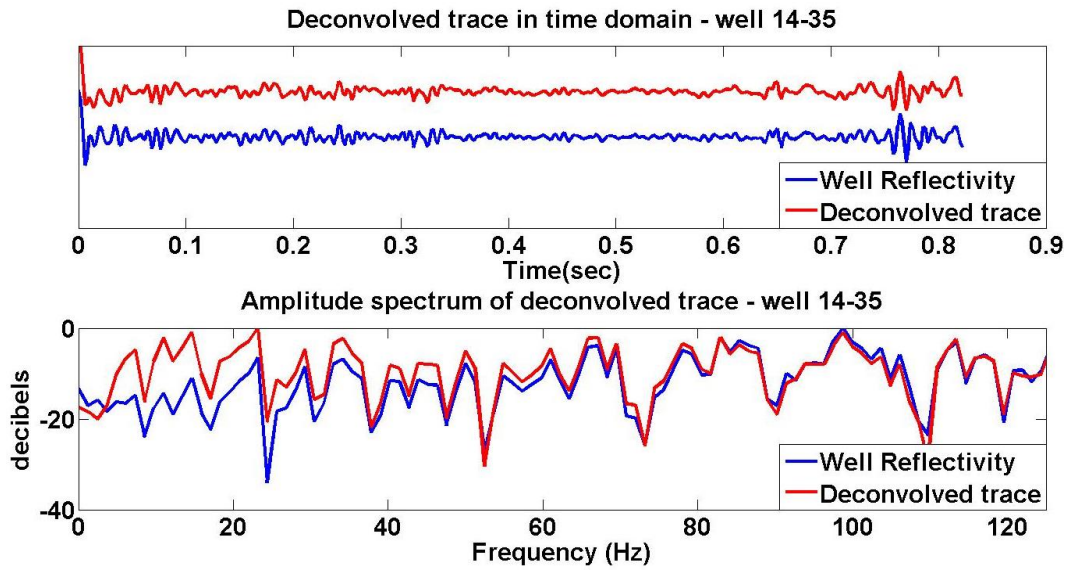


Figure 3.37. The deconvolved trace of synthetic trace created from well 14-35 data using boxcar smoother algorithm.

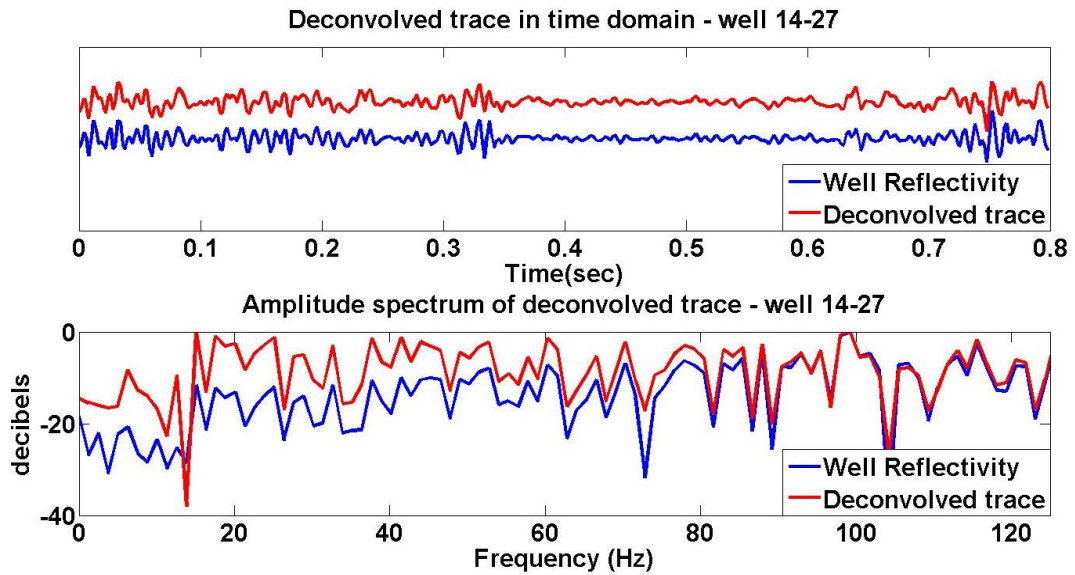


Figure 3.38. The deconvolved trace of synthetic trace created from well 14-27 data using boxcar smoother algorithm.

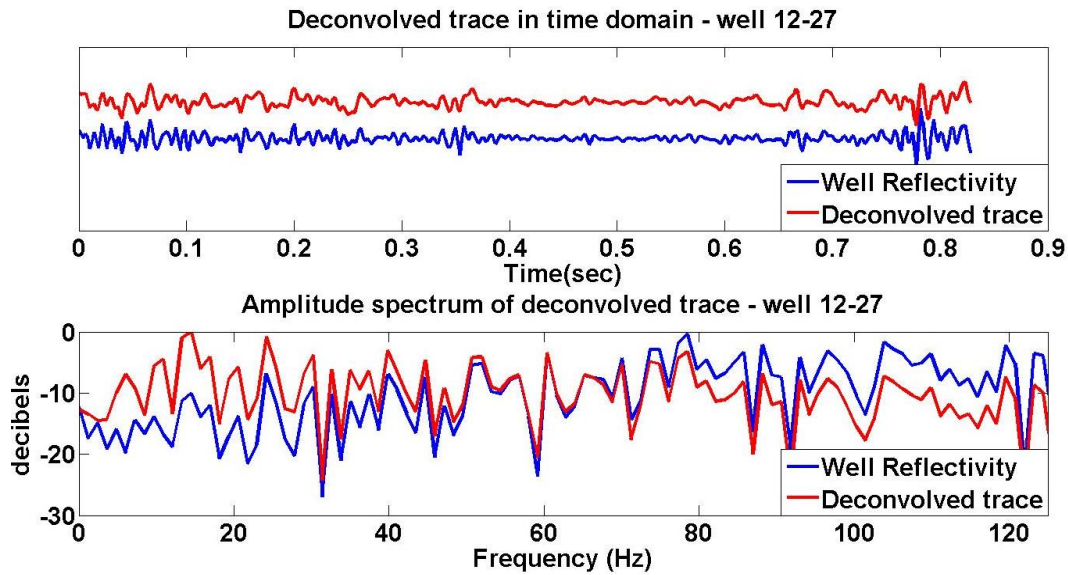


Figure 3.39. The deconvolved trace of synthetic trace created from well 12-27 data using boxcar smoother algorithm.

As it was expected, in all three cases when the frequency domain deconvolution with the assumption of white reflectivity is applied to the seismic data, the color properties of the data are missing and this causes incorrect estimation of low frequencies of the estimated reflectivity. In all three cases, as it can be seen, the spectrum of real reflectivity rolls off from frequencies around 60 Hz. While, the spectrum of estimated reflectivity is trying to remain flat. The color operator was designed to correct these white effects of deconvolved data and as it was mentioned, it should be applied to the deconvolved data right after deconvolution process. To do this, the deconvolved trace needs to be convolved with color operator which was designed for each Hussar well in section 3.2.

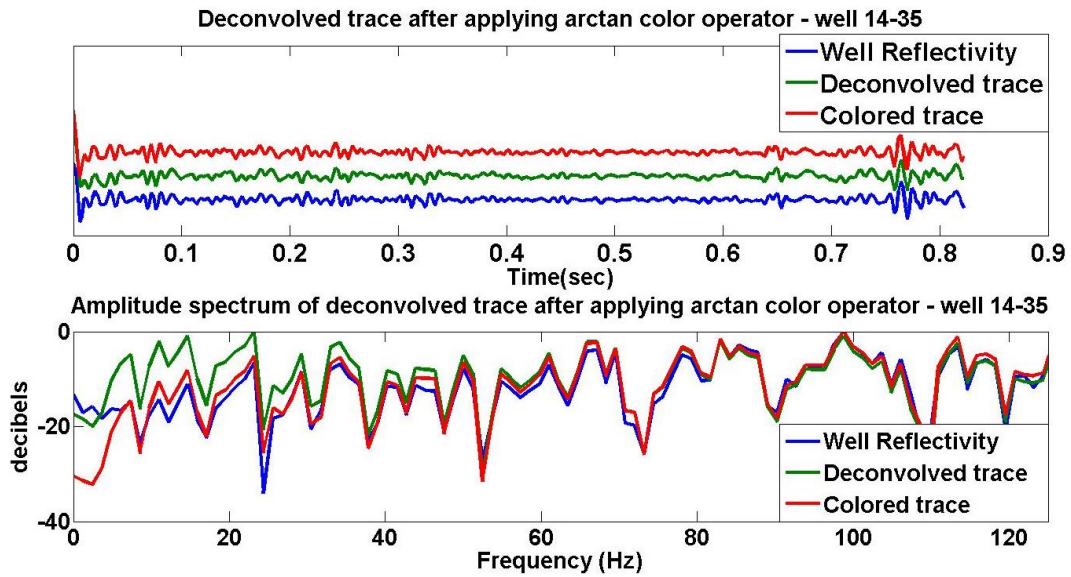


Figure 3.40. The result of applying arctan color operator on the deconvolved trace from well 14-35 in the time and frequency domain and comparing it with the deconvolved trace without applying color operator.

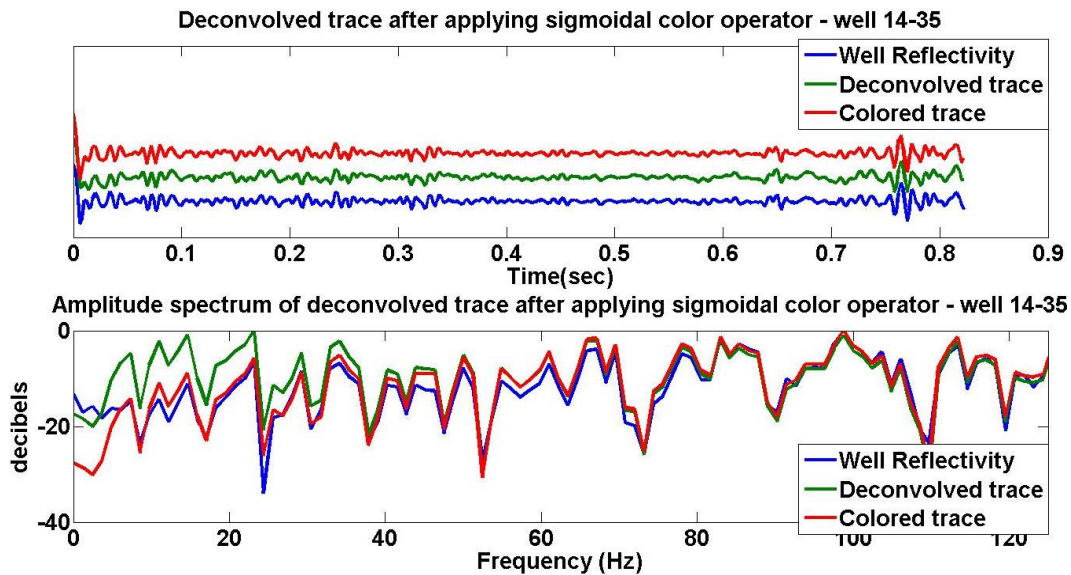


Figure 3.41. The result of applying sigmoidal color operator on the deconvolved trace from well 14-35 in the time and frequency domain and comparing it with the deconvolved trace without applying color operator.

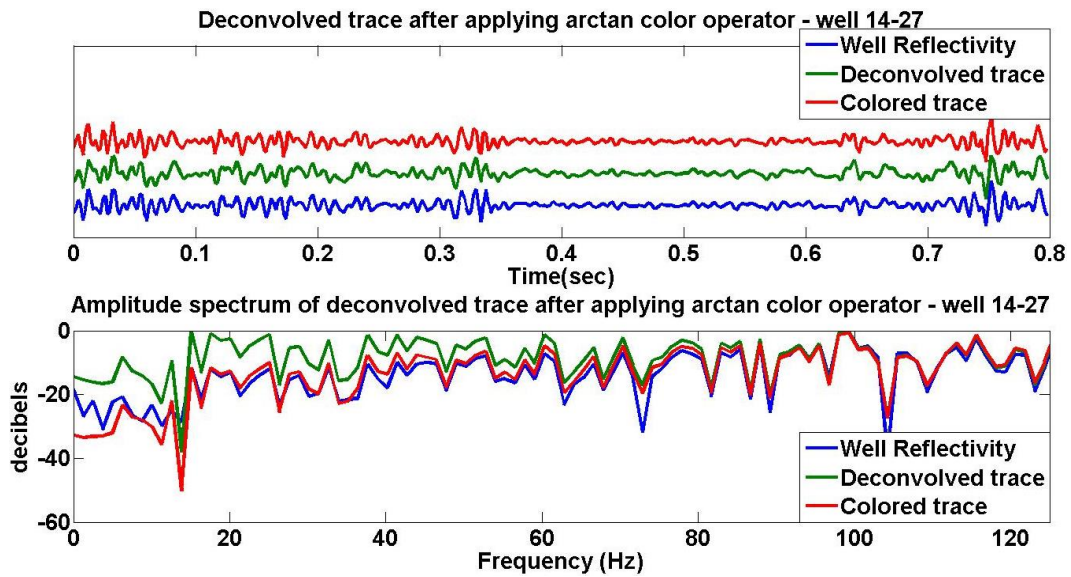


Figure 3.42. The result of applying arctan color operator on the deconvolved trace from well 14-27 in the time and frequency domain and comparing it with the deconvolved trace without applying color operator.

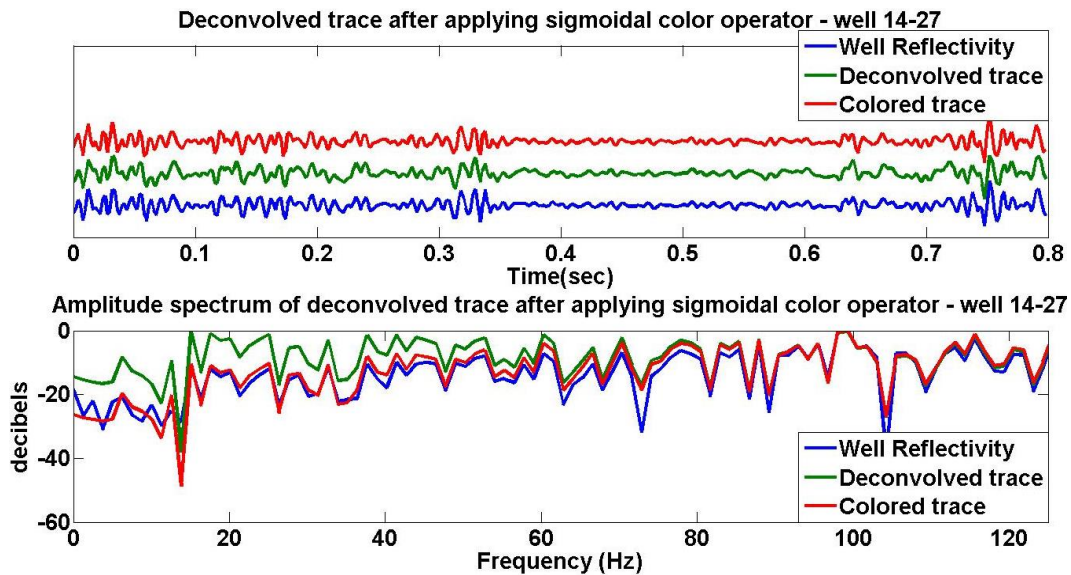


Figure 3.43. The result of applying sigmoidal color operator on the deconvolved trace from well 14-27 in the time and frequency domain and comparing it with the deconvolved trace without applying color operator.

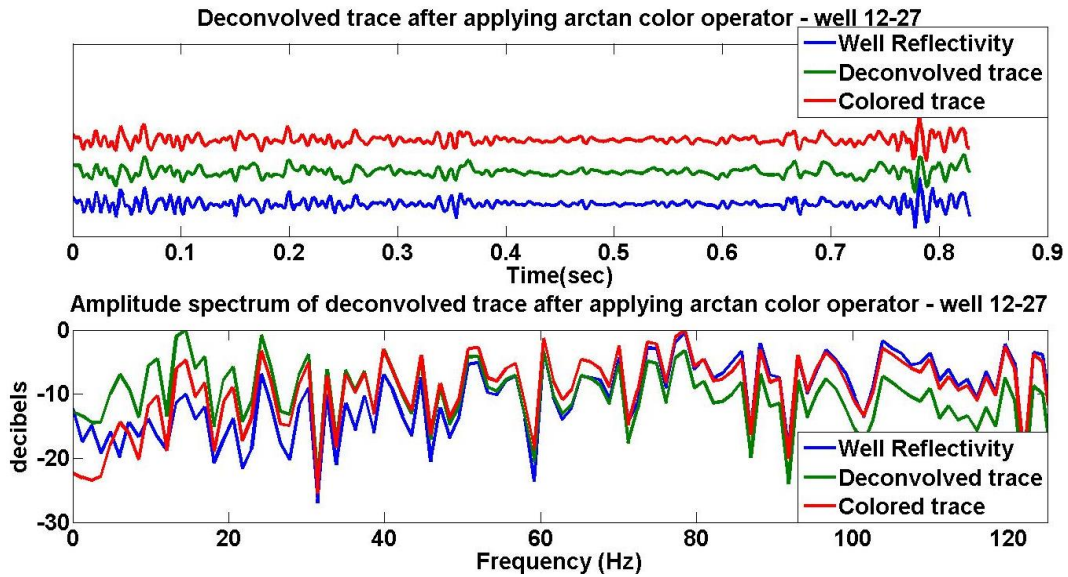


Figure 3.44. The result of applying arctan color operator on the deconvolved trace from well 12-27 in the time and frequency domain and comparing it with the deconvolved trace without applying color operator.

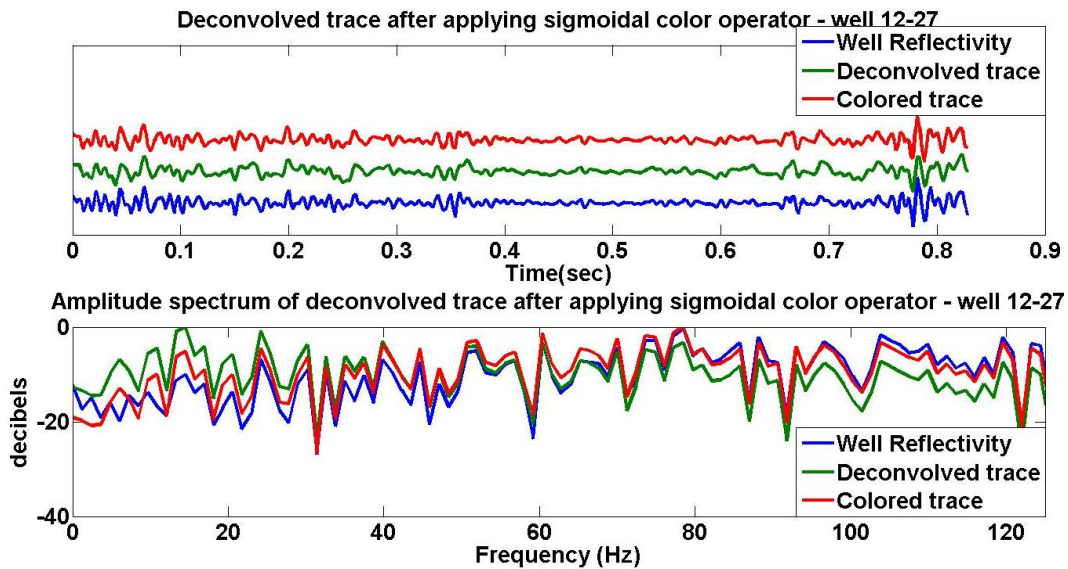


Figure 3.45. The result of applying sigmoidal color operator on the deconvolved trace from well 12-27 in the time and frequency domain and comparing it with the deconvolved trace without applying color operator.

As can be seen from these figures, applying the color operators to the deconvolved traces in all three well locations the reflectivity estimations for frequencies between 10Hz to 60Hz significantly improved. These results can be compared with the result of applying AC color

operator to the same data. The results are shown in the next three figures for well 14-35, 14-27 and 12-27 respectively.

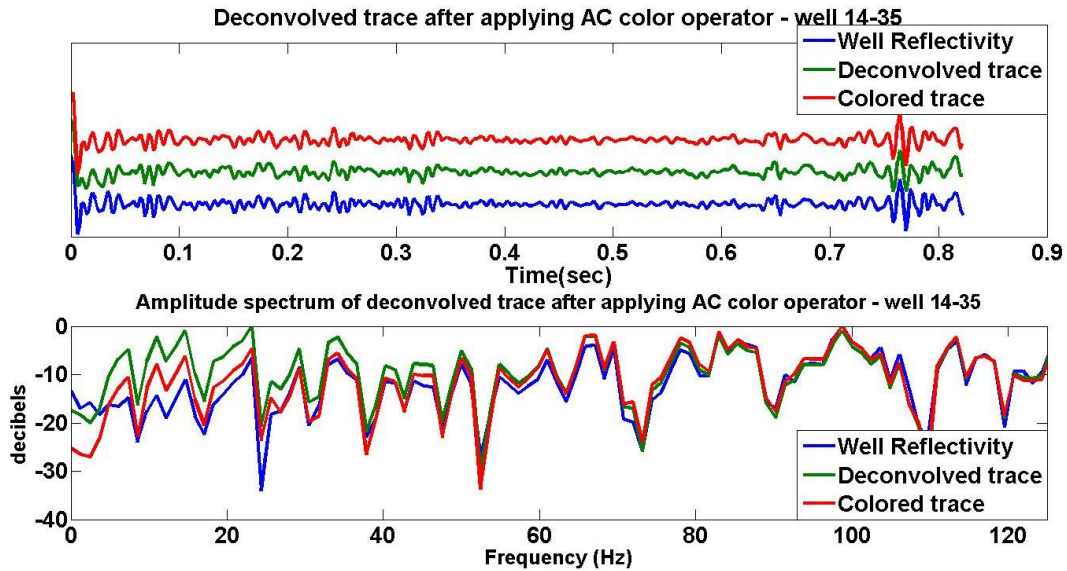


Figure 3.46. The result of applying AC color operator on the deconvolved trace from well 14-35 in the time and frequency domain and comparing it with the deconvolved trace without applying color operator.

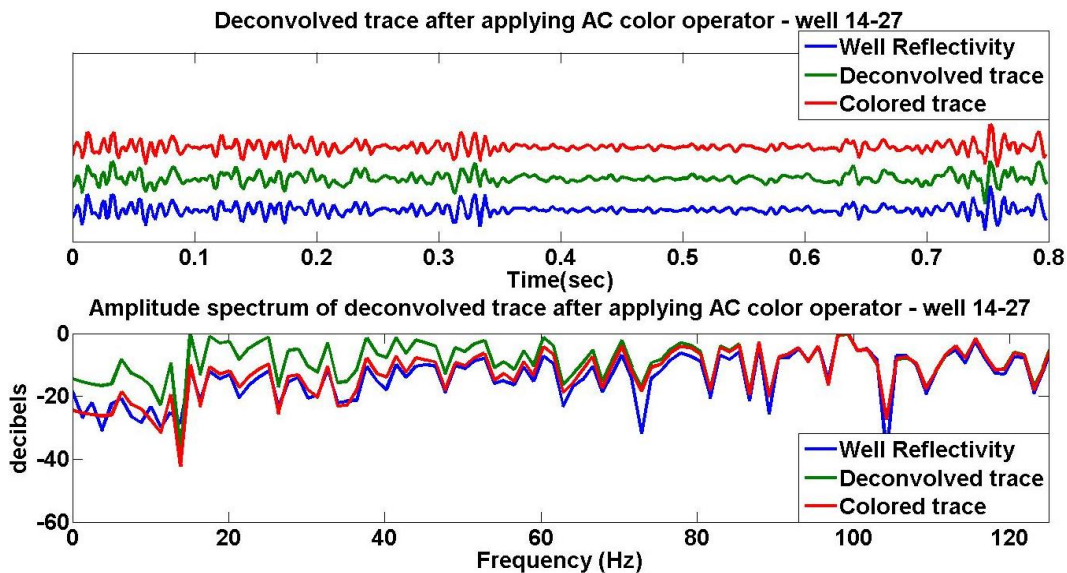


Figure 3.47. The result of applying AC color operator on the deconvolved trace from well 14-27 in the time and frequency domain and comparing it with the deconvolved trace without applying color operator.

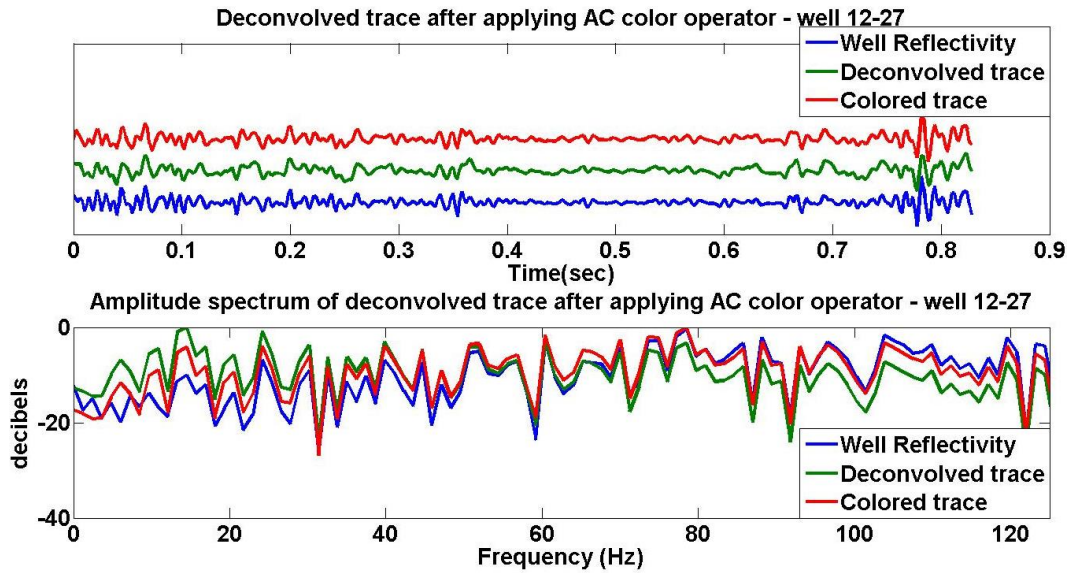


Figure 3.48. The result of applying AC color operator on the deconvolved trace from well 12-27 in the time and frequency domain and comparing it with the deconvolved trace without applying color operator.

The results of maximum correlation between estimated reflectivity and real well reflectivity also are shown in **Error! Reference source not found.** for before and after applying each color operator.

	Before applying color operator	After applying arctan color operator	After applying sigmoidal color operator	After applying AC color operator
Well 14-35	0.8980	0.9743	0.9795	0.9576
Well 14-27	0.8731	0.9682	0.9780	0.9638
Well 12-27	0.7926	0.9550	0.9598	0.9267

Table 3.3. The maximum correlation calculated between estimated reflectivity after using one of the color operators and real reflectivity.

The results show that applying any type of color operator is a robust method to improve the reflectivity estimation. The next step is computing the acoustic impedance for each case and compare it with the result of colored inversion as described at the beginning of this part. Note that

the recursion formula (Equation 1.19) has been used to calculate each of the acoustic impedances. To do this, the corrected calculated reflectivity with color operator can be used in recursion formula to calculate the acoustic impedance. The results for the data in all three wells location illustrate in figures Figure 3.49, Figure 3.50 and Figure 3.51.

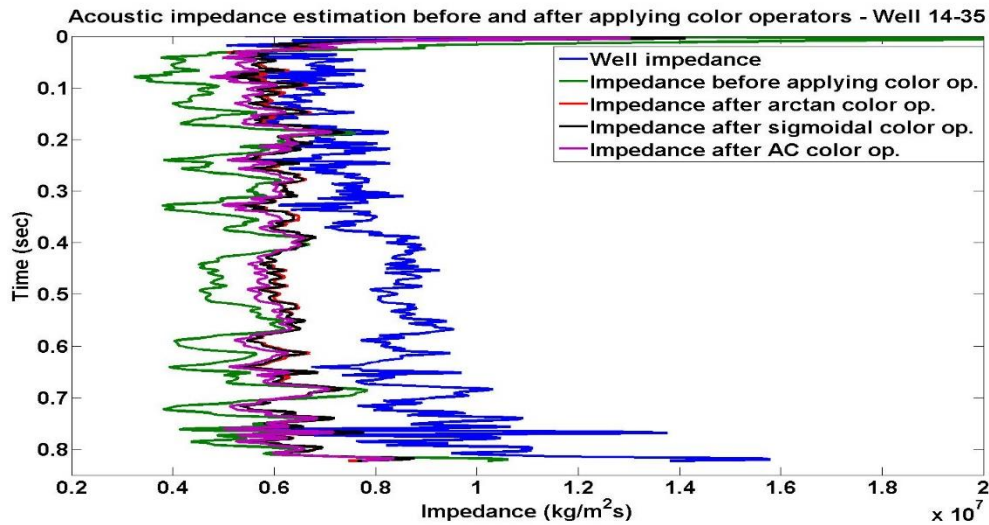


Figure 3.49. The acoustic impedance was calculated for well 14-35 data after and before applying color operator to see the effect of different color operators on impedance results. The results show improvements when the color operators have been used after deconvolution.

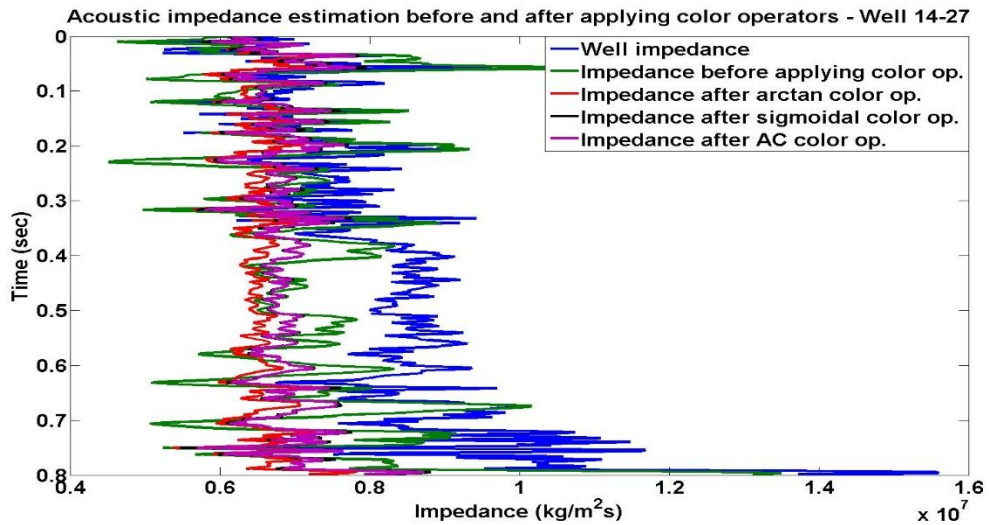


Figure 3.50. The acoustic impedance was calculated for well 14-27 data after and before applying color operator to see the effect of different color operators on impedance results. The results show improvements when the color operators have been used after deconvolution.

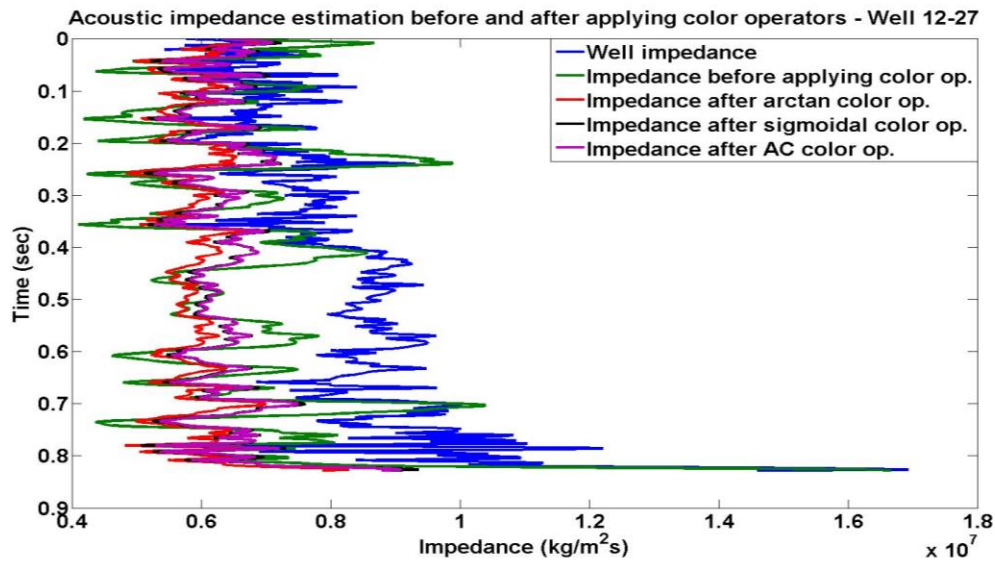


Figure 3.51. The acoustic impedance was calculated for well 12-27 data after and before applying color operator to see the effect of different color operators on impedance results. The results show improvements when the color operators have been used after deconvolution.

All the impedance plots show the improvements when the color operators have been used in compared with not using color operator. However, there are part of low frequency information that still misses and its consequence is inaccurate impedance estimation even after applying color operators. Thus to get more accurate impedance result the low frequencies from the wells are needed. This can be done using BLIMP algorithm which is in CREWES MATLAB toolbox. The acoustic impedance has been calculated once more using BLIMP algorithm with different low cut-off frequency from data with and without color operator and then the maximum correlation between each of estimated impedance and well reflectivity have been calculated. The result of computed maximum correlations versus the low cut-off frequency for three Hussar wells have been displayed in figures.

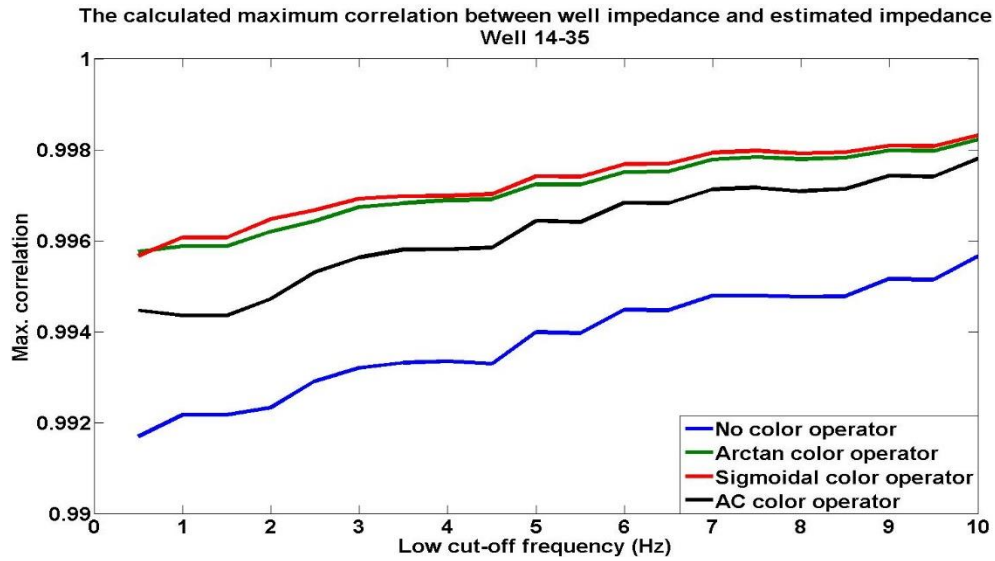


Figure 3.52. The maximum correlation results between estimated acoustic impedances with BLIMP algorithm and well 14-35 impedance. Different low cut-off frequencies have been used in BLIMP algorithm.

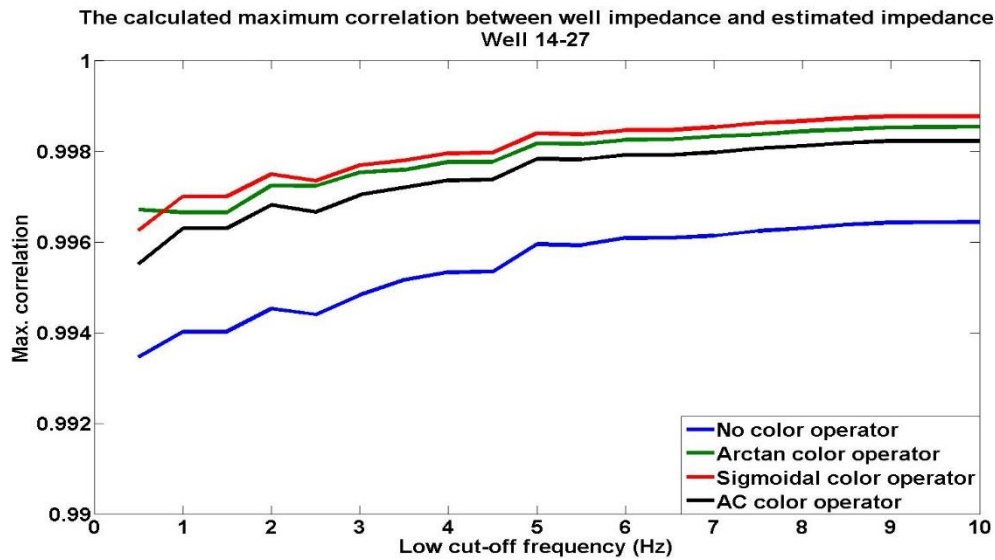


Figure 3.53. The maximum correlation results between estimated acoustic impedances with BLIMP algorithm and well 14-27 impedance. Different low cut-off frequencies have been used in BLIMP algorithm.

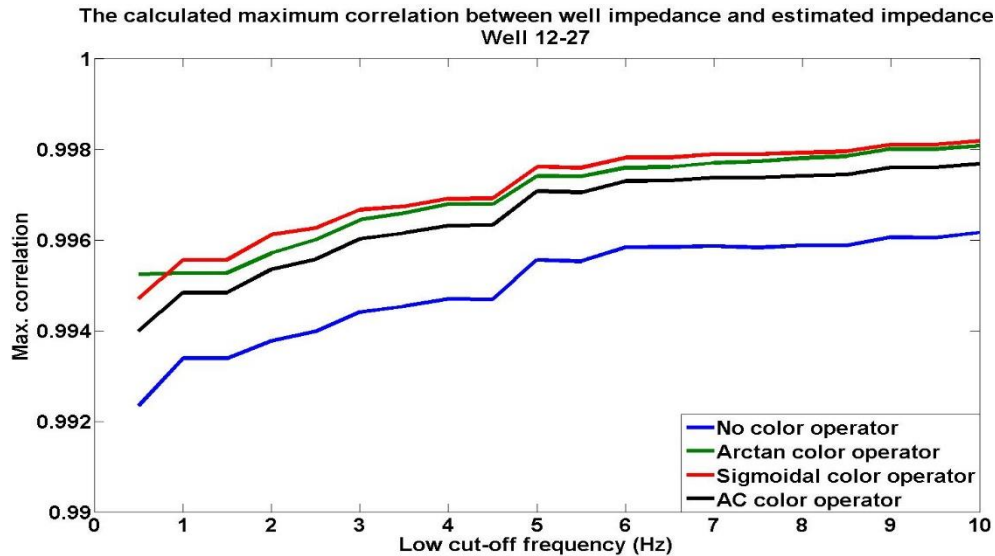


Figure 3.54. The maximum correlation results between estimated acoustic impedances with BLIMP algorithm and well 12-27 impedance. Different low cut-off frequencies have been used in BLIMP algorithm.

The figures demonstrate that for a specific low cut-frequency the best correlation between well impedance and estimated impedance happens when one of the color operators have been applied on the deconvolved traces. As mentioned previously, based on Heather Lloyd (2013) investigations the optimum low frequency cut off choice for Hussar seismic data is between 3 and 4 Hz and the results illustrate by using this low cut-off frequency range in BLIMP algorithm we can reach better results if the color operators have been applied to the deconvolved traces.

In the next chapter the Hussar seismic data will be discussed and it will be seen that how these minimum-phase color operators can affect the real seismic data and acoustic impedance section.

### 3.5 Summary

- The reflectivity calculated from well log data is in depth and has very detailed information. This needs to be converted into the time domain using 2-way time-depth table to be able correlate with the seismic data.

- The reason that the frequency domain deconvolution is not able to estimate the reflectivity precisely especially in the low frequencies and is not only because of the smoothing process. The colored spectrum property of the real reflectivity in the low frequencies causes any method of smoothening to become unsuccessful in this matter.
- Unlike the random reflectivity which has a white spectrum, the amplitude spectrum of well reflectivity at the low frequency part rolls off and this refers to the spectral color.
- The objective of the color operator is to create a model that represents the color trend in the spectrum without reproducing the specific characteristics of reflectivity that must be preserved in the seismic; such as the reflections to be interpreted.
- The color operator should depend only on the observed spectral shape of the reflectivity. Also, this operator needs to correct the error of minimum-phase whitening deconvolution operator, therefore it must be minimum-phase.
- Three different color operators have been studied in this thesis. Autocorrelation Color (AC) operator which has been calculated from well reflectivity autocorrelation and arctan and sigmoidal color operator which have been calculated from curve fitting method.
- The spectral rolling off effect in the amplitude spectrum of reflectivity at the frequencies higher than half of Nyquist frequency is because of applying anti-alias filter which means using higher sample rates shifts the anti-alias filter effect to higher frequencies.
- The color operator can correct the whitening deconvolution errors of deconvolved trace but it is not able to recover all the low frequency components.

- The BLIMP algorithm is a robust method to calculate more accurate impedance from bandlimited seismic data by adding low frequency information from well log data. The results showed using color operator can improve the impedance estimation of BLIMP.

## **CHAPTER FOUR: EFFECT OF MINIMUM-PHASE COLOR OPERATOR ON HUSSAR REAL DATA**

### **4.1 Introduction**

As mentioned previously, in September 2011, CREWES with cooperation of Husky Energy initiated a seismic experiment near Hussar in Alberta. After the data was collected at the field, CGG Veritas implemented a specialized processing flow. Normally a high-pass filter is applied to the data to remove noise such as ground roll. This high-pass cut-off of the filter can be as high as 10 Hz. To preserve the low-frequency reflection signal, a different noise attenuation was needed. Some of these methods were as follows: removing sinusoidal noise caused by power lines and pump-jacks, attenuating coherent noise and attenuating anomalous high amplitude frequencies. These noise attenuation procedures were repeated several times during the processing flow. Scaling was also specialized as trace equalization or an AGC was undesired. Geometrical spreading gain recovery and surface consistent scaling was implemented instead. Phase coherence, which is an indicator of coherent signal at any particular frequency, was measured by CREWES and reflection signal was estimated to be present down to frequencies as low as 1 to 5 Hz in the dynamite data (Isaac et al, 2012). The fully processed section, (Figure 4.1) when compared to the well reflectivity, has underestimated amplitudes from 0 to 1 second. This may be a result of trying to reduce the noise in the near surface and inadvertently reducing the signal amplitudes as well. This needs to be corrected for but should not be done with conventional scaling operators such as an AGC as this adversely affects the phase coherence of the data (Isaac et al, 2012) by boosting noise in the low frequencies that the specialized noise attenuation attempted to reduce. An AGC also equalizes the energy on the trace which does not keep the true relative reflectivity intact. Scaling was achieved by tying well 14-27, using a bulk shift, to the seismic and computing a time variant balancing algorithm with a window size of 50 ms and an

increment of 10 ms to balance the seismic data with synthetic seismogram created from well 14-27.

The resulting seismic section is shown in Figure 4.2.

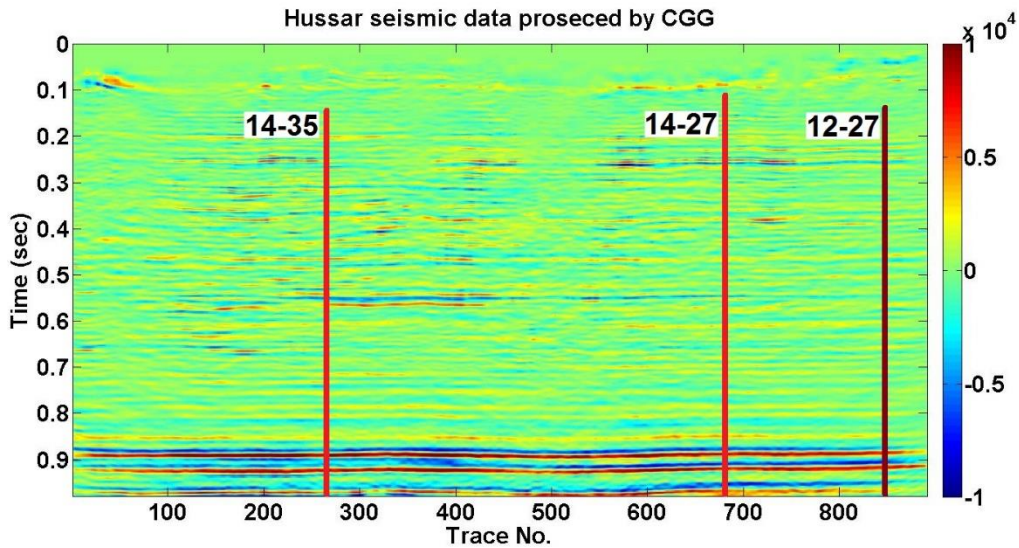


Figure 4.1. Hussar seismic data processed by CGG Veritas and the location of three wells.

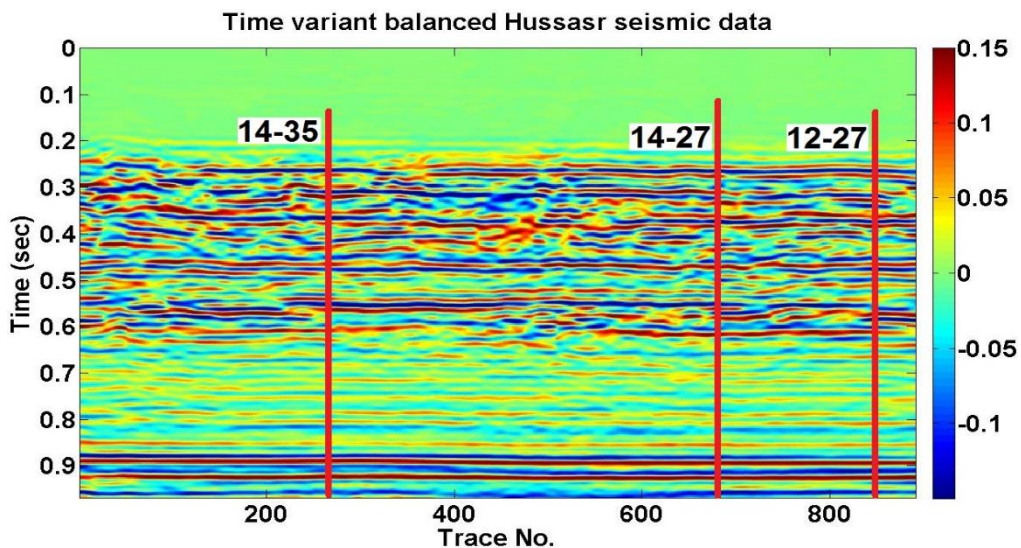


Figure 4.2. The time variant balancing operator applied to the Hussar seismic data.

#### 4.2 Data preparation

Before the wells can be tied to the seismic data they must first have an overburden applied. The overburden extends the wells to the surface and makes the well tying process easier. An overburden was modeled using a linear gradient for the P-wave velocity and density this has been done

with the SYNGRAM software which is a CREWES Matlab software. The surface value for the P-wave velocity and density was set 1100 m/s and 1500 kg/m<sup>3</sup> and the end value of the gradient blended into the top of the well log. The P-wave velocity and density logs for well 14-35, 14-27 and 12-27 are displayed in Figure 4.3, Figure 4.4 and Figure 4.5 , respectively.

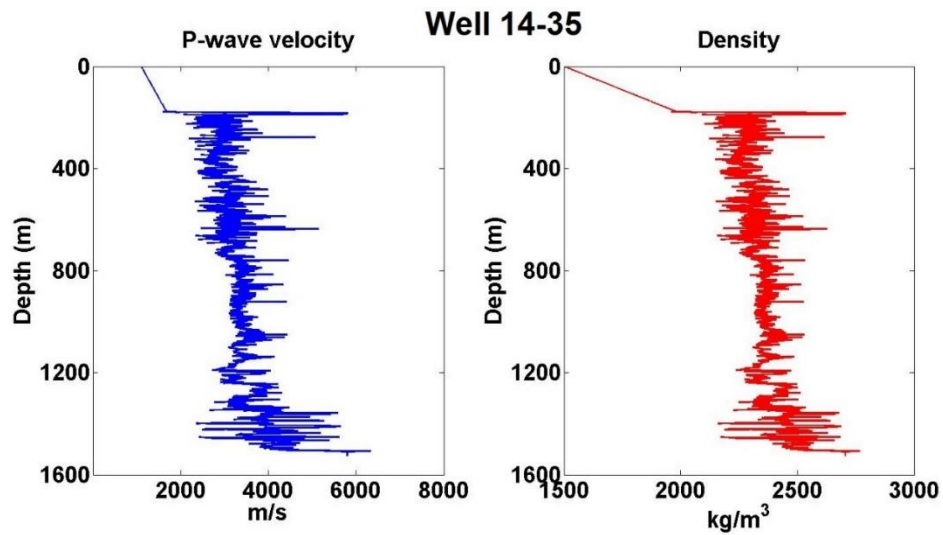


Figure 4.3. P-wave velocity and density logs of well 14-35 from Hussar data.

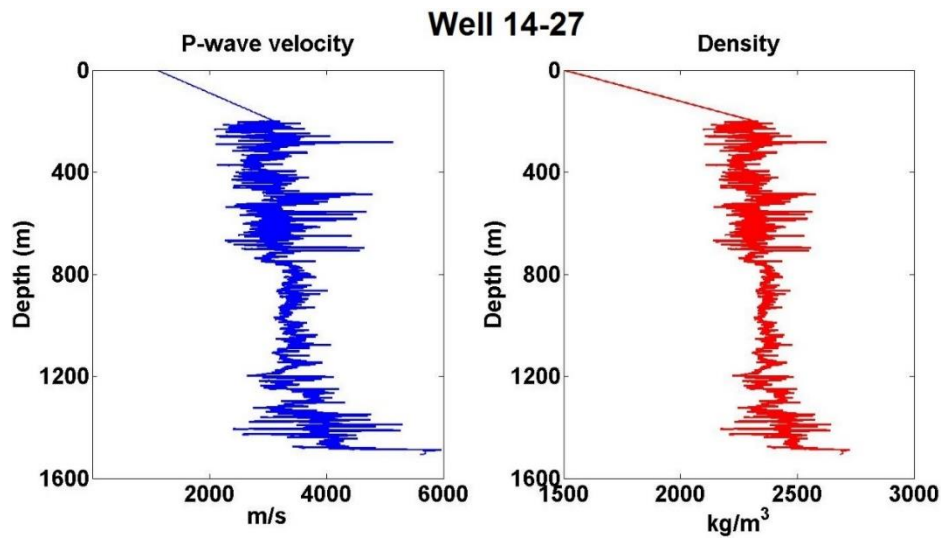


Figure 4.4. P-wave velocity and density logs of well 14-27 from Hussar data.

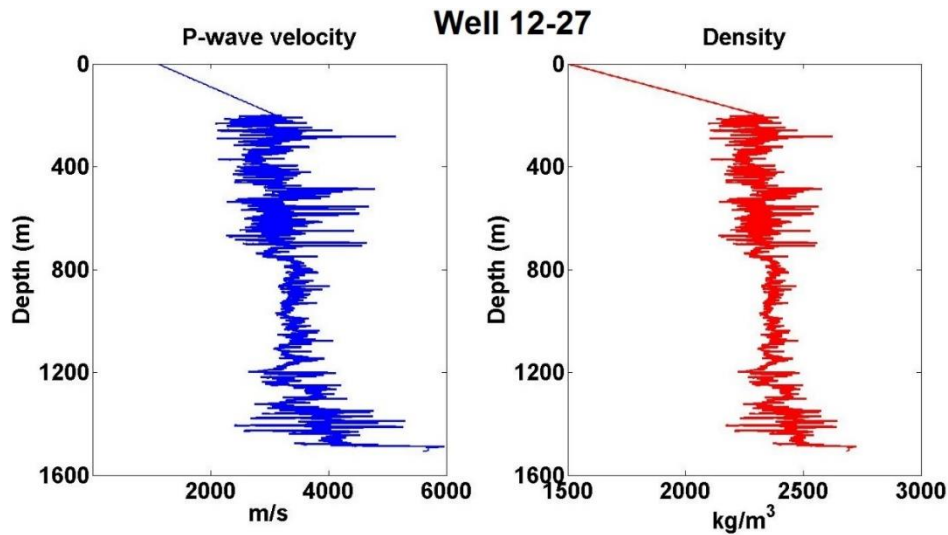


Figure 4.5. P-wave velocity and density logs of well 12-27 from Hussar data.

After modeling the overburden area, for tying the wells to the seismic data, the zero-phase synthetic data have been created from the well log data. This can be done with “seismo” function from CREWES Matlab toolbox which basically convolves the zero-phase wavelet with the time-domain reflectivity function. Generally, the well tie process includes a time shift and a phase rotation and because of attenuation it may contain an extra time shifts at deeper events. This can be fixed numerically with a method such as dynamic time warping (DTW) method (Cui and Margrave, 2014) or manually by stretching the synthetic trace. Here, after applying 0.002s, 0.044s and -0.014s time shift for synthetic seismic traces of wells 14-35, 14-27 and 12-27 respectively, the time stretching also needs to be applied to the synthetic data. (Figure 4.6)

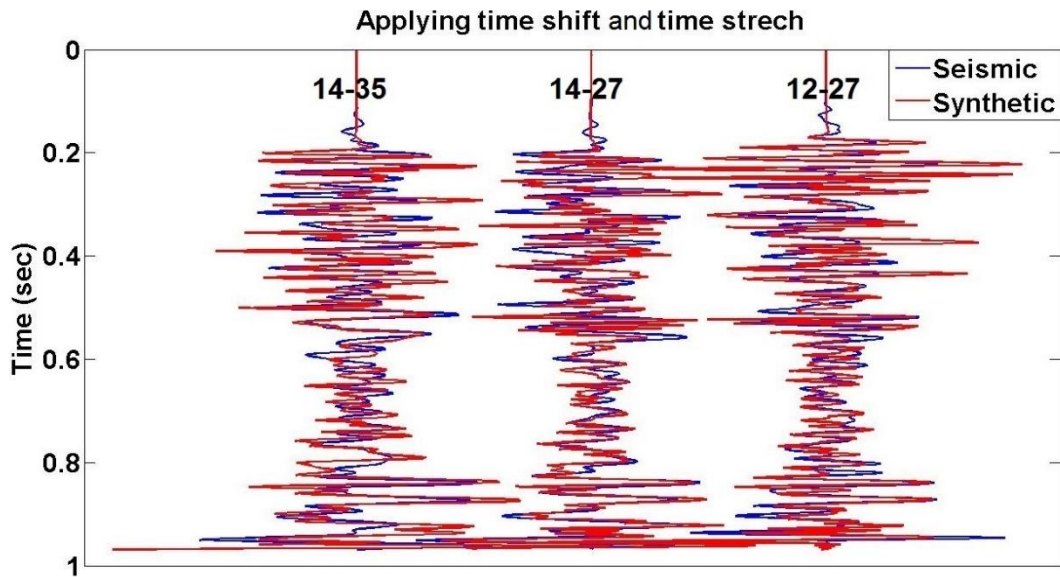


Figure 4.6 Applying appropriate time shifting (and if applicable phase shifting), because of attenuation, different time slices might need different time shifts. This can be done by time stretching algorithm.

As can be seen from this figure, at all three well locations there are good matches between seismic traces and synthetic traces. The calculated cross correlations between each synthetic and seismic pairs are 0.5561, 0.5370 and 0.5588 for wells 14-35, 14-27 and 12-27 respectively and all have been occurred at zero lag.

### 4.3 Color operator effects on seismic data and impedance inversion

Once the synthetic seismic data has been successfully tied to the real seismic data, we can apply different color operators to the stacked seismic section. Using two different methods the color operators can be applied to the seismic section. We can average three color operators which were created from the three Hussar wells and then the averaged color operator can be applied to the entire seismic section or, by spatial interpolation between three color operators, a unique color operator can be computed for each seismic trace. In this study three color operator types (AC color operator, arctan color operator and sigmoidal color operator) have been calculated for the whole seismic section using the spatial interpolation method. Once it has been done, each trace of seismic

section can be convolved with its related color operator. The result of applying minimum-phase AC, arctan and sigmoidal color operators to the seismic section are shown in the Figure 4.7, Figure 4.8 and Figure 4.9. At each figure the left hand side one is before applying color operator and the right hand side is after applying color operator respectively.

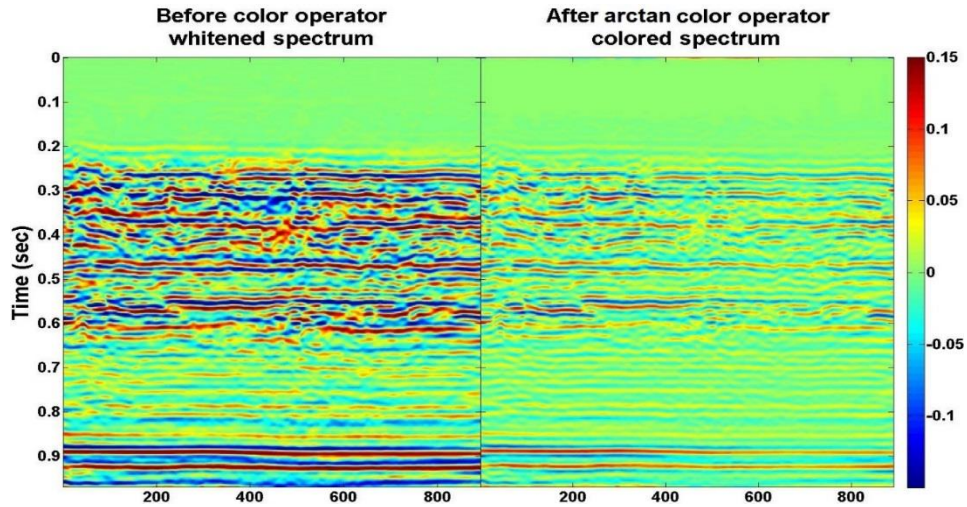


Figure 4.7. The effect of applying arctan color operator on Hussar seismic data. (left) before applying color operator and (right) after applying color operator. The results show that the seismic data after applying color operator become dim which means their power of amplitude at the low frequency part are decreasing.

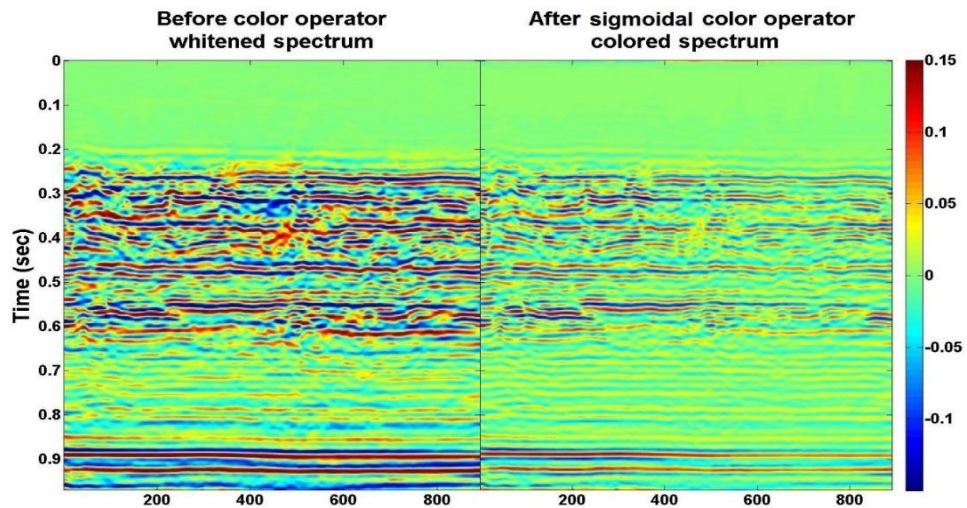


Figure 4.8. The effect of applying sigmoidal color operator on Hussar seismic data. (left) before applying color operator and (right) after applying color operator. The results show that the seismic data after applying color operator become dim which means their power of amplitude at the low frequency part are decreasing.

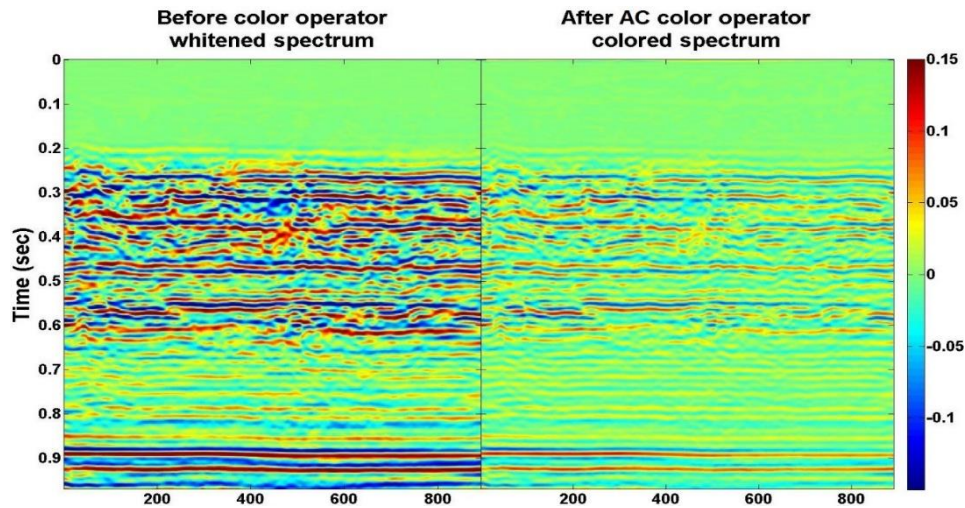


Figure 4.9. The effect of applying AC color operator on Hussar seismic data. (left) before applying color operator and (right) after applying color operator. The results show that the seismic data after applying color operator become dim which means their power of amplitude at the low frequency part are decreasing.

The apparent dimming of the seismic data after applying color operator happens because the operator suppresses the lower frequencies which were previously equal in strength to the higher frequencies because of spectral whitening. This can be proven by looking at the amplitude spectrum of an arbitrary trace from the seismic section before and after applying color operator. For example, the amplitude spectrum of seismic trace near well 14-27 before and after applying color operator have been displayed in figures Figure 4.10, Figure 4.11 and Figure 4.12.

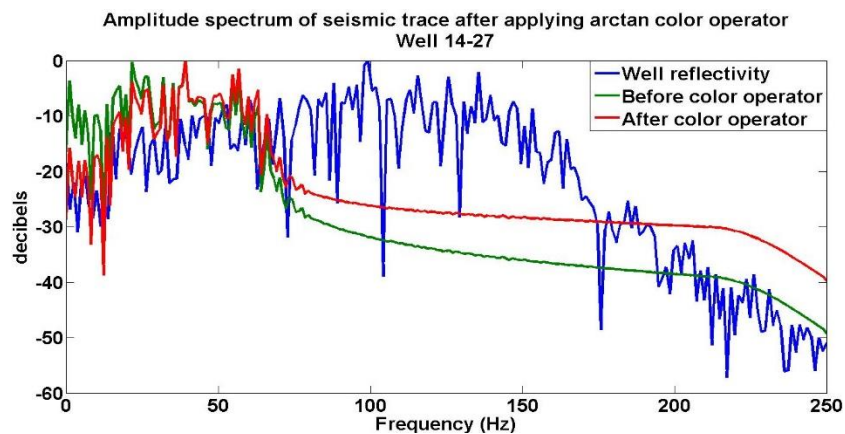


Figure 4.10. The amplitude spectrum of trace from Hussar seismic data near well 14-27 before and after applying arctan color operator.

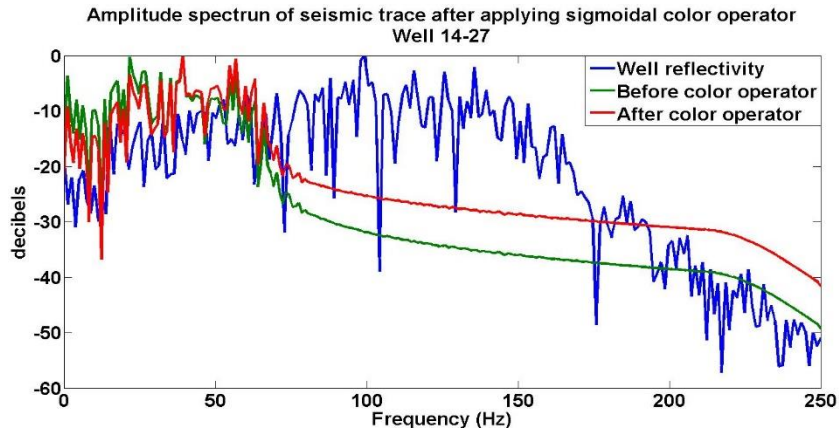


Figure 4.11. The amplitude spectrum of trace from Hussar seismic data near well 14-27 before and after applying arctan color operator.

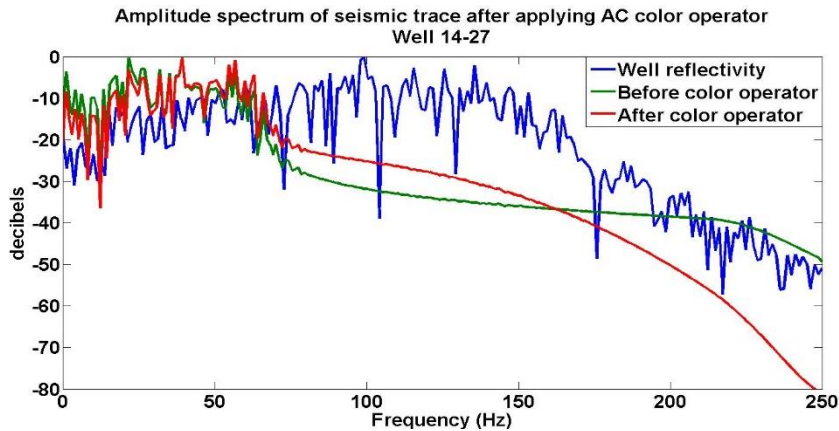


Figure 4.12. The amplitude spectrum of trace from Hussar seismic data near well 14-27 before and after applying AC color operator.

These three figures demonstrate that applying any of color operators to the stacked seismic traces causes their amplitude spectrum to roll off in low frequency to become similar with the spectral shape of well reflectivity. This causes the whole section to become dim as can be seen in figures Figure 4.7 to Figure 4.9. More similarity between the spectral shape of seismic trace and reflectivity means better estimation of amplitude spectrum which causes the colored seismic section to become de-whitened.

#### 4.4 Acoustic impedance inversion

Once the data have been prepared and the color operator has been applied, we are able to invert them to the impedance section. As mentioned previously, using the recursion formula (equation 1.19) for calculating the acoustic impedance from bandlimited seismic data is not a reliable method and cannot estimate the true acoustic impedance. However, to illustrate the effect of color operators in acoustic impedance calculation, the impedance section has been computed directly from recursion formula using seismic data before and after applying color operator (Figure 4.13).

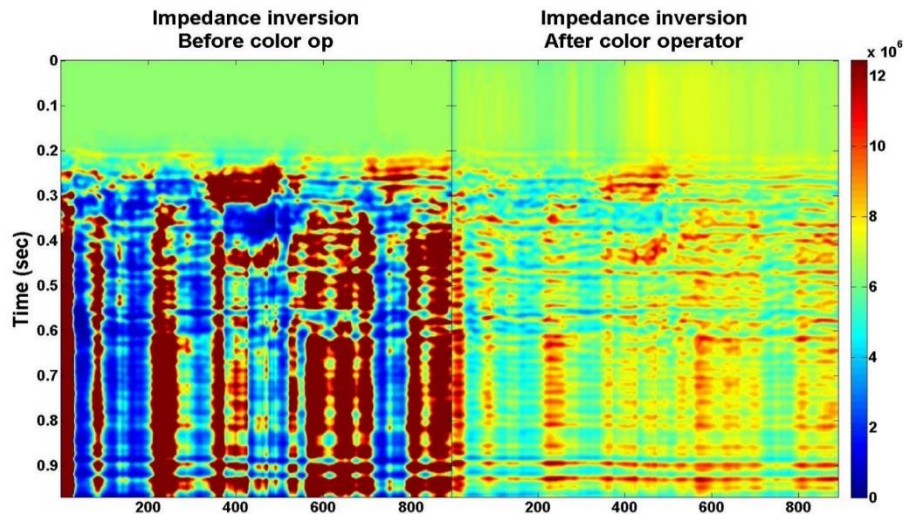


Figure 4.13 Impedance inversion using recursion formula for the seismic data before and after applying color operator.

This result demonstrates the significant changes in impedance inversion section after applying color operator. However, to get the correct impedance results, the low frequency components need to be inserted from the well log data. This can be done using BLIMP algorithm which is in CREWES MATLAB toolbox. As mentioned previously, the BLIMP function has two frequency input parameters: low cut off frequency and high cut off frequency. The low cut off frequency is the value below which the algorithm suppresses the seismic frequencies and inserts

the same frequencies from the well log. However, the frequencies higher than the high cut off frequency are totally removed from data via BLIMP algorithm. To compute an accurate inversion the low frequency cut off must be chosen with care. If the cut off is too low, low frequency noises from the seismic data will contaminate the inversion. If the cut off is too high, the inversion is overwhelmed by well information and subtle details from the seismic data cannot be seen. Lloyd (2013) discussed in detail the optimum low frequency cut off choice for Hussar seismic data and based on the results the best choice of low cut off frequency is between 3 and 4 Hz.

In this study we used 3.5 Hz as a low cut off frequency and the high cut off frequency is varying from 60 to 70 Hz from the side of well 14-35 to the side of well 12-27. The acoustic impedance inversion results before and after applying color operator are displayed in Figures Figure 4.14, Figure 4.15, Figure 4.16 and Figure 4.17.

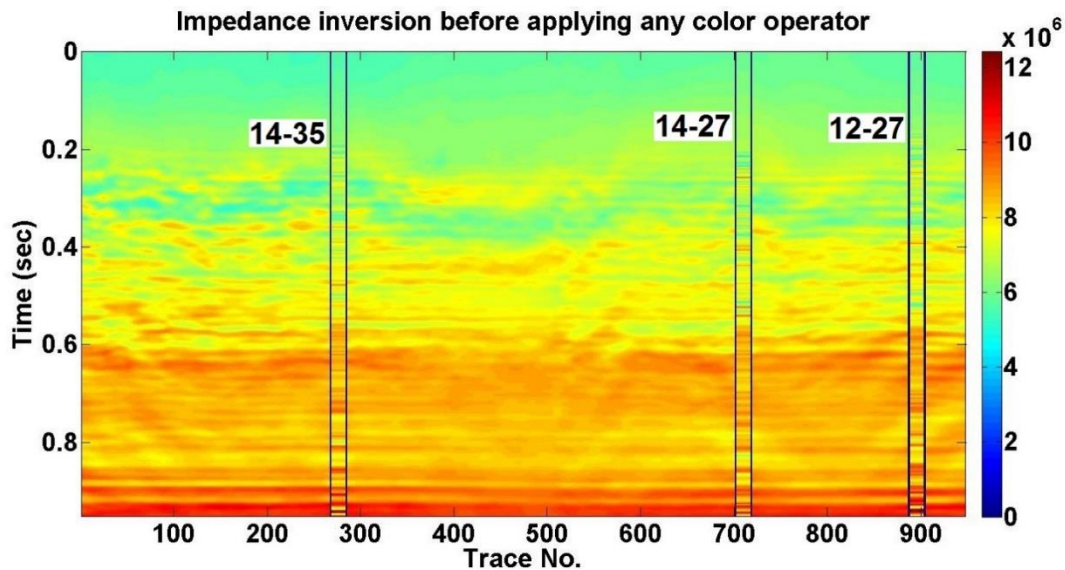


Figure 4.14. The BLIMP impedance inversion without using any color operator. The low frequency in BLIMP algorithm was chosen 3.5Hz and the high frequency is linearly varying from 60Hz to 70Hz from left to the right side of seismic section.

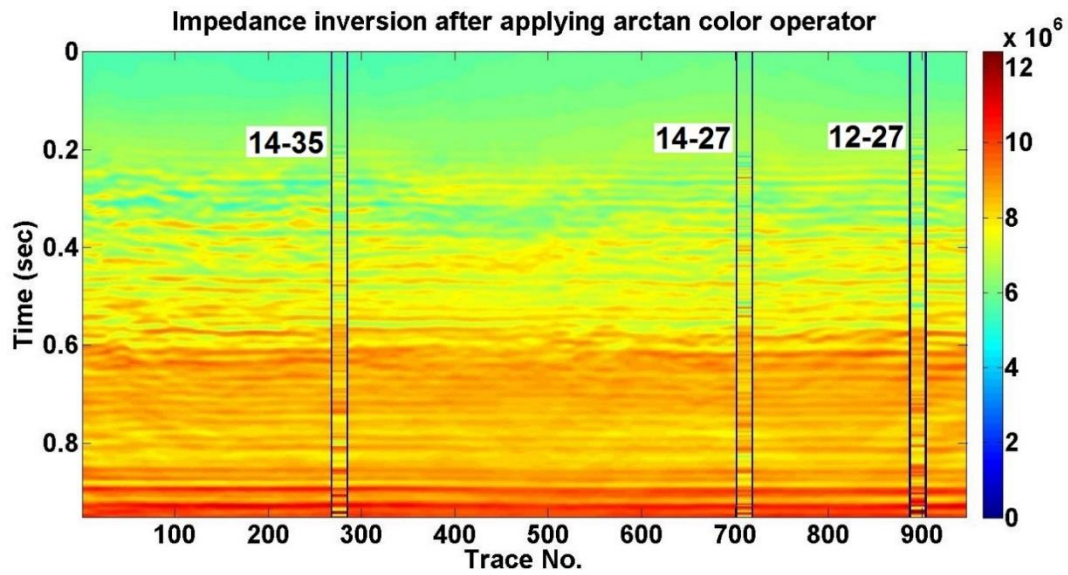


Figure 4.15. The BLIMP impedance inversion for arctan color operator. The low frequency in BLIMP algorithm was chosen 3.5Hz and the high frequency is linearly varying from 60Hz to 70Hz from left to the right side of seismic section.

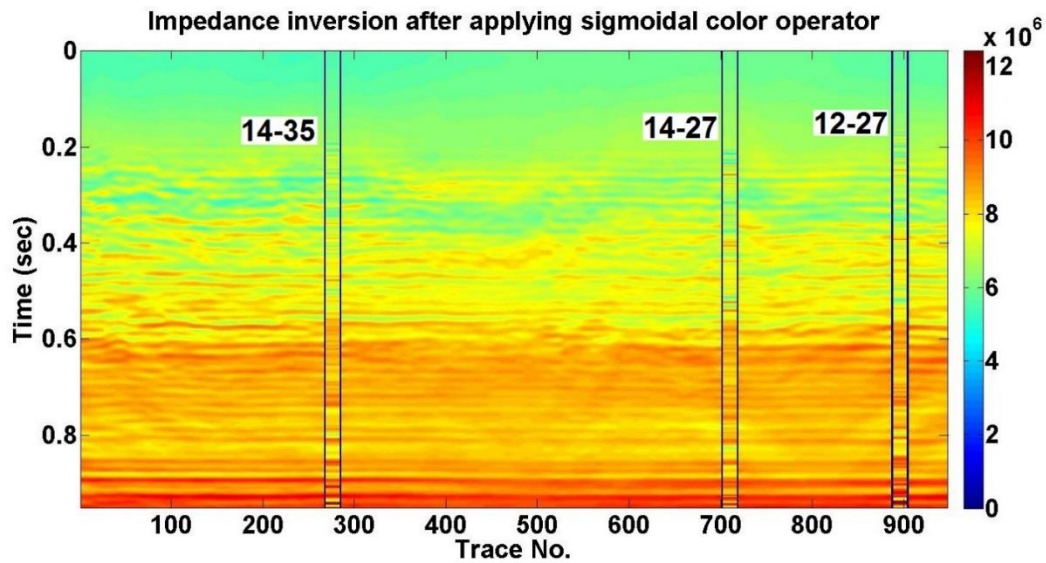


Figure 4.16. The BLIMP impedance inversion for sigmoidal color operator. The low frequency in BLIMP algorithm was chosen 3.5Hz and the high frequency is linearly varying from 60Hz to 70Hz from left to the right side of seismic section.

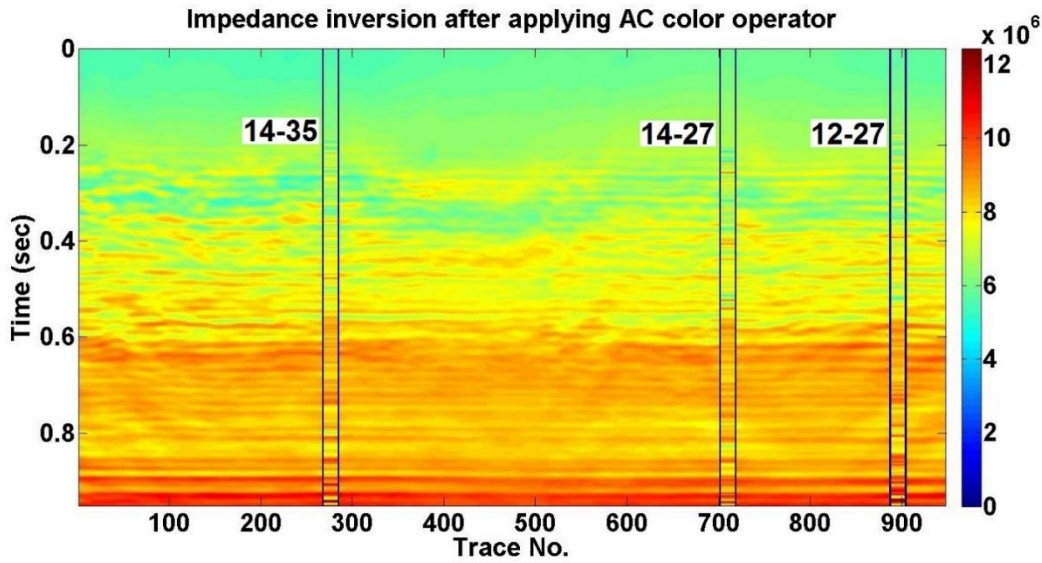


Figure 4.17. The BLIMP impedance inversion for AC color operator. The low frequency in BLIMP algorithm was chosen 3.5Hz and the high frequency is linearly varying from 60Hz to 70Hz from left to the right side of seismic section.

These figures demonstrate remarkable improvement in the acoustic impedance section after applying any of color operators related to the one without applying color operator. These improvements can be seen in layers resolution as well as matching with the well impedance at the well location. This can also be seen from computing the maximum correlation between calculated impedance and well impedance at the well locations for all types of color operators (Table 4.1).

	Well 14-35	Well 14-27	Well
Before color operator	0.4415	0.4261	0.4169
After arctan color op.	0.5568	0.6124	0.546
After sigmoidal color op.	0.5726	0.6088	0.5664
After AC color op.	0.5726	0.6083	0.5632

Table 4.1. The maximum correlation calculated for acoustic impedance estimation between the well impedance and the traces near those wells before and after applying color operator.

These results can be compared with the result of colored inversion method which was introduced by Lancaster and Whitcombe in 2000. As mentioned previously, this method was based

on deriving the spectral shape of well impedance and then the amplitude spectrum of the colored inversion operator is determined as being that which maps the seismic spectrum to a spectral shape of well impedance. To design this operator for the Hussar seismic data, first the average well impedance of three well log data has been calculated and then the appropriate  $\alpha$  value from fitting the  $f^\alpha$  curve to the amplitude spectrum of averaged impedance was found ( $\alpha = -0.8355$ ).

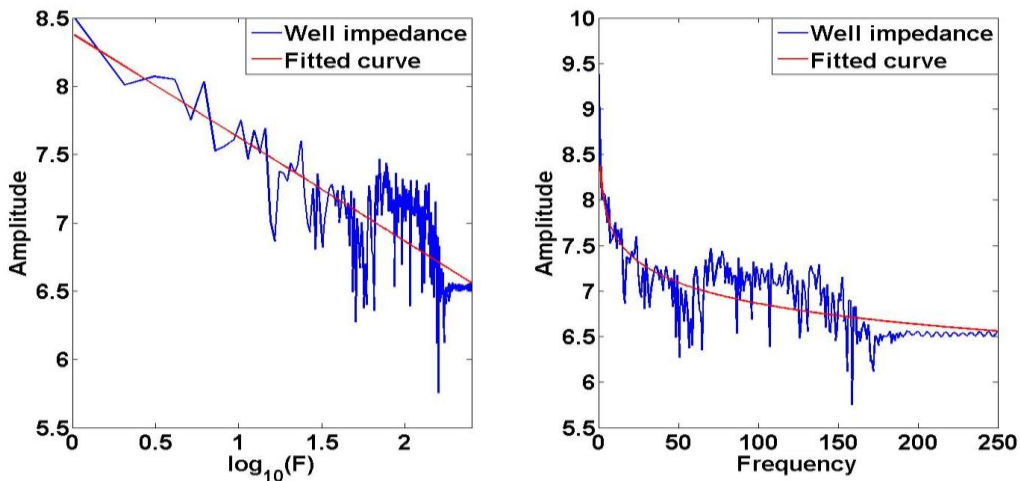


Figure 4.18. The colored inversion operator derivation process which needs to derive the spectral shape of well impedance.

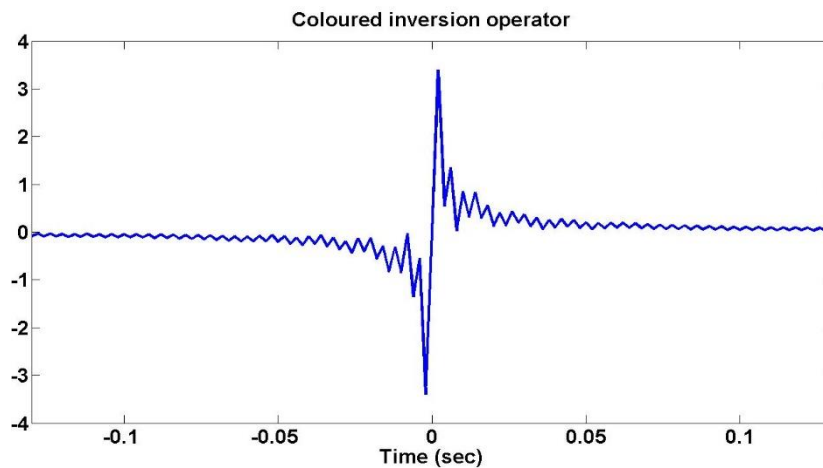


Figure 4.19. The designed colored inversion operator from averaged well impedance and averaged seismic trace of Hussar data.

Once the colored inversion operator was designed, it can be apply directly to the seismic section to give us the bandlimited impedance inversion. Figure 4.20 illustrates the result of colored inversion method of Hussar seismic data. Note that the calculated impedance has both positive and negative values. However, from our knowledge about acoustic impedance since it defines as a multiplication of velocity and density, its value cannot be a negative. Thus, the computed impedance in this case is only showing the variation of impedance from its trend not its real value.

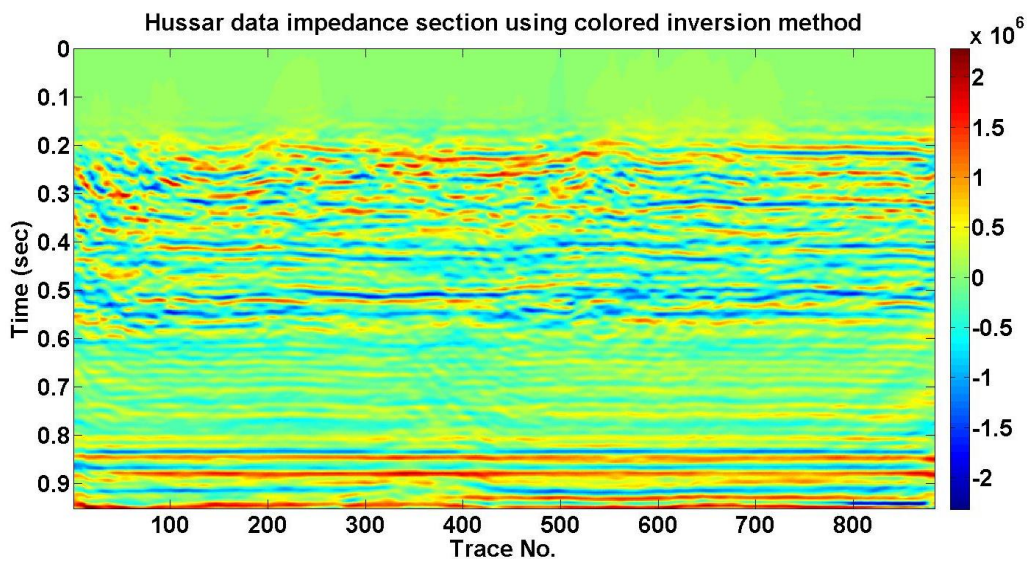


Figure 4.20. The result of applying colored inversion operator on Hussar seismic data. The computed impedance in this case is only showing the variation of impedance from its trend not its real value.

This is the consequence of lacking low frequencies in calculated acoustic impedance. On the other hand, as we can see in the Figure 1.13, the broadband impedance inversion can be divided into the two separate parts: the low frequency part which defines the trend of broadband impedance and the high frequency part which causes the impedance fluctuation. Thus, the results we have seen in the Figure 4.20 do not have a low frequency trend. To determine the approximate frequency range that includes in the colored inversion result, the amplitude spectrum of the traces near the well logs can be compared with the amplitude spectrum of the well impedance. These are shown

in Figure 4.21 and it shows the approximate range of frequency that colored inversion method contains is 14 to 62Hz at the location of well 14-35, 14 to 68Hz at the location of well 14-27 and 20 to 70Hz at the location of well 12-27.

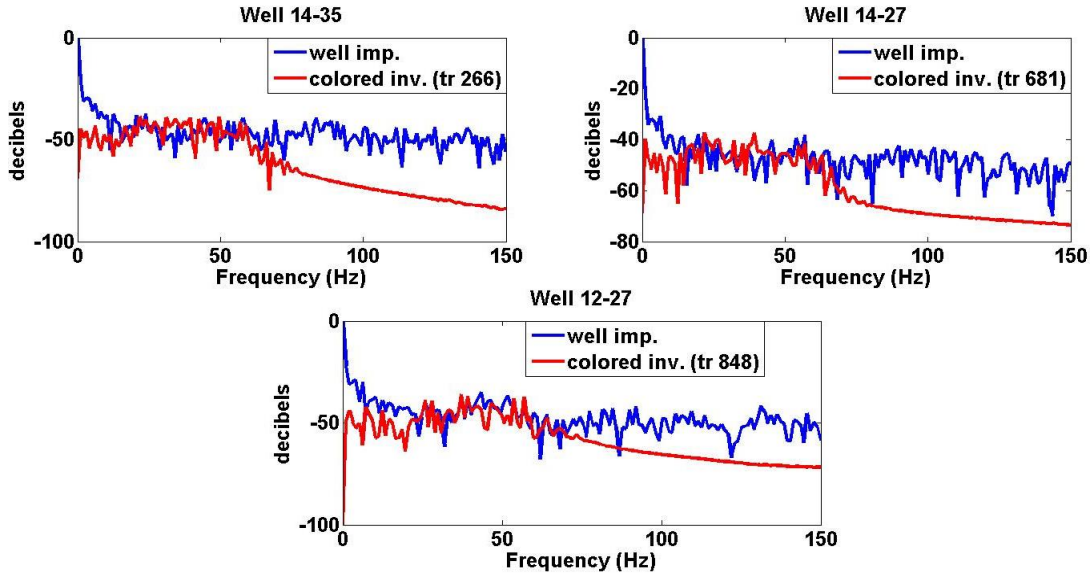


Figure 4.21. The amplitude spectrum of colored inversion result near each well and its comparison with the real acoustic impedance amplitude spectrum. The approximate range of frequency that colored inversion method contains is 14 to 62Hz at the location of well 14-35, 14 to 68Hz at the location of well 14-27 and 20 to 70Hz at the location of well 12-27.

The colored inversion results also can be compared with the result of -90 degree phase rotation of seismic data. As mentioned earlier, the colored inversion can be proportional to the -90 degree phase rotation of seismic data and this can be seen in Figure 4.22. The -90 degree phase rotation is the consequence of simple mathematical concept. Equation 1.19 can be written as

$$I(t) = I_1 e^{2 \int R(t) dt} . \quad 4.1$$

Thus, the integral operator applying to the reflectivity function which is roughly a -90 degree phase rotation. This can be shown mathematically. Consider the signal as

$$S(t) = \int_{-\infty}^{\infty} \widehat{S}(\omega) e^{-i\omega t} d\omega, \quad 4.2$$

where  $\widehat{S}(\omega)$  is the Fourier transform of  $S(t)$ . By taking the derivative of equation 4.2 with respect to  $t$

$$\begin{aligned} \frac{\partial S(t)}{\partial t} &= \frac{\partial \left( \int_{-\infty}^{\infty} \widehat{S}(\omega) e^{-i\omega t} d\omega \right)}{\partial t} = \int_{-\infty}^{\infty} \widehat{S}(\omega) \frac{\partial (e^{-i\omega t})}{\partial t} d\omega \\ &= \int_{-\infty}^{\infty} -i\omega \widehat{S}(\omega) e^{-i\omega t} d\omega. \end{aligned} \quad 4.3$$

In this equation  $-i$  can be written as

$$-i = \cos\left(\frac{\pi}{2}\right) - i \sin\left(\frac{\pi}{2}\right) = e^{-i\frac{\pi}{2}}, \quad 4.4$$

and by substituting this value in the equation 4.3, it becomes

$$\begin{aligned} \int_{-\infty}^{\infty} -i\omega \widehat{S}(\omega) e^{-i\omega t} d\omega &= \int_{-\infty}^{\infty} e^{-i\frac{\pi}{2}} \omega \widehat{S}(\omega) e^{-i\omega t} d\omega \\ &= \int_{-\infty}^{\infty} \omega \widehat{S}(\omega) e^{-i(\omega t + \frac{\pi}{2})} d\omega. \end{aligned} \quad 4.5$$

Equation 4.5 shows that the derivative operation corresponds to multiplying the amplitude spectrum by frequency and a +90 degree phase rotation. Since the integral operator is the inverse of derivative operator, the integral operator has a phase response that is a -90 degree phase rotation.

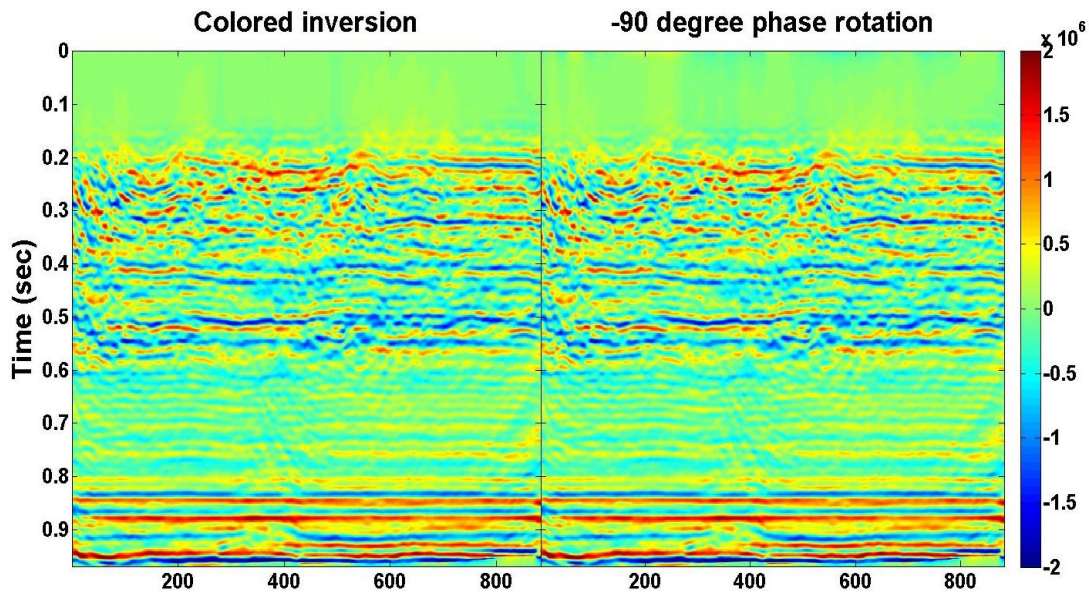


Figure 4.22. Comparing the result of colored inversion method and -90 degree phase rotation on seismic data.

To compare the result of acoustic impedance inversion calculated from applying different color operators it is easy to look at the calculated maximum correlation between well impedance and each of the methods near the well locations. The results have been computed for the frequency ranges between 14 and 60Hz to be able to compare all possible options. Chart 4.1 showing these calculated correlation for each of the methods. The results in the table demonstrate a noticeable difference when we are using the minimum-phase color operator. Besides that, to be able to compare with the colored inversion method, after applying proper filter to the estimated impedances from BLIMP and well impedance the results show using any of the color operators have more reliable and accurate result than using colored inversion method.

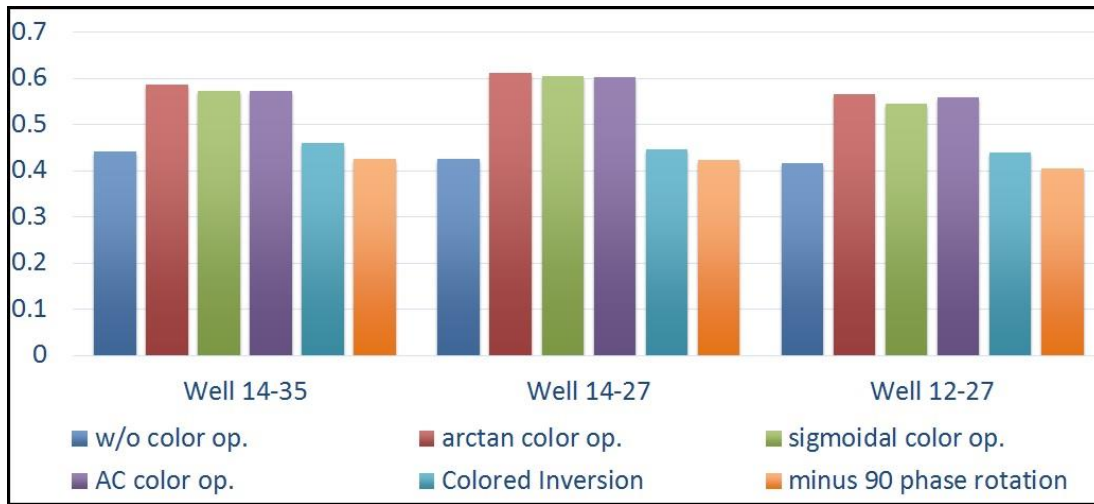


Chart 4.1. The maximum correlation calculated between well impedance and estimated acoustic impedance using different methods. The results have been compared for the frequency ranges between 14 and 60Hz to be able to compare all possible options.

#### 4.5 Summary

- To assist in the well tying process, calculating accurate P-wave velocity and density overburdens are necessary. A linear gradient has been used to calculate each of the overburdens to prevent artificial coefficients creation.
- Generally, the well tie process includes a time shift and a phase rotation and because of attenuation it may contain an extra time shifts at deeper events. This can be fixed numerically with a method such as dynamic time warping (DTW) method or manually by stretching the synthetic trace.
- A deconvolved trace shaped to a white spectrum can be corrected by applying a minimum-phase color operator after deconvolution.
- The minimum-phase color operator can be calculated separately for each well and then the average color operator can be applied to the whole seismic section or, by spatial interpolation between available color operators, a unique color operator can be computed for each seismic trace.

- Applying any of color operators to the stacked seismic traces causes their amplitude spectrum to roll off in low frequency to become similar with the spectral shape of well reflectivity. This causes the whole section to become dim.
- The result of impedance inversion is greatly improved after applying color correction because this affects the low frequencies and therefore the trend of the inversion.
- Colored inversion method is based on deriving the spectral shape of well impedance and then the amplitude spectrum of the colored inversion operator is determined as being that which maps the seismic spectrum to a spectral shape of well impedance.
- The colored inversion method is a fast and robust technique to calculate the deviation of acoustic impedance from background trend (e.g. no low frequency information) and it is similar to a -90 degree phase rotation.
- Comparing the maximum correlations between well acoustic impedance and estimated acoustic impedance from each method including before applying any color operator, after applying minimum-phase arctan, sigmoidal and AC color operator, colored inversion method and -90 degree phase rotation show that around 20 percent higher correlation can be reached if minimum-phase color operator has been applied to the deconvolved seismic data.

## CHAPTER FIVE: CONCLUSION

- Seismic reflectivity estimation is aimed at obtaining the true underground reflection information and improving the seismic vertical resolution, which is mainly restricted by the bandlimited source wavelet.
- Frequency domain deconvolution method assumes some fundamental assumptions such as:
  - The wavelet should be causal and minimum-phase.
  - The wavelet spectrum should be smooth.
  - The wavelet should be stationary.
  - The reflectivity is assumed to be random, thus its amplitude spectrum is white.
  - Any noise is additive, white and stationary.
- The minimum-phase wavelet does not refer to a particular phase spectrum which, if preserved, maintains a dataset's minimum-phase. Instead, the minimum-phase refers to a particular mathematical relationship existing between the amplitude and phase spectra so that knowledge of either one is sufficient to compute the other one. The mathematical relation between phase spectrum and amplitude spectrum can be found in equation 2.12.
- To calculate the frequency domain deconvolution operator, the amplitude spectrum of seismic trace must be smoothed to aim the wavelet estimation. This can be done with different smoother types. Boxcar smoother, constant Gaussian smoother and frequency dependent Gaussian smoother have been used.
- Applying different frequency domain deconvolution operators to the pseudo random data demonstrate significant improvement in impedance results when the frequency dependent Gaussian smoother has been used (Figure 2.20).

- The reflectivity calculated from well log data is in depth and has very detailed information. This needs to be converted into the time domain using 2-way time-depth table to be able to correlate with the seismic data.
- The reason that the frequency domain deconvolution is not able to estimate the reflectivity precisely especially in the low frequencies and that is not only because of the smoothing process. The colored spectrum property of the real reflectivity in the low frequencies causes any method of smoothing to become unsuccessful in this matter.
- Unlike the random reflectivity which has white spectrum, the amplitude spectrum of log reflectivity at the low frequency part rolls off and this refers to the spectral color.
- The objective of the color operator is to create a model that represents the color trend in the spectrum without reproducing the specific characteristics of reflectivity that must be preserved in the seismic; such as the reflections to be interpreted.
- The color operator should depend only on the observed spectral shape of the reflectivity. Also, this operator needs to correct the error of minimum-phase whitening deconvolution operator, therefore it must be minimum-phase.
- Three different color operators have been studied in this thesis. Autocorrelation Color (AC) operator which has been calculated from well reflectivity autocorrelation and arctan and sigmoidal color operator which have been calculated from curve fitting method.
- The spectral rolling off effect in the amplitude spectrum of reflectivity at the frequencies higher than half of Nyquist frequency is because of applying anti-alias filter which means using higher sample rates shifts the anti-alias filter effect to higher frequencies.

- The color operator can correct the whitening deconvolution errors of deconvolved trace but it is not able to recover all the low frequency components.
- The BLIMP algorithm is a robust method to calculate more accurate impedance from bandlimited seismic data by adding low frequency information from well log data. The results showed using color operator can improve the impedance estimation of BLIMP.
- To assist in the well tying process, calculating accurate P-wave velocity and density overburdens are necessary. A linear gradient has been used to calculate each of the overburdens to prevent artificial coefficients creation.
- Generally, the well tie process includes a time shift and a phase rotation and because of attenuation it may contain an extra time shifts at deeper events. This can be fixed numerically with a method such as dynamic time warping (DTW) method or manually by stretching the synthetic trace.
- A deconvolved trace shaped to a white spectrum can be corrected by applying a minimum-phase color operator after deconvolution.
- The minimum-phase color operator can be calculated separately for each well and then the average color operator can be applied to the whole seismic section or, by spatial interpolation between available color operators, a unique color operator can be computed for each seismic trace.
- Applying any of color operators to the stacked seismic traces causes their amplitude spectrum to roll off in low frequency to become similar with the spectral shape of well reflectivity. This causes the whole section to become dim.

- The result of impedance inversion is greatly improved after applying color correction because this affects the low frequencies and therefore the trend of the inversion.
- Colored inversion method is based on deriving the spectral shape of well impedance and then the amplitude spectrum of the colored inversion operator is determined as being that which maps the seismic spectrum to a spectral shape of well impedance.
- The colored inversion method is a fast and robust technique to calculate the deviation of acoustic impedance from background trend (e.g. no low frequency information) and it is similar to a -90 degree phase rotation.
- Comparing the maximum correlations between well acoustic impedance and estimated acoustic impedance from each method including before applying any color operator, after applying minimum-phase arctan, sigmoidal and AC color operator, colored inversion method and -90 degree phase rotation show that around 20 percent higher correlation can be reached if minimum-phase color operator has been applied to the deconvolved seismic data.

## References

- Aki, K., and Richards, P. G. (2002). *Quantitative Seismology*. Lamont-Doherty Earth Observatory of Columbia University.
- Bagaini, C., Bunting, T., El-Emam, A., and Strobbia, C. (2010). Land seismic techniques for highquality. *Oilfield Review*, 22(2).
- Burg, J. P. (1975). Maximum Entropy Spectral Analysis. *PhD thesis, Stanford University* .
- Cambois, G. (2002). Instrumentation or how many sows' ears does it take to make a silk purse? *The Leading Edge*, 21 (9), pp. 816-818.
- Canales, L. L. (1984). Random noise reduction. *54th Ann. Interna. Mtg., Society of Exploration Geophysics (SEG)*, (pp. 525-527).
- Claerbout, J. F. (1985). *Fundamentals of geophysical data processing with applications to petroleum prospecting*. Tulsa, OK: Pennwell Books.
- Cui, T., and Margrave, G. F. (2014). *Drift time estimation by dynamic time warping*. CREWES Research Report, Vol 26.
- Dolberg, D. M., Helgesen, J., Hanssen, T. H., Magnus, I., Saigal, G., and Pedersen, B. K. (2000). Porosity prediction from seismic inversion, Lavrans Field, Halten Terrace, Norway. *The Leading Edge*, 392-399.
- Ferguson, R. J., and Margrave, G. F. (1996). A simple algorithm for bandlimited impedance inversion. *CREWES research report, Vol. 8, No. 21*.
- Galbraith, J. M., and Millington, G. F. (1979). Low frequency recovery in the Inversion of seismoerams. *Journal of the CSEG*, v. 15, p. 30-39.
- Hunt, L., Gray, F. D., and Wallace, R. A. (1993). Using Reflectivity to Produce a Superior Deconvolution. *Canadian SEG Convention Technical Abstracts*, 95-96.

- Isaac, J. H., Margrave, G. F., Deviat., M., and Nagarajappa, P. (2012). *Processing and analysis of Hussar data for low frequency content*. CREWES Research Report, Vol. 24.
- Karastathis, V. C., Louis, I. F., Karantonis, G. A., and Apostolopoulos, G. V. (1995). Comparison tests of shallow seismic reflection sources. *EAGE Conference and Exhibition, Expanded Abstracts*, (pp. P035, 2 p).
- Lancaster, S., and Whitcombe, D. (2000). Fast-track 'colored' inversion. *SEG Technical Program Expanded Abstracts 2000*.
- Larner, K., Chambers, R., Yang, M., Lynn, W., and Wai, W. (1983). Coherent noise in marine seismic data. *Geophysics*, 48(7), 854-886.
- Lavergne, M., and Willm, C. (1977). Inversion of seismograms and pseudovelocity logs. *Geophys. Proso*, v. 25, p. 231 - 250.
- Leinbach, J. (1995). Wiener spiking deconvolution and minimum-phase wavelets: A tutorial. *Geophysics*.
- Lindseth, R. O. (1979). Synthetic sonic logs-a process for stratigraphic interpretation. *Geophysics*, 3-26.
- Lloyd, H. E. (2013). *An Investigation of the Role of Low Frequencies in Seismic Impedance Inversion*. Calgary: University of Calgary.
- Margrave, G. F. (2002). *Methods of seismic data processing*. Calgary: Department of Geoscience, University of Calgary.
- Margrave, G. F., and Lamoureux, M. P. (2002). Gabor deconvolution. *CSEG Geophysics*.
- O'Doherty, R. F., and Anstey, N. A. (1971). Reflections on amplitudes. *Geophysical Prospecting*, 19, 430–458.

- Oldenburg, D. W., Scheuer, T., and Levy, S. (1983). Recovery of the acoustic impedance from reflection seismograms. *Geophysics*, 1318-1337.
- Ongkiehong, L. (1988). A changing philosophy in seismic data acquisition. *First Break*, 6, pp. 281-284.
- Ongkiehong, L., and Huizer, W. (1987). Dynamic range of the seismic system. *First Break*, 5, pp. 435-284.
- Scheffers, B. C., Otte, W. A., Meekes, S. C., and Arts, R. J. (1997). Special aspects of acquisition of 2D HRS data using dynamite and Vibroseis sources. *59th EAGE Conference and Exhibition, Expanded*, (pp. Paper P045, 2 p).
- Sheriff, R. E., and Geldart, L. P. (1982). *Exploration seismology: History, theory, and data acquisition*. Cambridge Univ. Press, v.1.
- Sheriff, R. E., and Geldart, L. P. (1995). *Exploration Seismology*. Cambridge University Press.
- Walden, A. T., and Hosken, J. W. (1985). An investigation of the spectral properties of primary reflection coefficients. *Geophysical Prospecting*, 33, 400–435. doi:10.1111/j.1365-2478.1985.tb00443.x
- Waters, K. H. (1981). *Reflection seismology*. New York: John Wiley.
- Yang, L., Cai, L., and Dian, W. (2009). A 1D time-varying median filter for seismic random, spike-like noise elimination. *Geophysics*, 74, V17 - V24.
- Yilmaz, O. (1987). *Seismic data processing*. SEG.
- Yu, S. P., Zha, Z. Q., and Liang, J. (1984). Frequency. *Oil Geophysical Prospecting*, 19(3), 200-209.